Exotic properties of ordered phases in active matter

Brieuc Benvegnen

To cite this version:

Brieuc Benvegnen. Exotic properties of ordered phases in active matter. Condensed Matter [cond-mat]. Sorbonne Université, 2023. English. NNT : 2023SORUS334 . tel-04330742

HAL Id: tel-04330742
https://theses.hal.science/tel-04330742

Submitted on 8 Dec 2023

Sorbonne Université

École Doctorale n°564 : Physique en Île-de-France

Thèse de doctorat

Discipline : Physique Théorique

présentée par

Brieuc Benvegnen

Propriétés exotiques des phases ordonnées en matière active

---

dirigée par Alexandre Solon

et soutenue publiquement le 10 Octobre 2023.

Jury :

Rapporteurs :	M. Ignacio Pagonabarraga	-	University of Barcelona
	M. Martin Evans	-	University of Edinburgh
Directeur :	M. Alexandre Solon	-	Sorbonne Université
Présidente du Jury :	M$^{\text{me}}$ Cécile Appert-Rolland	-	Université Paris-Saclay
Examinateurs :	M. Vivien Lecomte	-	Université Grenoble-Alpes
	M. Eric Clement	-	ESPCI

Acknowledgments

I would like first to thank Ignacio Pagonabarraga and Martin Evans for a careful reading of the manuscript. I am also thankful to Cécile Appert-Rolland, Vivien Lecomte and Eric Clement for accepting to be in the jury of my PhD defence. Your comments have helped me to put my work in context.

Pendant ma thèse, j'ai eu le plaisir de travailler avec des personnes que j'estime beaucoup. Alex, merci pour ta présence sereine, ta disponibilité infaillible et ta rigueur scientifique inspirante. Tu as su m'aguiller vers des problèmes combinant à la fois du numérique et de l'analytique, ce qui a fait de ma thèse trois années riches et diversifiées. Hugues, tu m'as montré l'importance du sérieux des travaux numériques, et comment combiner admirablement science et soleil. Merci aussi pour ta franchise dans nos échanges. Enfin, un mot pour Guillaume, toi qui m'as donné le goût de la recherche bien avant que je ne commence cette thèse, et pour Julien, pour tes précieux conseils tout au long de ces trois années.

Je remercie aussi mes amis d'être chaque jour à mes côtés. Vincent et Zach, merci pour ces beaux moments de vie commune, parisiens comme canariens. Vous me faites grandir plus que vous ne l'imaginez. Jade, Clément, Davide, Etienne, Théo, Arthur, si ces trois années de thèse ont été si agréables, c'est aussi parce que je les ai partagées avec vous. Louis, Enzo, vous avez su comprendre ce que ma thèse représente pour moi et m'écouter avec intérêt, en faisant abstraction de nos trajectoires différentes. Jérémie, Léo, Julien, chers partenaires de bureau, ce fut un plaisir de travailler en musique à vos cotés.

Un immense merci à ma famille, dont le soutien à toute épreuve est difficile à exagérer. Grand-mère, Grand-père, merci d'être là pour moi. Papa, Maman, une pensée spéciale pour vous. Merci de rendre ma vie si facile. Vous connaissez mieux que personne les notes de la mélodie qui m'anime. Paulo, Max, merci pour ces moments de pause loin de la jungle parisienne. Je suis fier de vous avoir pour petits frères.

Contents

Chapter 1

Introduction

Contents

1.1 From equilibrium to non-equilibrium physics

When dealing with a many-body system, using classical and quantum mechanics to follow individual particle trajectories is most often untractable. The goal of statistical physics is then to develop models and methods that can effectively capture the statistical regularities of these systems and make predictions about their future states, at the cost of giving up the ambition to access the individual properties of particles. This requires developing mathematical techniques that can account for the many interactions between the objects within the system.

One of the first major successes of statistical physics is the development of the kinetic theory of gases in the 19th century by J.C Maxwell [Maxwell 1860]. This theory provides a statistical description of the behavior of a large number of gas molecules. It gives a microscopic basis to the ideal gas law and provides a foundation for thermodynamics. Another major success is the explanation of phase transitions in materials, such as the liquid-gas, or the paramagnetic-ferromagnetic phase transitions. In the early 20th century, Paul Ehrenfest developed a classification of such transitions on the basis of singularities in derivatives of the free energy function [Ehrenfest 1933]. They are now commonly used and known as first- and second-order transitions. In addition, statistical physics has played a key role in the development of other areas of physics, including the study of complex systems, from Bose-Einstein condensates to polymers and glasses.

1.1.1 Microscopic and macroscopic equilibrium

One way to statistically describe the dynamics of a system is through a set of configurations $\{\phi\}$ and transition rates W between them. These configurations may for instance encode the positions of particles in a gas or spins of ferromagnetic systems. When the configurations $\{\phi\}$ describe the microscopic scale, the system is in equilibrium if the probability flux from a state ϕ to a state ϕ' is equal to its reverse in steady-state:

$$P(\phi)W(\phi \to \phi') = P(\phi')W(\phi' \to \phi) \tag{1.1}$$

where $P(\phi)$ is the stationary probability to find the system in the configuration ϕ. This equation encodes the principle of *detailed balance*, which characterizes statistical equilibrium. A pragmatic illustration of detailed balance takes the form of Kolmogorov's criterion [Kolmogorov 1936]: the products of the transition rates for visiting a loop of three configurations in one order, $\phi_1 \to \phi_2 \to \phi_3 \to \phi_1$, must be equal to that of the reverse order $\phi_1 \to \phi_3 \to \phi_2 \to \phi_1$. This insures, for instance, that there is no net flux in phase space.

For systems in equilibrium at the macroscopic level *i.e.* at thermodynamic equilibrium, the dynamics can simply be ignored and the computation of macroscopic quantities such as pressure or entropy reduces to that of averages within the appropriate statistical ensemble. For instance, in the canonical ensemble at inverse temperature β, averages are taken with respect to the probability distribution $P(\phi) = \exp(-\beta\mathcal{H}(\phi))/Z$ where $\mathcal{H}$ is the Hamiltonian and Z the partition function.

The formalism of equilibrium statistical physics enables us to study a variety of systems using the same mathematical tools. Moreover, linear response theory predicts that if a system is only slightly perturbed from its equilibrium state, the equilibrium fluctuations dictate its nonequilibrium response, through the fluctuation-dissipation theorem [Einstein 1905, Callen & Welton 1951, Kubo 1966], extending the use of equilibrium statistical mechanics to systems that are 'close' to equilibrium. However, in many interesting situations, it is not the case. One is then required to study the dynamics of these out-of-equilibrium systems using novel analytical and numerical tools.

1.1.2 Out-of-equilibrium physics

A system can be out-of-equilibrium for numerous reasons. An isolated Hamiltonian system is out-of-equilibrium if its equilibration time towards stationary state diverges, which is known as critical slowing down. This is the case of glasses that remain trapped in a complex energy landscape without being able to relax to an equilibrium state [Berthier & Biroli 2011]. Externally driven systems with open boundary conditions, such as living organisms that are constantly exchanging energy and matter with their environment, or systems subject to an external field like shear or shaking, are also out-of-equilibrium. Bacterial colonies or flame fronts are growing systems and, as such, are not in thermodynamic equilibrium.

The study of such systems unveiled out-of-equilibrium universality classes, among which the now-famous KPZ class for growing interfaces [Kardar *et al.* 1986]. A dynamic field of research which displays a wide range of out-of-equilibrium behaviors and breaks detailed balance at the microscopic level is active matter.

1.2 Active matter

Active matter encompasses all systems whose components dissipate energy in order to exert forces on their environment. Depending on the nature of the force, the dynamics of individual components can take many forms, the most common being self-propulsion.

1.2.1 Origins of the field

Active matter emerged as a topic of physics research in the 1990s. Its origins can be traced back to 1995 and the influential publications of [Vicsek *et al.* 1995] and [Toner & Tu 1995]. They showed that self-propelled particles with local ferromagnetic alignment can order even in two dimensions, whereas such ordered state would be destroyed by fluctuations in the passive case, in agreement with the Mermin-Wagner theorem [Mermin & Wagner 1966]. This set the stage for three decades of animated investigations revolving around the theoretical novelties raised by this system such as the nature of the transition to the ordered state or the computation of critical exponents. An overview of these investigations will be the topic of Sec. 1.3.

Around the same time, the concept of Active Brownian Particles (ABPs) appeared in 1995 to refer to Brownian particles with the ability to generate a field, which in turn can influence their motion [Schimansky-Geier *et al.* 1995]. Later, [Ebeling *et al.* 1999] used the same terminology for the now-widely adopted model of self-propelled particles based on a Langevin equation. The concept of Run-and-Tumble particle (RTP) was introduced by [Schnitzer 1993] with an example of application being the modelling of the movement of swimming bacteria [Galajda *et al.* 2007] such as *E. coli* [Berg 2004]. Later, [Tailleur & Cates 2008] showed that collections of highly persistent RTPs display aggregating dynamics,

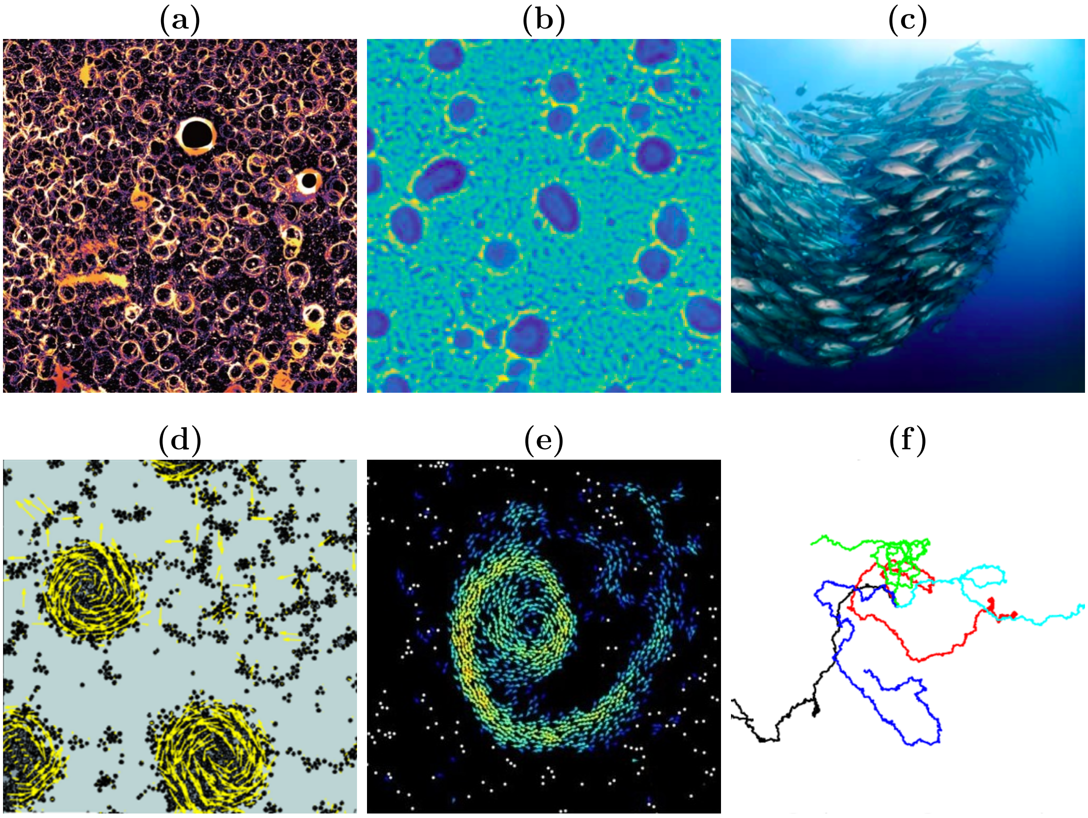

Figure 1.1: Examples of collective behaviours in active matter in the biological realm (top) and in engineered systems (bottom). **(a):** Microtubule vortices [Sumino *et al.* 2012]. **(b):** Fruiting bodies of *Myxococcus xanthus* [Liu *et al.* 2019]. **(c):** School of Trevally fish. **(d):** Rotating clusters of Quincke walkers [Karani *et al.* 2019]. **(e):** Spiral flock of Quincke rollers [Liu *et al.* 2021]. **(f):** Trajectories over 25 sec for 5 self-propelled Janus particles [Howse *et al.* 2007].

now refered to as Motility-Induced Phase Separation (MIPS). This behaviour was then extended to ABPs, and will be the topic of Sec. 1.4.

1.2.2 Ubiquity of active matter systems

In addition to the theoretical interests raised by active matter, its study is also relevant to various fields, in particular in biology (See Fig. 1.1, top row, for some illustrations) at the scale of molecular motors, where vortices are persistently reported [Schaller *et al.* 2011, Sumino *et al.* 2012] or in bacterial swarms [Ben-Jacob 2003, Sokolov & Aranson 2012], displaying active bioturbulence [Wensink *et al.* 2012], influencing viscosity [López *et al.* 2015], or exhibiting spatial patterns [Liu *et al.* 2019, Curatolo *et al.* 2020]. At larger scales, collective behaviors of animal groups are subject to constant investigations. In particular, starlings have been extensively studied [Cavagna *et al.* 2010, Parisi 2023], along with fish shoal [Gautrais *et al.* 2012, Poel *et al.* 2022] or swarms of midges [Attanasi *et al.* 2014a].

In addition to biological systems, some typical condensed matter systems were made motile [Aranson 2013, Zhang *et al.* 2017]. Some examples are shown in Fig. 1.1, bottom row. For instance, [Howse *et al.* 2007] used particles half-coated with platinum (an example of Janus particles) in a solution of water and hydrogen peroxide. The platinum catalyzes the reduction of hydrogen peroxide to oxygen and water, producing a chemical gradient which propels the particle. Other mechanisms can be used to propel inert units. One of them is the Quincke effect [Tsebers 1980]. Quincke rollers make use of the spontaneous rotation of a dielectric sphere submerged in a conductive fluid and exposed to a static electric field, propelling the sphere. Assemblies of such active colloids have been shown to display intriguing features, organizing in whirling structures [Karani *et al.* 2019, Liu *et al.* 2021] or presenting out-of-equilibrium collective behaviours [Bricard *et al.* 2013, Geyer *et al.* 2019]. Self-propelled Janus particles enabled to run experimental tests of theories [Ginot *et al.* 2018] while collection of vibrated macroscopic objects have been shown to generically display flocking [Deseigne *et al.* 2010, Kumar *et al.* 2014, Soni *et al.* 2020].

While some real-life experiments are possible, most of the investigations are carried out using two complementary approaches: agent-based models and continuum models.

1.2.3 Models of self-propelled particles

Active particles for which interactions with the solution cannot be neglected are commonly refered to as microswimmers and belong to the class of *wet* active matter. According to the kind of far-field fluid flow that they induce, they are classified into two microswimming types: pushers, like most bacteria, which self-propel from the rear, and pullers, like algae *Chlamydomonas reinhardtii*, that

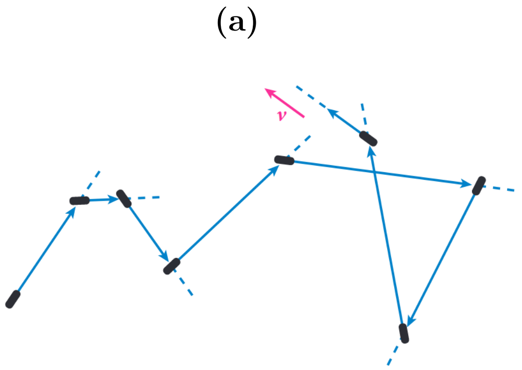

Figure 1.2: Simulated paths of **(a)** run-and-tumble and **(b)** active Brownian particles. Reproduced from [Cates & Tailleur 2015].

pulls in the fluid in front with a pair of flagella. The long-ranged interactions make analytical study of wet active matter challenging.

For simplicity, in the following, we will instead consider *dry* active matter, in which hydrodynamic interactions between the constituting particles are neglected. The fluid is assumed to only provide friction, rendering the dynamics overdamped [1]. Energy is injected at the microscopic level by allowing the particles to self-propel in a direction that has its own dynamics. A simple way to account for self-propulsion is to model it as a force with constant magnitude F_p acting on particles. We write the dynamics of a self-propelled particle of mass m as

$$m\ddot{\mathbf{r}} = -\gamma\dot{\mathbf{r}} + F_r\mathbf{e}_\theta \tag{1.2}$$

where γ is the viscous friction coefficient and $\mathbf{e}_\theta$ is a unitary vector oriented in the direction of motion. Eq. (1.2) can be supplemented by a term of thermal noise which is often considered negligible. In the overdamped limit that we will consider in this thesis, particles thus self-propel at constant speed $v = F_r/\gamma$ in free space. We now present two archetypal models of active particles: Active Brownian Particles (ABPs) and Run-and-Tumble Particles (RTPs), pictured in Fig. 1.2. ABPs are continuously reorienting their direction of motion by rotational

---

[1] It is a limit relevant for most active matter systems.

diffusion. In two dimensions, their dynamics read:

$$\begin{cases} \dot{\mathbf{r}} = v\mathbf{e}_\theta \\ \dot{\theta} = \sqrt{2D_r}\eta \end{cases} \tag{1.3}$$

where D_r is the rotational diffusion coefficient and η is a unit-variance Gaussian white noise. In contrast, RTPs self-propel in straight lines ("runs") but stochastically choose a new direction at random, during a "tumble" event. For bacteria, which show run-and-tumble dynamics, these tumble events are usually significantly shorter than the runs, so that we neglect their duration and assume they are instantaneous.

We consider active particles interacting locally with their neighbours through two mechanisms: alignment or speed regulation. Alignment causes particles to align their direction of motion with their neighbours. In Nature, this can be the result of steric interactions, hydrodynamic interactions, or even voluntary reorientation. Speed regulation can also result from different phenomena, the simplest being short-range pairwise repulsive interactions such as excluded volume interactions. Indeed, when two active particles – such as ABPs or RTPs – collide head to head, they momentarily stop their motion until one of the particles rotates in a different direction. This induces an effective decrease in velocity upon contact. Speed can also be intentionally regulated by the particle, as is the case for bacteria reacting to fluctuations of concentration of a chemical in their environment, in a process called quorum-sensing.

In most realistic cases, we expect a combination of alignment and speed regulation to enter the dynamics. In the rest of this work, we will instead focus on the extreme cases where alignment is the only interaction or where speed regulation dominates and show that even in these simple settings, many issues remain to be addressed.

1.2.4 Continuum theories

In addition to particle-level models and simulations, active matter can be examined using continuum models. They exhibit the structure of generalized hydrodynamic equations for continuous fields, commonly density and velocity. The evolution of these fields describes the large-scale, long-time behaviour of the system and includes non-equilibrium terms arising from the activity. In the few cases where continuum theories can be constructed from microscopic models by coarse-graining the dynamics, the procedure allows to establish a connexion between the parameters in the macroscopic equations and the specific physical mechanisms (noise, self-propulsion speed, etc).

A different, more empirical method, involves writing hydrodynamic equations for the macroscopic fields that encompass all possible terms allowed by symmetry. This methodology involves the appearance of numerous terms whose physical meaning are not necessarily apparent at first. Moreover, this procedure prevents establishing a straightforward connexion between microscopic dynamics and macroscopic properties. When restricted to contain a minimal amount of terms, it however proved useful to describe some behaviours. For instance, Model B [Hohenberg & Halperin 1977], the standard field theory for phase separation at equilibrium, was constructed in this spirit. This approach was also employed in active matter by [Toner & Tu 1995] to describe flocks (the resulting equations will be presented in Sec. 1.3.2), and later extended to include self-propelled particles suspended in a fluid in [Aditi Simha & Ramaswamy 2002] and active filament solutions in [Hatwalne *et al.* 2004].

Among the various phenomena observed in active matter, two phase transitions are specific to active systems: the transition to collective motion (flocking) and the Motility-Induced Phase Separation (MIPS). These two transitions to collective behaviours can be captured by simple models and exhibit ordered phases that we will study in this thesis.

1.3 Flocking

1.3.1 Real flocks

The most widespread and spectacular manifestation of collective behaviour in active matter is arguably collective motion, also known as *flocking*. It features self-propelled particles aligning their direction of motion, which self-organize to

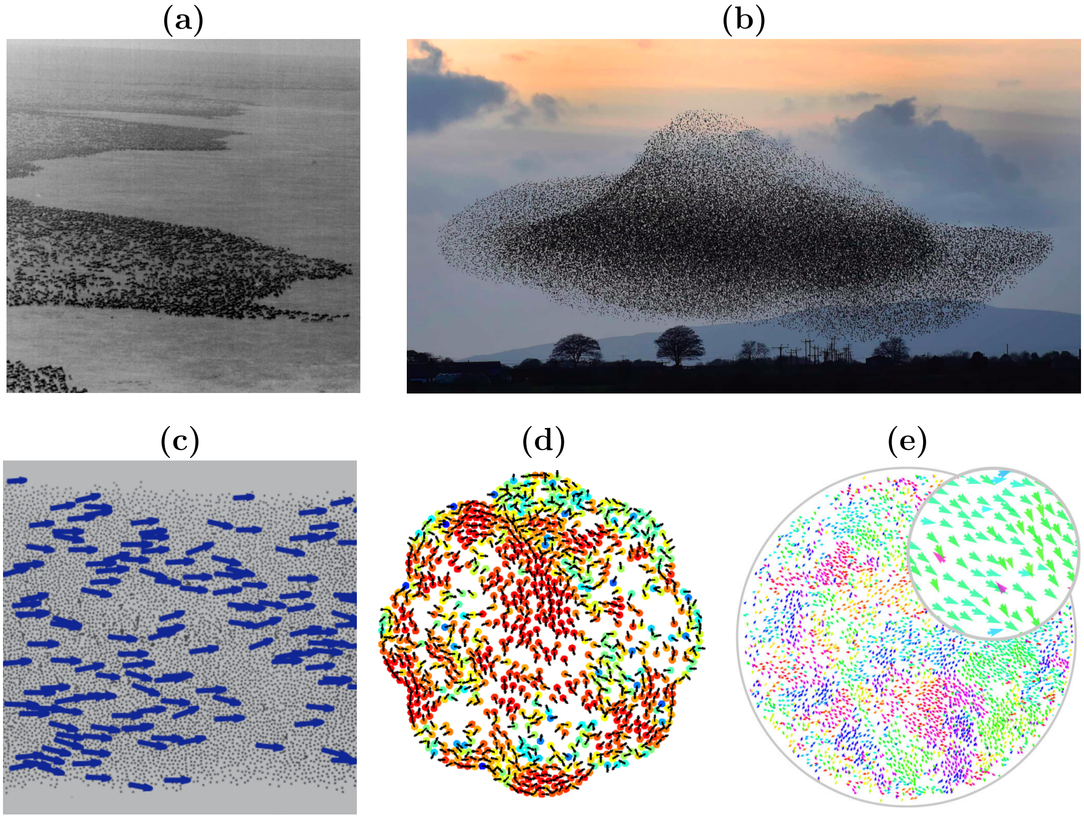

Figure 1.3: Collective motion in active matter. **(a):** Aerial photograph of a large wildebeest herd [Gueron & Levin 1993]. **(b):** Murmuration of starlings. **(c):** Homogeneous polar phase in a system of rolling colloids [Bricard *et al.* 2013]. Blue arrows correspond to roller displacement between two subsequent movie frames. **(d):** Vibrated grains [Deseigne *et al.* 2010]. **(e):** Local order inside of collective chiral rollers motion [Zhang *et al.* 2020].

move collectively on large scales in a coordinated manner without any central control. Flocking is commonly observed at all scales in many biological systems: cells migrate collectively, thus keeping the tissue or structure intact and continuous while remodeling it [Rørth 2009, Giavazzi *et al.* 2017]. More commonly, insects [Attanasi *et al.* 2014b], school of fish [Shaw 1978, Weihs 1973] or herds of wildebeest [Banerjee 1992, Gueron & Levin 1993] are known to exhibit collective motion (See Fig. 1.3a) during periods of migration. Perhaps the most in-depth study of animal flocking was conducted on flock of starlings [Cavagna *et al.* 2008], which display remarkably coordinated behaviours, as show in Fig. 1.3b. Cavagna *et. al.* achieved the 3D reconstruction of flocks of thousands of birds under field conditions, paving the way for further enlightening investigations [Ballerini *et al.* 2008] as well as providing data to test theories of collective animal behaviour [Cavagna & Giardina 2014].

Flocking is also observed in engineered active particles. [Bricard *et al.* 2013] studied large populations of Quincke colloidal rollers that self-propel and align through hydrodynamic interactions. They confined the roller population in racetracks and witnessed, increasing density, the transition from a disordered gas to a state of collective motion, as shown in Fig. 1.3c. [Deseigne *et al.* 2010] investigated vibrated disks that possess an inherent polar asymmetry, allowing them to move with quasi-ballistic behaviour over a significant persistence length. Alignment occurs during collisions due to the interplay of the self-propulsion and the repulsive forces between the disks' hard cores. They witnessed the emergence of large-scale collective motion by varying the amplitude of the vibration (Fig. 1.3d). Flocking seems to be a rather robust feature: [Zhang *et al.* 2020] employed shape-anisotropic Quincke rollers to make active chiral rollers. They nonetheless found rotating flocks exhibiting local polar ordering, as shown in Fig. 1.3e. These systems are different in terms of their sizes and have greatly differing dynamics at the microscopic level but they exhibit similar macroscopic collective properties resulting from the coupling of self-propulsion and alignment.

1.3.2 The Vicsek Model

The first minimal model containing these two key ingredients was introduced by [Vicsek *et al.* 1995]. It features N self-propelled particles moving at constant speed v in the $2d$ plane of surface S, along a direction given by an angle θ. These particles undergo a local alignment in the following way: at discrete time steps, each particle averages the direction of propulsion of its neighbours in a unit disk. It then performs a noisy alignment of its direction of motion with this prefered direction:

$$\theta_k(t+1) = \langle \theta_i \rangle_{i \in \mathcal{N}_k} + \eta \xi_k \tag{1.4}$$

where $\mathcal{N}_k$ is the unit disk centered on the particle k and ξ_k is drawn from a uniform disribution in $[-\pi, \pi]$. The particles then update their positions using this new orientation:

$$\mathbf{r}_k(t+1) = \mathbf{r}_k(t) + v\mathbf{e}_{\theta_k(t+1)} \tag{1.5}$$

Here, $\mathbf{e}_{\theta_k(t+1)}$ is simply the unit vector oriented along the angle $\theta_k(t+1)$. When the noise amplitude on the alignment η is low, particles tend to align and move on average in the same direction. This simple model therefore showed that self-propulsion and local alignment are sufficient ingredients to observe collective motion.

Shortly after the introduction of the Vicsek Model (VM), [Toner & Tu 1995] proposed a hydrodynamic description based on the symmetries of the system. It describes a conserved field ρ advected by a velocity field $\mathbf{v}$:

$$\partial_t \rho + \nabla \cdot (\rho \mathbf{v}) = 0$$

$$\begin{aligned}\partial_t \mathbf{v} + \lambda_1(\mathbf{v}\cdot\nabla)\mathbf{v} + \lambda_2(\nabla\cdot\mathbf{v})\mathbf{v} + \lambda_3\nabla(|\mathbf{v}|^2) = &\left(\alpha - \beta|\mathbf{v}|^2\right)\mathbf{v} - \nabla P + D_L\nabla(\nabla\cdot\mathbf{v}) \\ &+ D_1\nabla^2\mathbf{v} + D_2(\mathbf{v}\cdot\nabla)^2\mathbf{v} + \mathbf{f}\end{aligned}$$

where $\mathbf{f}$ is a Gaussian white noise. This set of equations is similar to Navier-Stokes equations supplemented by a standard Ginzburg-Landau term $\left(\alpha - \beta|\mathbf{v}|^2\right)\mathbf{v}$ imposing a non-vanishing velocity $|\mathbf{v}| = \sqrt{\alpha/\beta}$. The constants λ_1, λ_2 and λ_3 correspond to advective terms while D_L, D_1 and D_2 are diffusion constants. The pressure P is expressed as a series expansion in term of the density field ρ. These equations served as a basis to describe a new non-equilibrium universality class and, in particular, to predict scaling exponents in the homogeneous phase of the VM, which are still a topic of discussion [Toner & Tu 1998, Tu *et al.* 1998, Toner *et al.* 2005, Toner 2012b, Mahault *et al.* 2019].

1.3.3 Transition to collective motion

After the seminal publications of the VM and its theoretical study, it was commonly believed that an appropriate framework for the understanding of the transition to collective motion was that of a continuous order-disorder transition. However, the nature of the transition was subsequently extensively studied [Grégoire & Chaté 2004, Chaté *et al.* 2008, Baglietto & Albano 2009]. On the contrary, Chaté *et. al.* showed that the apparent continuous transition is a finite-size effect. At fixed density $\rho_0 = N/S$, starting in the disordered phase (Fig. 1.4a) and decreasing the noise η, they observed a discontinuous transition

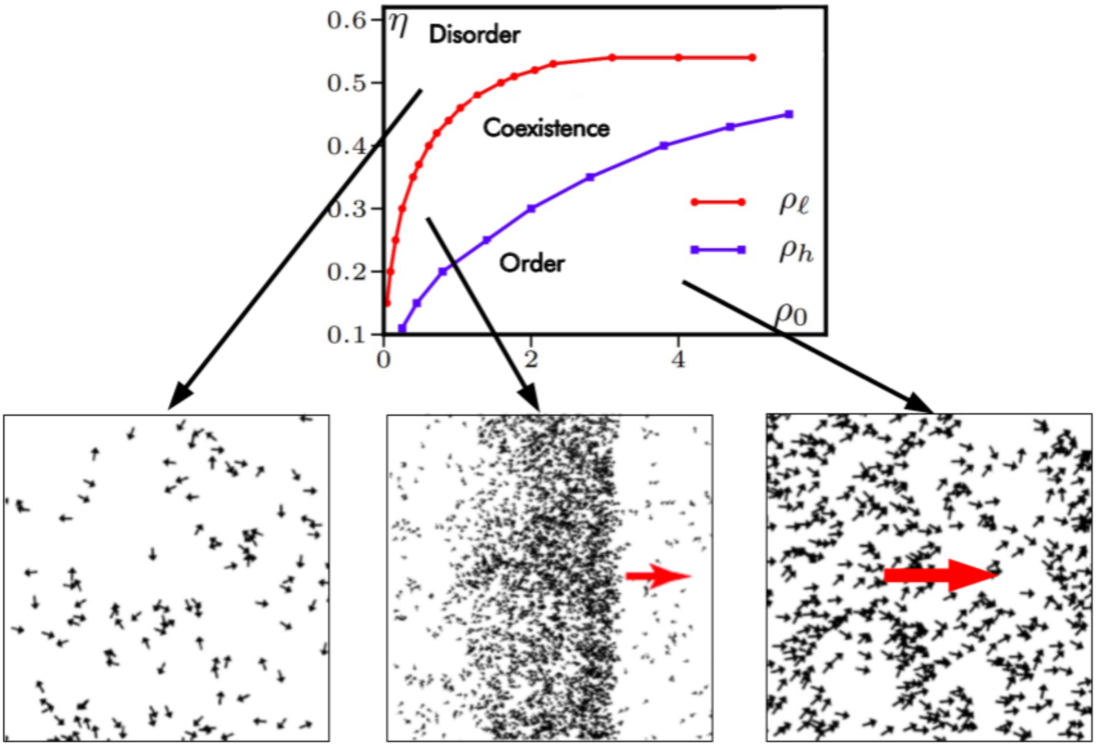

(a) **(b)** **(c)**

Figure 1.4: Phase diagram of the Vicsek Model and corresponding snapshots from simulations. Keeping the density constant, at high noise the system is a disordered gas **(a)**. Decreasing the noise, the system transitions to a state of collective motion where ordered liquid bands coexist with a dilute gas **(b)**. Finally, at low noise value, the system is found in a state of homogeneous polar order **(c)**. Red arrows indicate the prefered direction of motion. Reproduced from [Solon *et al.* 2015c].

to the formation of dense ordered bands (Fig. 1.4b) propagating in a dilute disordered gas. At low noise values, they recovered the homogeneous ordered phase (Fig. 1.4c). Moreover, these bands emerge through the nucleation of many liquid domains which coarsen into bands, and hysteresis is observed in the transition from disorder to band phase, as for first-order transition at equilibrium. Therefore, the transition is now recognized as a discontinuous first-order phase transition [Martin *et al.* 2021a].

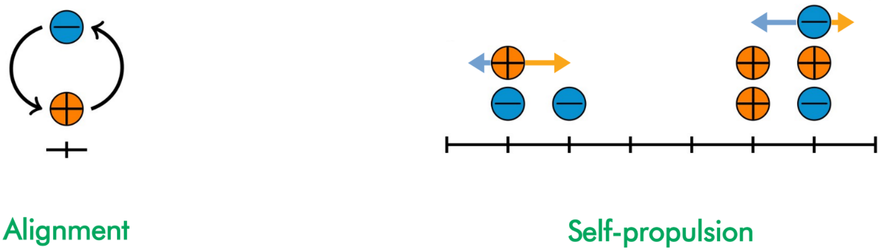

Alignment

Self-propulsion

Figure 1.5: Sketch of the two ingredients of the Active Ising Model: on-site alignment and self-propulsion.

1.3.4 A liquid-gas phase separation

Large finite-size effects makes the numerical study of the VM challenging. Progress in the understanding of the flocking transition has been made following the introduction of the Active Ising Model (AIM) [Solon & Tailleur 2013, Solon & Tailleur 2015], a simple stochastic lattice gas that contains the same ingredients as the VM. In the AIM, particles self-propel by diffusing in a direction biased by the Ising spin they carry: particles carrying a ⊕-spin move to the right whereas particles carrying a ⊖-spin move to the left. The continuous rotational symmetry of the VM is simply replaced by a discrete symmetry in the AIM. Local alignment of the self-propulsion direction takes the form of an on-site ferromagnetic alignment between the spins of the particles. The dynamics of the AIM are pictured in Fig. 1.5.

Like the VM, the AIM displays a phase transition to collective motion: decreasing the temperature, which controls the strength of the alignment dynamics, it transitions from a disordered gas to an ordered band propagating in a residual gas (the coexistence phase), to finally reach a homogeneous ordered phase. This transition is very similar to an equilibrium liquid-gas transition. For instance, in the coexistence phase, the density of the gas and of the liquid band are only fixed by the speed of self-propulsion and the temperature. Increasing the density of particles only results in an increase of the liquid fraction in the system, thus verifying the lever rule, as in equilibrium [Solon & Tailleur 2015].

The transition to collective motion in the VM can also be interpreted as a liquid-gas phase transition, the only qualitative difference with the AIM being the shape of the bands in the coexistence phase. While in the AIM, the system phase separates into two distinct dense and dilute domains, in the VM the system displays a microphase separation: an extensive number of finite-size evenly-spaced ordered bands travel in a dilute gas [Solon *et al.* 2015b]. This qualitative difference was rationalized at the hydrodynamic level by taking into account the fluctuations in the continuum descriptions of both the AIM and the VM, which were shown to play a central role in the selection of the shape of the bands [Solon *et al.* 2015c]. More generally, [Martin *et al.* 2021a] showed that fluctuations turn continuous transitions to collective motion predicted by deterministic hydrodynamics into phase separation. All in all, the previous paradigm of an order-disorder magnetic transition is now replaced by a phase separation between a disordered gas and an ordered liquid.

In Chapter 2 we will study the $1d$ AIM, and show that this liquid-gas phase separation paradigm partially survives in one space dimension, in the form of an ordered phase where particles aggregate and move collectively. Symmetry is not broken though because the aggregate reverses stochastically its direction of motion due to the prominent effect of fluctuations. We will rationalize this behavior by explaining the dynamics of the aggregates and their reversals. At lower temperature, we observe static structures which are amenable to an analytic treatment.

Chapter 3 will be devoted to the study of the stability of the flocking phase of the AIM. We will show that both the band in the coexistence phase and the homogeneous ordered phase are metastable to the nucleation of counter-propagating droplets in the $2d$ AIM. Using a continuous description, we will show that such droplets propagate if they are large enough and characterize analytically their self-similar growth. Our results imply that, in the thermodynamic limit, discrete-symmetry flocks are metastable in all dimensions.

1.4 Motility-Induced Phase Separation

1.4.1 Realizations of MIPS

In contrast to flocking, where the collective motion results from the coupling of self-propulsion and alignment, the Motility-Induced Phase Separation (MIPS) is a collective behavior emerging as a consequence of the dynamic interplay between self-propulsion and velocity-regulation. It is perhaps the most elementary phase transition observed in active matter. As already mentioned in Sec. 1.2.3, particles progressing in a dense area can experience a decrease in their velocity, whether because of collisions or quorum-sensing mediated interactions. As a result, they accumulate in high density regions. The mutual influence of these two ingredients generates a feedback mechanism leading to the progressive appearance of clusters of high density surrounded by a dilute phase. These clusters undergo coarsening until only one macroscopic cluster remains, coexisting with a remaining gas, and thus achieving a full phase separation.

This scenario was first predicted in [Tailleur & Cates 2008] for Run-and-Tumble Particles (RTPs) interacting via quorum-sensing and subsequently triggered a multitude of numerical realizations of MIPS. Active Brownian Particles (ABPs) interacting solely through excluded volume effects, without any aligning interactions, have been studied extensively [Fily & Marchetti 2012, Cates & Tailleur 2013, Redner *et al.* 2013, Stenhammar *et al.* 2013, Bialké *et al.* 2013, Wysocki *et al.* 2014, Solon *et al.* 2015e, Takatori & Brady 2015]. At high density, they have been shown to phase separate in the form of the coexistence of dense clusters with a dilute gas (Fig. 1.6a) which then coarsen into one macroscopic cluster. In models of RTPs reducing their swimming speed in high density regions, [Tailleur & Cates 2008, Thompson *et al.* 2011, Solon *et al.* 2015a] also reported the formation of high-density clusters, as shown in Fig. 1.6b. Recently, [Fodor *et al.* 2016, Martin *et al.* 2021b] studied active Orstein-Uhlenbeck particles, which have the property of having Gaussian fluctuations of their velocity, interacting by pairwise repulsive forces and also found the system to display MIPS (Fig. 1.6c).

Experimentally, in addition to self-propulsion and repulsive interactions, the systems usually feature various other more or less controlled effects, such as at-

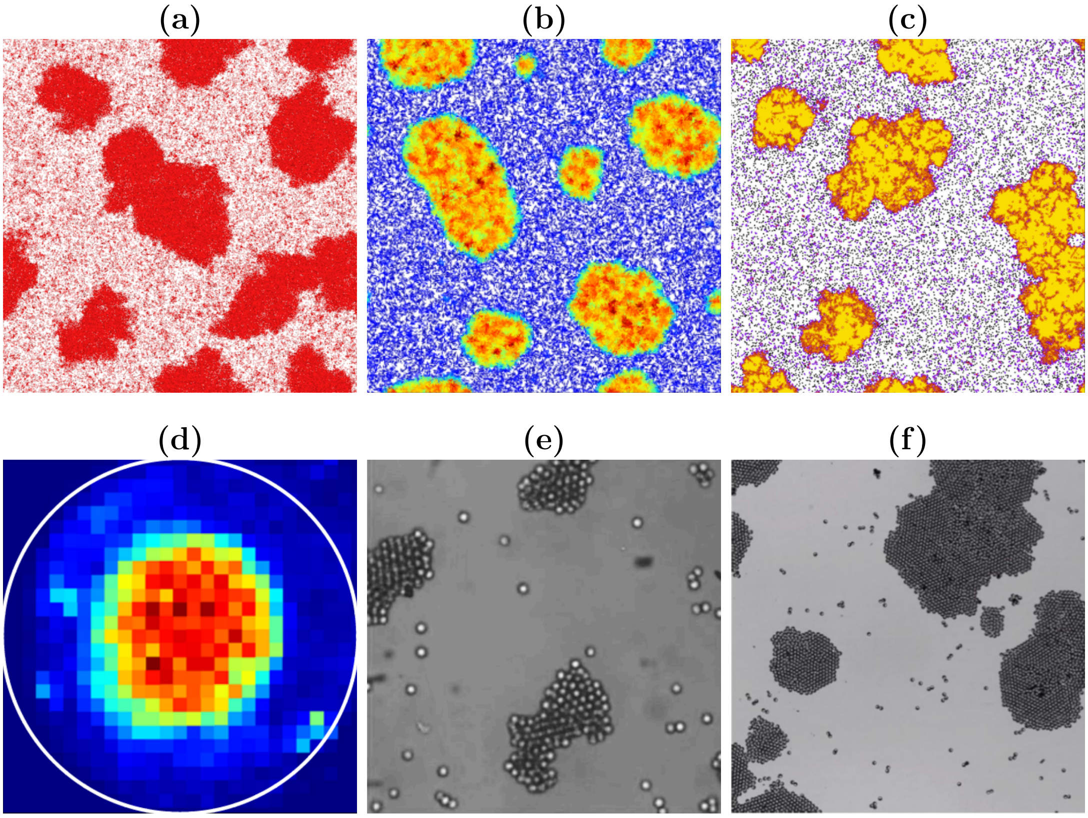

Figure 1.6: Motility-Induced Phase Separation in numerical simulations (top row) and in experimental setups (bottom row). **(a):** Coarsening stage for ABPs [Redner *et al.* 2013] and **(b)** for RTPs swimming at speed $v(\tilde{\rho})$ where $\tilde{\rho}$ is the average density around a particle [Solon *et al.* 2015a]. **(c):** Occurence of MIPS for active Ornstein-Uhlenbeck particles [Martin *et al.* 2021b]. **(d):** Experimentally measured density of self-propelled colloids whose motility is tuned by a computer-assisted loop reducing their swimming speed in high density regions [Bäuerle *et al.* 2018]. Warmer colors indicate higher local density. Self-propelled Janus particles undergoing clustering in [Buttinoni *et al.* 2013] **(e)** and in [van der Linden *et al.* 2019] **(f)**.

tractive forces or hydrodynamic interactions. Untangling these effects from the bare MIPS ingredients is a difficult challenge which has partially motivated the numerous numerical studies, in which the precise ingredients are known. Still, some experimental setups clearly display MIPS. Among them, [Bäuerle *et al.* 2018] used silica spheres which are half-coated by a carbon film and suspended in a water–lutidine mixture. The activity of each particle is tuned in real time by using a laser focusing on the particles and heating the carbon caps to adjust their velocities on the local density. Decreasing the particle velocity in region of high density triggers MIPS, as seen on Fig. 1.6d. [Buttinoni *et al.* 2013] used the same particles, albeit with a constant velocity and repulsive interactions, and reported another instance of MIPS (See Fig. 1.6e). Finally, in [van der Linden *et al.* 2019], titanium-coated Janus colloids self-propelled by an external electric field undergo phase separation until a critical size, at which point clusters break apart due to alignment forces between particles.

Phase separation and clustering patterns have also been reported in some experimental setups in which additional ingredients become relevant. [Liu *et al.* 2011] genetically modified cells to couple their motility to the surrounding density and observed the appearance of periodic stripes of high and low cell densities, as predicted in [Cates *et al.* 2010] from the study of MIPS applied to growing cell colonies. The fruiting bodies of *Myxococcus xanthus* mentioned in Sec. 1.2.2 and shown in Fig. 1.1b were argued to result from an interplay between MIPS and other mechanisms, such as cell communication and alignment [Liu *et al.* 2019]. Very recently, collections of fire ants were shown to undergo clustering [Anderson & Fernandez-Nieves 2022] which can be understood in the framework of MIPS.

1.4.2 Generalized thermodynamics

MIPS phenomenology is now best understood through the generalized thermodynamic formalism presented in [Solon *et al.* 2018b, Stenhammar 2021], the construction of which we give a brief overview here. The goal is to formulate a hydrodynamic theory for the only relevant hydrodynamic field: the density $\rho(\mathbf{r}, t)$ of active particles. To do so, they assume that active particles adapt their velocity to their surrounding density, so that their velocity is written as a functional of the density field: $v(\mathbf{r}, [\rho])$. Expanding $v(\mathbf{r}, [\rho])$ at order $\mathcal{O}(\nabla^2)$ and introducing a variable $R(\rho)$ playing the role of density, they are able to write the evolution of the conserved field ρ:

$$\partial_t \rho(\mathbf{r}, t) = \nabla \cdot [M \nabla \mu] \tag{1.6}$$

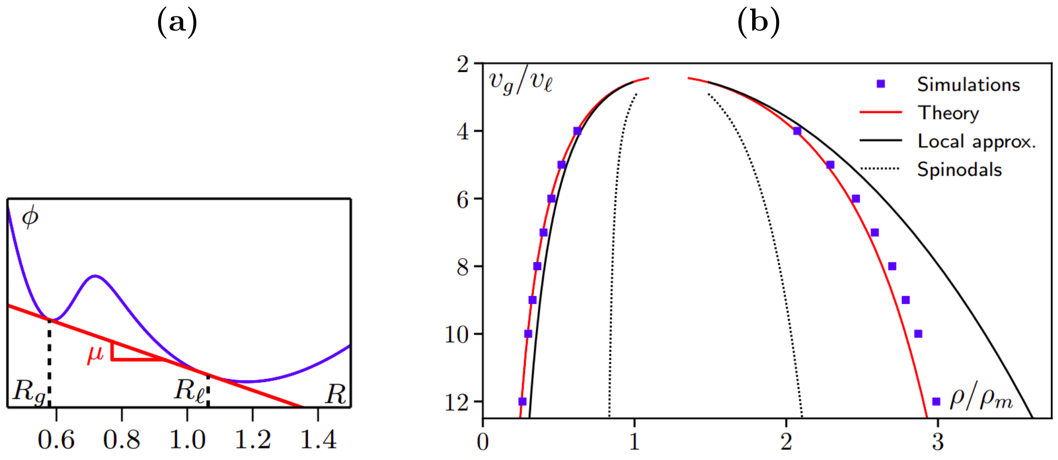

Figure 1.7: **(a):** The binodals are computed through a common tangent construction on the generalized free energy defined in Eq. (1.8). **(b):** Comparison between the binodals measured in simulations of RTPs in $2d$ and the binodals predicted by the generalized thermodynamics (red line). Adaptated from [Solon *et al.* 2018b].

with μ the derivative of a generalized free-energy $\mathcal{G}$ with respect to a variable $R(\rho)$:

$$\mu = \frac{\delta \mathcal{G}}{\delta R(\rho)} \tag{1.7}$$

The "effective density" $R(\rho)$ is in one-to-one mapping[2] with ρ but depends on additional out-of-equilibrium terms appearing in the expression of $\mathcal{G}$ which is given by:

$$\mathcal{G} = \int d\mathbf{r} \left[\phi(\mathbf{r}) + \kappa(\nabla R)^2\right] \quad \text{with} \quad \frac{d\phi(R)}{dR} = \ln(\rho v(\rho)) \tag{1.8}$$

where κ can be explicitely written as a function $v(\rho)$. The existence of the free-energy $\mathcal{G}$ enables to recast the problem of finding the phase equilibria of an active phase separation into an standard equilibrium one. For instance, the coexisting effective densities R_g and R_ℓ of the gas and the dense phase respectively can be obtained from a common tangent construction on $\phi(R)$ (Fig. 1.7a). The resulting binodal densities ρ_g and ρ_ℓ (red lines in Fig. 1.7b) are found to be in very good agreement with numerical measurements.

---

[2] See details of the derivation in [Solon *et al.* 2018b].

This theory provides a unified framework to understand the phase equilibrium in MIPS. However, it fails to account for the finite-size effects observed in collections of particles interacting via repulsive forces. Indeed, in these systems, the Laplace pressure difference between a finite droplet and the surrounding gas was measured to be negative [Bialké *et al.* 2015, Solon *et al.* 2018a, Patch *et al.* 2018]. Analytical and numerical particle-level investigations then provided evidences that such a negative surface tension triggers the nucleation and growth of gas bubbles in the dense phase in stationary state [Tjhung *et al.* 2018, Caporusso *et al.* 2020, Shi *et al.* 2020].

In Chapter 4, we will investigate several minimal models to explain the bubble dynamics observed in MIPS. We will show that these models generically display scale-free distributions that we will characterize both numerically and using a mean-field approach. We will conclude by providing numerical evidences in favor of a homogeneous nucleation process generating the MIPS bubbly phase separation.

Chapter 2

Flocking in one dimension

Contents

2.1 Introduction

In the one-dimensional Ising model, that is a chain of spins interacting ferromagnetically with their nearest neighbors, the ordered phase is destroyed by thermal fluctuations. Specifically, Ising showed in his 1924 PhD thesis, and one year later in a short article [Ising 1925], that for any non-vanishing temperature, the free energy is analytic in the thermodynamics parameters. Therefore, no phase transition is observed and the system remains in a disordered state. This is a rather generic fact that can be understood from the Landau argument [Landau & Lifshitz 1980]: the energy of a domain wall separating two regions of opposite magnetization being finite, the system minimizes its free energy by breaking up into a macroscopic number of domains at any positive temperature. This is however expected to fail if the energy of a domain wall can be extensive. As we will see in this chapter, this happens in a peculiar way in $1d$ flocking.

2.1.1 Alternating ordered state

Different $1d$ models of collective motion have been proposed that contain two basic ingredients: self-propulsion and alignment, without any excluded volume interactions. They differ in the details of their implementation. [Czirók *et al.* 1999] studied a system consisting of N off-lattice particles that self-propel and interact locally with their neighbors by a noisy alignment of their direction of self-propulsion (left or right). The same year, [O'Loan & Evans 1999] introduced a lattice model with ± particles moving to the right and left and no limit on the number of particles on a site. The alignment is implemented by a noisy majority rule: A particle i is chosen at random and flips its velocity $v_i = \pm 1$ with rate $W_i = [1 - (1 - 2\eta)v_i U_i]$ where $U_i = \pm 1$ if there are a majority of ± particles on the site of i and its two nearest neighbors ($U_i = 0$ in absence of a majority) and η controls the noise strength. In average, particles therefore acquire the velocity of the majority of their neighbors with probability $1 - \eta$. Later, [Solon & Tailleur 2013] proposed a lattice model of self-propelled particles carrying an Ising spin and interacting through an on-site ferromagnetic alignment.

They all observe ordered aggregates that move ballistically and reverse their direction of motion, as shown in Fig. 2.1. On the left, starting from an initial homogeneous disordered state, the model of [Czirók *et al.* 1999] displays the formation of many individual clusters that merge upon contact, until only one

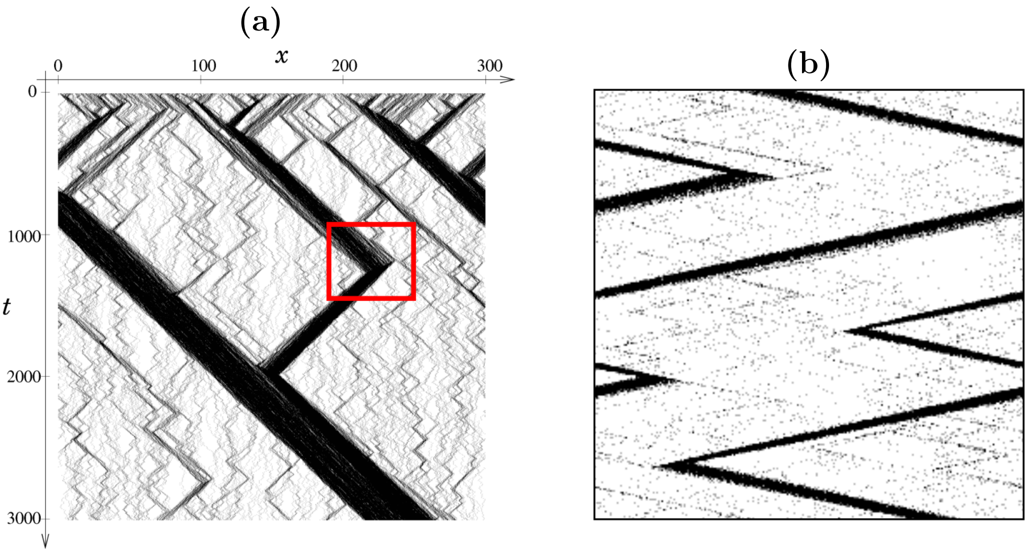

Figure 2.1: Space-time diagrams in the flocking phase. Darker gray levels represent higher particle density. **(a):** Coarsening from an initial homogeneous disordered state leading to a single remaining aggregate in the model of [Czirók *et al.* 1999]. The red square indicates a reversal. **(b):** Aggregate performing reversals in steady state in the model of [O'Loan & Evans 1999].

macroscopic aggregate remains. The coarsening exhibits clear signs of reversals (See for instance the red square in Fig. 2.1). Similarly, on the right, the model of [O'Loan & Evans 1999] features a moving cluster performing reversals in steady state. This phenomenology is well captured by the set of stochastic partial differential equations derived by [Laighléis *et al.* 2018] from microscopic dynamics very similar to [O'Loan & Evans 1999]. Indeed, these equations successfully reproduce the alternating order and the generic nature of such a continuum description highlights the prevalence of reversals in one-dimensional collective motion.

With the numerical evidences available at that time, Czirók *et al.* were led to believe that the discrete orientational symmetry was spontaneously broken, as they did not witness reversals of the macroscopic aggregate. Running longer simulations, O'Loan & Evans observed the alternating order and reported an average time separating two reversals scaling as $\log L$, with L the system size. Such a diverging time could give the impression that the symmetry is spontaneously broken, but [O'Loan & Evans 1999, Solon & Tailleur 2013] showed that it is not the case, through a scaling argument that we will make more precise later in this chapter. Apart from their mean reversal time, the properties of the aggregates remain poorly understood. We will study them in details in this chapter. Note that although the transition to collective motion was reported to be continuous in early papers [Czirók *et al.* 1999, O'Loan & Evans 1999], it was found to be discontinuous in [Solon & Tailleur 2013], a fact that is somewhat hidden by reversals.

By incorporating centering interactions that promote movement towards dense regions in the model of [O'Loan & Evans 1999], [Raymond & Evans 2006] observed a new phase composed of "dipoles". These dense, localized structures emerge through the centering interaction and undergo a slow coarsening process towards a single large dipole. In this chapter, we report the existence of such dense and static structures appearing because of the sole interplay of alignment and self-propulsion.

2.1.2 Experimental relevance

The group of [Buhl *et al.* 2006] studied locusts marching in a quasi-1d ring (see Fig. 2.2a). Locusts tend to align their direction of motion with the locusts in front of them, as they try to eat one another. The experiment showed that, at high enough locust density, the assembly moves coherently, stochastically reversing its direction of motion (see Fig. 2.2b). [Yates *et al.* 2009] confirmed these spontaneous directional switching and provided arguments rationalizing the mean reversing time for groups of a few dozen of locusts. Reversals of collective motion therefore constitute a generic feature of 1d ordering active systems, extending beyond numerical models. More recently, self-propelled droplets in a one-dimensional microfluidic channel [Illien *et al.* 2020] have been studied in details, exhibiting collective motion through a local alignement resulting from their collisions. The group properties of cells confined to 1d racetracks [Bertrand *et al.* 2021] have also been investigated. The asymmetric aligning interaction due to cell-cell collisions destroys large scale clustering and ordering, leading instead to a liquid-like microphase of cell clusters of finite size and short lived polarity.

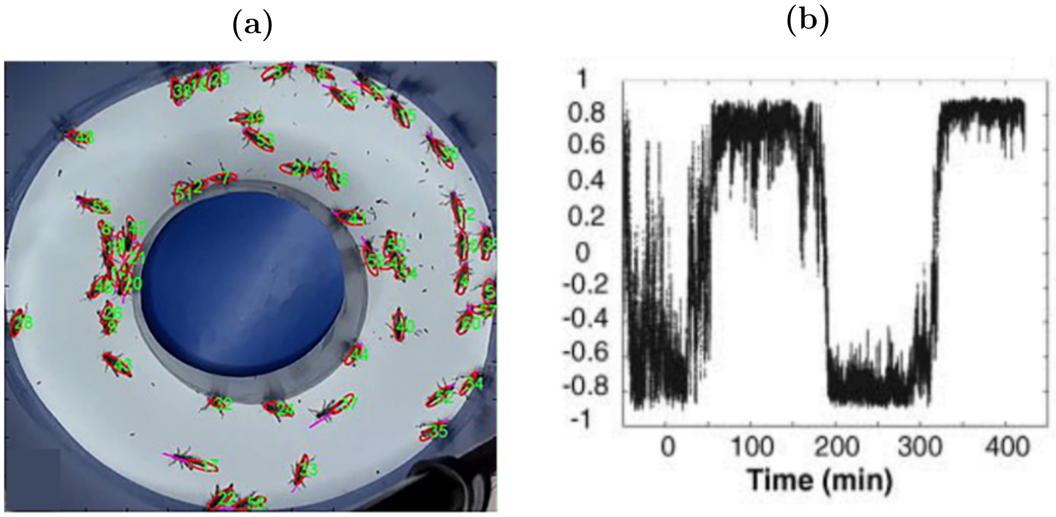

Figure 2.2: **(a):** Locusts evolving in a circular arena, making it a quasi-1d setup. **(b):** Reversals of the collective motion, captured by alternating values of the order parameter. Adaptated from [Buhl *et al.* 2006].

2.1.3 A liquid-gas phase separation

In this chapter, we analyze the 1d version of the active Ising model (AIM), first introduced in [Solon & Tailleur 2013]. This lattice model only involves ferromagnetic alignment and self-propulsion, with no excluded volume or other interaction. Consistently with previous studies considering different implementations of the same ingredients [Czirók *et al.* 1999, O'Loan & Evans 1999, Dossetti 2011, Laighléis *et al.* 2018, Sakaguchi & Ishibashi 2019], we observe a transition from a disordered state to a flocking state featuring a single moving aggregate, which stochastically reverses its direction of motion.

In this chapter, we will show that the transition is similar to the liquid-gas coexistence observed in [Solon & Tailleur 2013, Solon & Tailleur 2015], although the flocks are prevented to relax to the phase-separated state by reversals. We show this by analyzing the shape of the aggregates and its evolution in time. Computing the full statistics of reversal times, we are able to explain the logarithmic scaling with system size of the average reversal time first observed in [O'Loan & Evans 1999]. We also measure and explain how the reversal time varies with all parameters of the model. In addition, at low temperature and/or hopping rate, when alignment dominates over self-propulsion, we encounter a new type of structure that we term “asters”. These asters are static objects composed of two highly localized peaks of opposite magnetization that exchange particles back and forth. We first account for the remarkable stability of these structures by solving exactly the dynamics of a single aster at zero temperature. We then discuss the finite-temperature coarsening of asters and show the existence of two possible scenarios leading either to macroscopic condensation or to an extensive number of asters possessing a characteristic size. Finally, we derive the steady-state profile of the asters in the mean-field approximation, which compares favorably with numerical measurements.

This chapter is organized as follows: In Sec. 2.2 we first define the AIM and present the three phases observed in our simulations (disordered, flocking and aster phases) with phase diagrams for the main parameters of the model. We then investigate the two non-trivial phases. In Sec. 2.3, we successively look at the shapes of flocks and how they evolve in time (Sec. 2.3.1), the statistics of reversals (Sec. 2.3.2) and the two distinct regimes observed at small and large velocity (Sec. 2.3.4). We then investigate the aster phase in Sec. 2.4. We first derive an exact solution for the dynamics of an aster at zero temperature in Sec. 2.4.1, before looking at the coarsening dynamics at small-but-finite temperature in Sec. 2.4.2 and investigating the aster shape in Sec. 2.4.3. Finally, we examine in Sec. 2.5 the robustness of our results by comparing to those of O’Loan and Evans in Sec. 2.5.1, and by considering an off-lattice version of the model in Sec. 2.5.2.

2.2 The 1d Active Ising Model

In the AIM [Solon & Tailleur 2013], each particle carries an Ising spin $s = \pm 1$ and undergoes biased diffusion: A particle with spin s hops to the next site on its right (resp. left) at rate $D(1 + s\varepsilon)$ (resp. $D(1 - s\varepsilon)$). The parameter $\varepsilon \in [0, 1]$ controls the asymmetry between the passive limit $\varepsilon = 0$ and fully asymmetric hoppings $\varepsilon = 1$, while D controls the overall hopping frequency. On average, a particle thus moves at a speed $v = 2D\varepsilon a$ in the direction set by the sign of its spin, a being the lattice spacing. Finally, on a site i occupied by n_i^+ and n_i^- particles with spins $+1$ and -1, respectively, a particle of spin s flips at a rate

$$W(s \to -s) = \omega_0 \, e^{-\beta s \frac{m_i}{\rho_i}} \ , \tag{2.1}$$

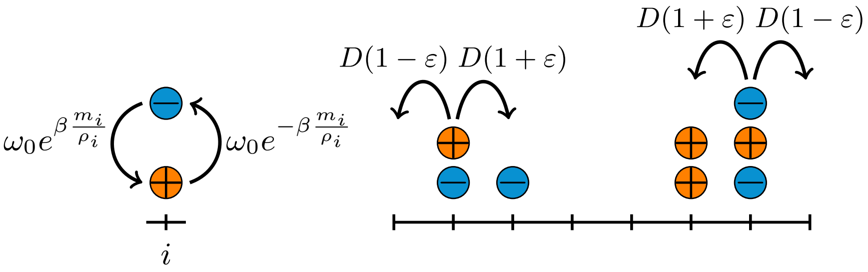

Figure 2.3: Sketch of the two possible actions in the AIM and their rates of occurrence: The particles align ferromagnetically with the particles on the same site (left) and undergo a diffusion biased by the sign of their spin (right).

where $\rho_i = n_i^+ + n_i^-$ and $m_i = n_i^+ - n_i^-$ are the local density and magnetization. Those rates are chosen such that, in absence of hopping, each site constitutes a fully-connected Ising model with Hamiltonian $-m_i^2/(2\rho_i)$ undergoing Glauber dynamics at inverse temperature $\beta = 1/T$. The two actions (hopping and flipping spin) and the associated rates are depicted in Fig. 2.3. Note that the model is out of equilibrium even at $\varepsilon = 0$ since the symmetric hopping dynamics is insensitive to the changes of the total Hamiltonian $H = -\sum_i m_i^2/(2\rho_i)$ [Solon & Tailleur 2015].

In the rest of the chapter, we choose without loss of generality $\omega_0 = a = 1$ thus fixing the time and space units. We study the system as a function of the parameters β (or T), D, ε and the average density $\rho_0 = N/L$.

2.2.1 Numerical implementations

Our simulations relied either on discrete time steps with random sequential updates or on an exact continuous-time Monte Carlo algorithm. The discrete-time simulations are implemented using random sequential updates: Particles are chosen at random and updated sequentially. For each update, the time is increased by dt/N. Denoting by i the site of the chosen particle and by s its spin, the particle either hops, flips its spin, or does nothing with probabilities:

$$\begin{cases} \text{Proba(hop to site } i+1\text{):} & D(1+s\varepsilon)dt \\ \text{Proba(hop to site } i-1\text{):} & D(1-s\varepsilon)dt \\ \text{Proba(spin flips):} & \omega_0 e^{-\beta s \frac{m_i}{\rho_i}}\, dt \\ \text{Proba(no update):} & 1 - 2Ddt - \omega_0 e^{-\beta s \frac{m_i}{\rho_i}}\, dt \end{cases} \tag{2.2}$$

Our continuous time simulations were implemented as follows. For each particle i, with spin s_i, we define an escape rate $r_i = 2D + \omega_i$, where ω_i is the rate at which s_i flips into $-s_i$. At time 0, we sample a time τ_i for each particle according to $P(\tau_i) = r_i e^{-r_i \tau_i}$. The algorithm then goes iteratively over the following loop:

1. Set the simulation time to $t = \tau_j$ where $\tau_j = \inf_i \tau_i$.

2. Update particle j using tower sampling: pull a random number $\eta \in [0, r_j]$. If $\eta < D(1 - s_j \varepsilon)$, the particle hops to the left. If $D(1 - s_j \varepsilon) < \eta < 2D$, the particle hops to the right. Otherwise, the spin flips: $s_j \to -s_j$.

3. Update any r_k that has changed because of step 2 and sample new τ_k's according to $P(\tau_k) = r_k e^{-r_k(\tau_k - t)} \Theta(\tau_k - t)$. A new τ_j is also sampled, whether or not r_j has changed.

To make step 1 as efficient as possible, we use a heap structure, which is a binary sorting tree consisting in a root and two sub heaps. The heap is such that the time stored at a root is always smaller that the times stored at the roots of the two sub heaps. Finding the smallest time then has a cost of $\mathcal{O}(1)$ whereas the reorganization of the heap due to step 3 has a cost $\mathcal{O}(\log_2 N)$.

The advantages of the continuous-time algorithm are that it is exact, being a generalization of the Gillespie algorithm [Gillespie 1976], and that there is no rejection. At every move, however, several new times τ_k have to be sampled, the heap has to be reorganized, and the data structure is much heavier than for the discrete-time algorithm. As a result, the discrete-time algorithm is always more efficient when the rejection rate is low. For our simulations, the discrete-time simulations were faster at high temperatures, whereas the continuous-time simulations were faster at lower temperature (see Fig. 2.4) and we used them accordingly.

2.2.2 The three phases

Looking at the phase diagrams in the $D - T$ (Fig. 2.5a) and $\rho_0 - T$ (Fig. 2.5b) planes, we see that, as expected, the system is disordered at high temperature. Density and magnetization are homogeneous and fluctuate, respectively, around ρ_0 and 0. Decreasing temperature, the system reaches a flocking phase which consists, at long times, of a single dense ordered aggregate moving ballistically in

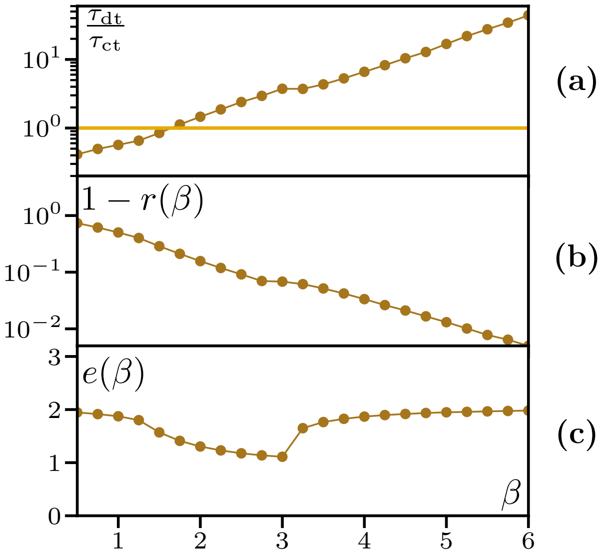

Figure 2.4: Comparison between discrete- and continuous-time algorithms. **(a):** Ratio between the cpu time used for a discrete-time simulation, $\tau_{\rm dt}$, and a continuous-time simulations, $\tau_{\rm ct}$, as β is varied. The discrete-time simulation is faster at large temperature but its efficiency decreases exponentially with β. **(b):** The rejection rate of the discrete-time algorithm, $r(\beta)$, converges exponentially to $r(\beta) = 1$ as β increases. **(c):** The average escape rate per particle, $e(\beta)$, shows little variation as β is varied and remains close to $r \simeq 2D + \omega_0$. The dip for intermediate β corresponds to the flocking phase where most particles are aligned. Parameters: $D = 0.5$, $\varepsilon = 1$, $\omega_0 = 1$, $L = 500$, $\rho_0 = 10$. In panel **(a)**, the system is simulated up to a final time $t = 110\,000$.

a disordered gas, as illustrated on the snapshot shown in Fig. 2.6a. It moves to the right or left if the particles are polarized positively of negatively. As illustrated in Fig. 2.8 and detailed later, these flocks have a rather complex dynamics: They diffusively widen as they travel, and undergo stochastic reversals during which they “regroup” into a very thin condensate and their magnetization changes sign. These dynamics, together with the coarsening leading to a single aggregate, are displayed in the space-time diagram of Fig. 2.6c, and form the topic of Sec. 2.3. Note that transient, finite-size aggregates can be observed to move ballistically in the gas region surrounding the main aggregate (see Fig. 2.6c).

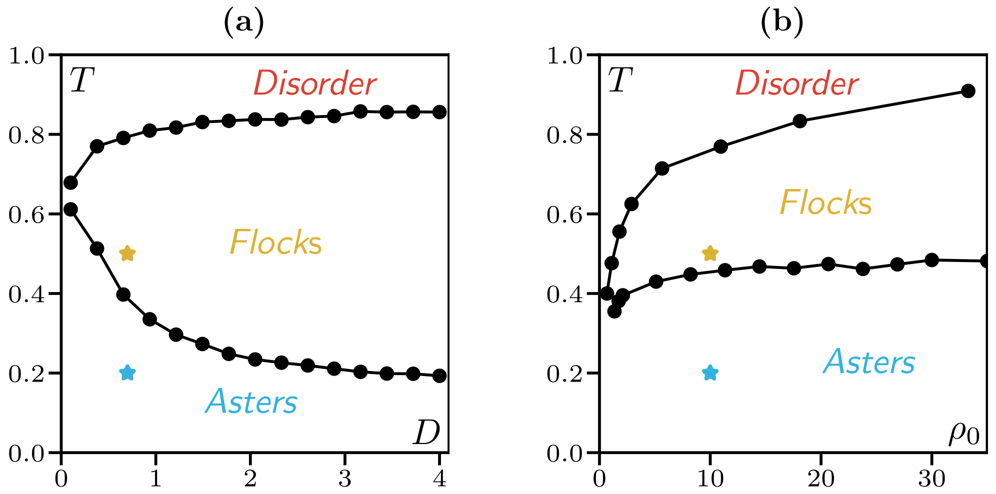

Figure 2.5: Phase diagrams in the (hopping-rate, temperature) plane at $\rho_0 = 10$ and $\varepsilon = 0.7$ **(a)** and (density, temperature) plane at $D = 0.5$ and $\varepsilon = 0.7$ **(b)**. The stars indicate the parameters used in Fig. 2.6 to illustrate the phases. The line separating the disordered and flocking phases in the (ρ_0, T) plane is set by the density $\rho_g(T)$ of the gas in the flocking states at temperature T (see Sec. 2.2.3). The other lines are determined using the threshold $\langle|\tilde{m}|\rangle = 0.05$ on the time-averaged magnetization per particle, which is non-zero only in the flocking phase. Data obtained in a system of size $L = 500$; increasing system size displaces the lines only within the size of the symbols.

Finally, at lower temperatures, the system exhibits what we have called asters, that are illustrated in the snapshot shown in Fig. 2.6b: Sharp peaks of positive and negative magnetizations, spread over a few sites, face each other. These structures are long-lived, despite the absence of repulsive interactions. As shown on the space-time plot Fig. 2.6d, asters can dissolve on long time scales, leading to a coarsening process. Our study of this phase, which was not observed in previous studies of the AIM [Solon & Tailleur 2013, Solon & Tailleur 2015], is in Sec. 2.4.

To distinguish between the three phases, we introduce an order parameter, the magnetization per particle $\tilde{m} = \sum_{i=1}^{N} s_i/N$, which is non-zero at long times only in the flocking phase where it alternates between a positive and a negative value because of reversals.

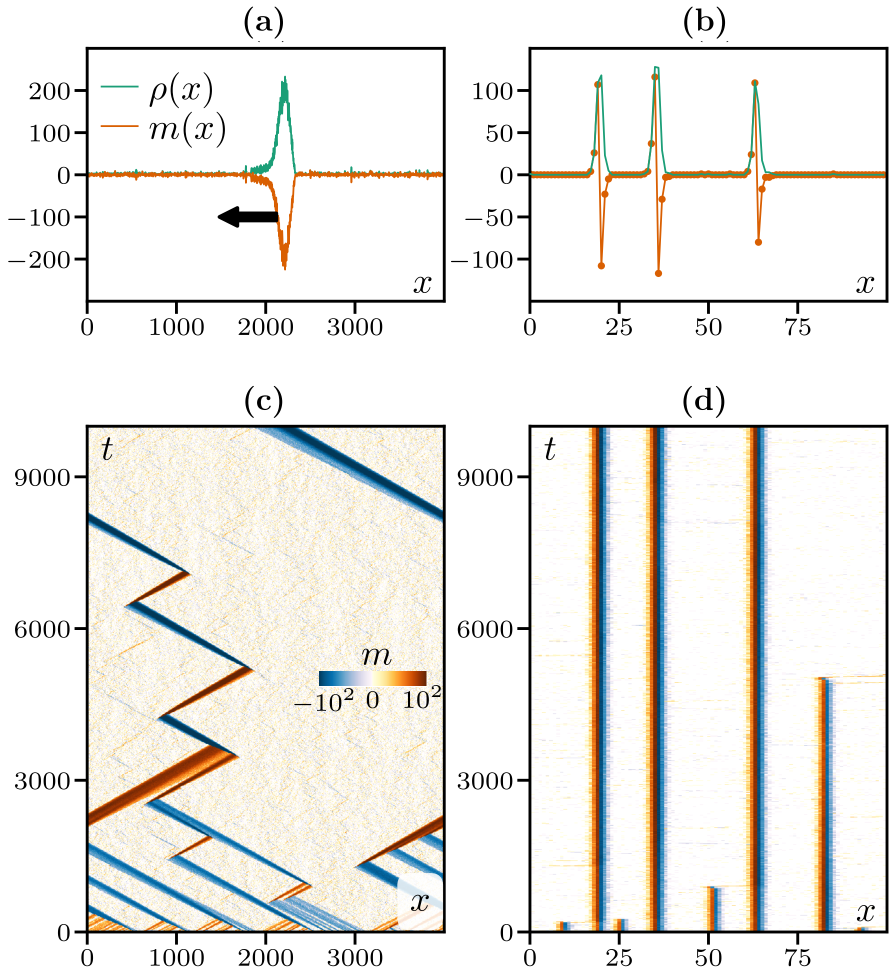

Figure 2.6: **(a-b):** Instantaneous density and magnetization fields at the final time $t = 10^4$ of the space-time diagrams shown in (c-d). **(c-d):** Space-time diagrams in the flocking (c) and aster (d) phases. The parameters, indicated by stars in the phase diagrams of Fig. 2.5, are $\rho_0 = 10$, $\varepsilon = 0.7$, $D = 0.5$ and $\beta = 2, 5$ for the F and A phases, respectively. The system sizes $L = 4000$ (Flocking phase) and $L = 100$ (Asters phase) were chosen for legibility. Simulations are started from a homogeneous disordered initial condition.

2.2.3 Fate of the liquid-gas transition scenario

In [Solon & Tailleur 2013], the transition to collective motion in polar flocking models has been shown to be akin to a liquid-gas transition between a disordered

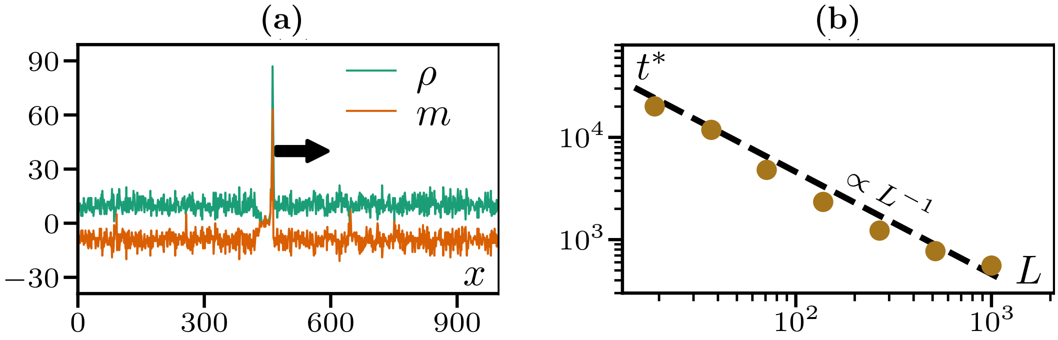

Figure 2.7: **(a) :** Instantaneous profile showing a fluctuation propagating through the homogeneous ordered phase. **(b) :** Average life time t^* of the metastable homogeneous ordered phase. Parameters: $L = 1000$ (left), $\beta = 2$, $\varepsilon = 1$, $D = 0.5$ and $\rho_0 = 10$.

gas and a polar ordered liquid [Solon & Tailleur 2013, Solon & Tailleur 2015]. The form of the phase coexistence depends on the symmetry of the spins: for the Vicsek model with continuous spins one observes microphase separation with an extensive number of dense ordered traveling bands having a characteristic size, while in the AIM, which has a discrete spin symmetry, one obtains phase separation between two macroscopic domains [Solon *et al.* 2015d].

In the same way, in $1d$ one observes the coexistence of an ordered flock with a disordered gas. Although, because of fluctuations it can easily be mistaken for a continuous transition [Czirók *et al.* 1999, O'Loan & Evans 1999], the transition between the disordered phase and the flocking state also shows a phase-separation scenario. In particular, the transition exhibits metastability and the associated negative peaks in the Binder fourth-order cumulant for large (but finite) systems which arise from discontinuous nucleation events [Binder & Landau 1984, Solon & Tailleur 2013]. In addition, the density in the gas is independent of the average density ρ_0 in the system, consistently with a liquid-gas separation.

Looking at the phase diagram in the (ρ_0, T) plane (Fig. 2.5b), a second transition line to a homogeneous ordered liquid is conspicuously absent. This is because, contrary to what happens in [Solon & Tailleur 2013], fluctuations destroy the homogeneous ordered phase in $1d$. Indeed, as in [Raymond & Evans 2006], we see that, if we prepare the system in this state, it is metastable but eventually gets destabilized by a fluctuation. As shown in the left panel of Fig. 2.7, a local fluctuation of the opposite magnetization propagates through the entire system, until only a localized flock remains.

The dependance on system size of the time t^* for such a fluctuation to happen can be easily understood: a fluctuation happens at a finite rate ν per unit time and space so that the total nucleation rate per unit time is νL. The nucleation time t^* is thus proportional to L^{-1} consistently with the numerical measurements reported in Fig. 2.7b. For a large enough system size, the ordered phase is destabilized very quickly.

The form of the phase coexistence is also altered by fluctuations in $1d$. Only the gas density ρ_g is easily defined and separates the disordered and flocking state in the phase diagram Fig. 2.5b. Below, we study how flocks tend to relax to a phase-separated state as in [Solon & Tailleur 2013] but are prevented to do so by reversals.

2.3 Flocks and Reversals

In the steady state of the flocking phase, the system presents a single ordered aggregate: the flock. As illustrated in Fig. 2.8, it moves ballistically but its shape evolves continuously: initially narrow and sharp, it progressively spreads. After some time, a protrusion with a constant density develops at the leading edge, growing out of the main peak. The most striking feature of flocks is that they reverse: Once the flock is sufficiently spread, a fluctuation that flips the first few sites at the front can become large enough that it flips systematically all the remaining flock particles. This leads to a full reversal of the flock, whose dynamics then resets, starting with the same initial sharply peaked shape but with the opposite magnetization (compare Fig. 2.8a and f).

2.3.1 Shape of a flock

To separate the trend from fluctuations in the evolution of the flock shapes, we average them over many realizations and construct the average flock shape at time t after their last reversal. To do so, we define an origin of time for each reversal and spatially align flocks of similar age t.

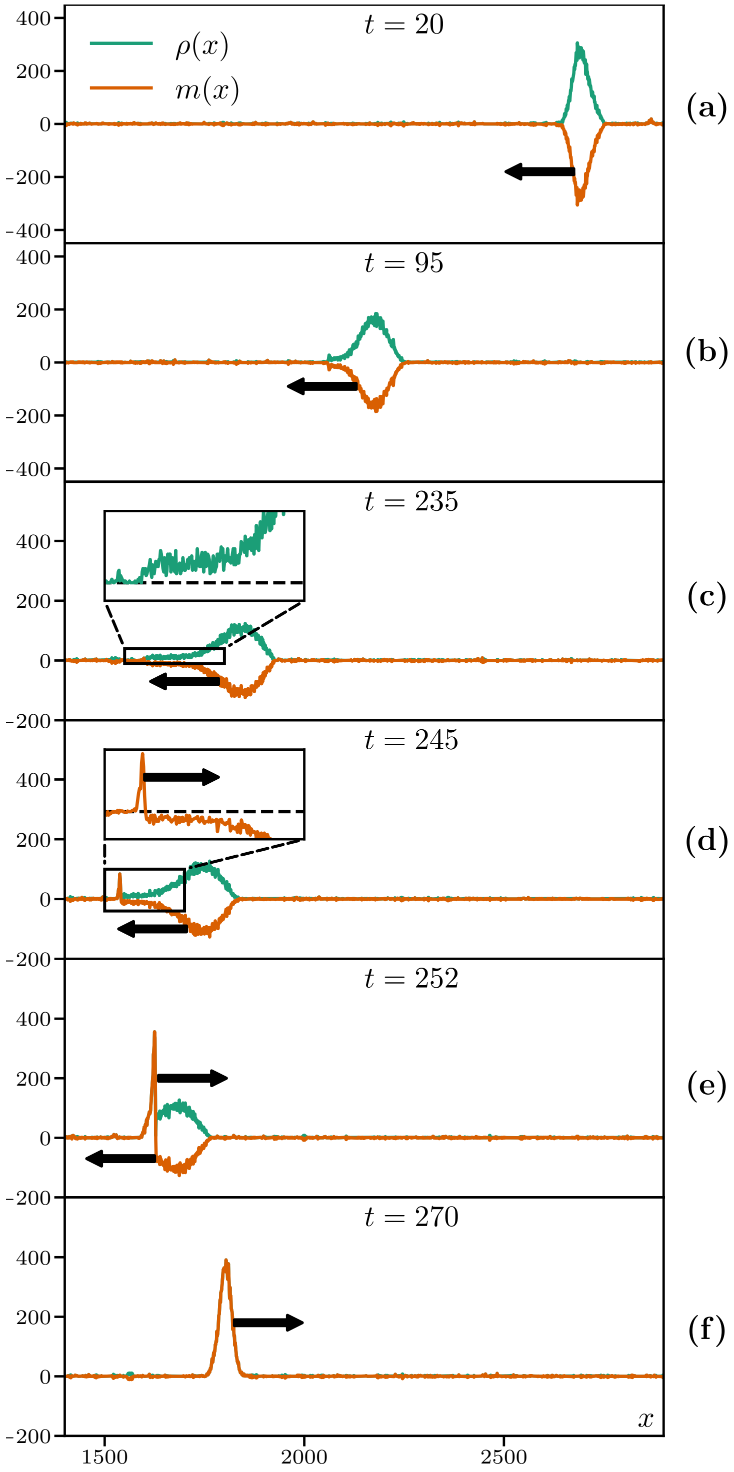

Figure 2.8: Instantaneous density (green) and magnetization (orange) profiles during the spreading and the reversal of a flock. An initially peaked aggregate **(a)** spreads while propagating **(b)**. After some time, it develops a protrusion at the leading edge **(c)**. A spontaneous fluctuation at the front **(d)** can propagate inside the flock and progressively flip all the particle orientations **(e)**. Finally, just after the reversal **(f)**, one is left with a flock with the same shape as in **(a)** (which was taken just after the previous reversal), albeit with a reversed magnetization. Time is counted from the previous reversal. Parameters: $L = 4000$, $\beta = 2$, $\varepsilon = 1$, $D = 0.5$, $\rho_0 = 10$.

The magnetization per spin $\tilde{m}$ flips from a well defined value $\tilde{m}_0$ to $-\tilde{m}_0$ during a reversal. We define the time origin of each reversal as the time when $\tilde{m}(t) = -0.7\tilde{m}_0$. (The 0.7 factor allows for a robust detection, but other values are of course possible.) Flocks of the same age are localized at different positions on the lattice. A simple idea to align them so as to be able to average their shape would be to align their densest sites (the green dot in Fig. 2.9a) to try and match their peaks. However, this leads to large fluctuations that artificially smear out the flock shapes. Instead, we use the rear edges of the flocks, which are always very sharp. The precise alignement point i_{align} (purple dot in Fig. 2.9a) is determined in the following way. We first localize the site $i_{\max}$ where the density is maximal (green dot). Going backward from there, i_{back} is the first site where the magnetization changes sign. We then calculate $\bar{m}$ the average magnetization per site over the region of size $2\ell + 1$ centered on $i_{\max}$, where $\ell \equiv |i_{\max} - i_{\text{back}}|$: the limits of this region are indicated by the two vertical dashed lines. Starting from i_{back}, we then find the first site i_{align} such that $m_{i_{\text{align}}} > \bar{m}/4$. All right-going flocks are then aligned such that their site i_{align} coincide. Left-going flocks are transformed by $m_i \to -m_i$ and $i \to L - i$ and then run through the same algorithm.

This averaging procedure leads to satisfying results: As shown in Fig. 2.9b, flocks superimpose with little spread along most of their profiles, allowing to extract meaningful average shapes. Note however that the precise position of the leading edge fluctuates, leading to an average profile whose leading edge is smoother than that of the instantaneous ones.

The mean shape allows us to quantify the dynamics of the flocks: they contain a main peak which spreads continuously and, after some time, a protrusion with constant density and magnetization which develops at their leading edge (see Fig. 2.9c). We now discuss both of these features.

As shown in Fig.2.9d, the main peak of the flock at a given age is proportional to the system size and contains a macroscopic fraction of the particles. The top of the peak is well approximated by a Gaussian with a variance σ^2 that is independent of system size and grows linearly in time (Fig. 2.10a). In addition, the peak propagates at a constant speed v_p, defined as the speed of the maximum of the density profile, which is smaller than the speed v of individual particles (Fig. 2.10b).

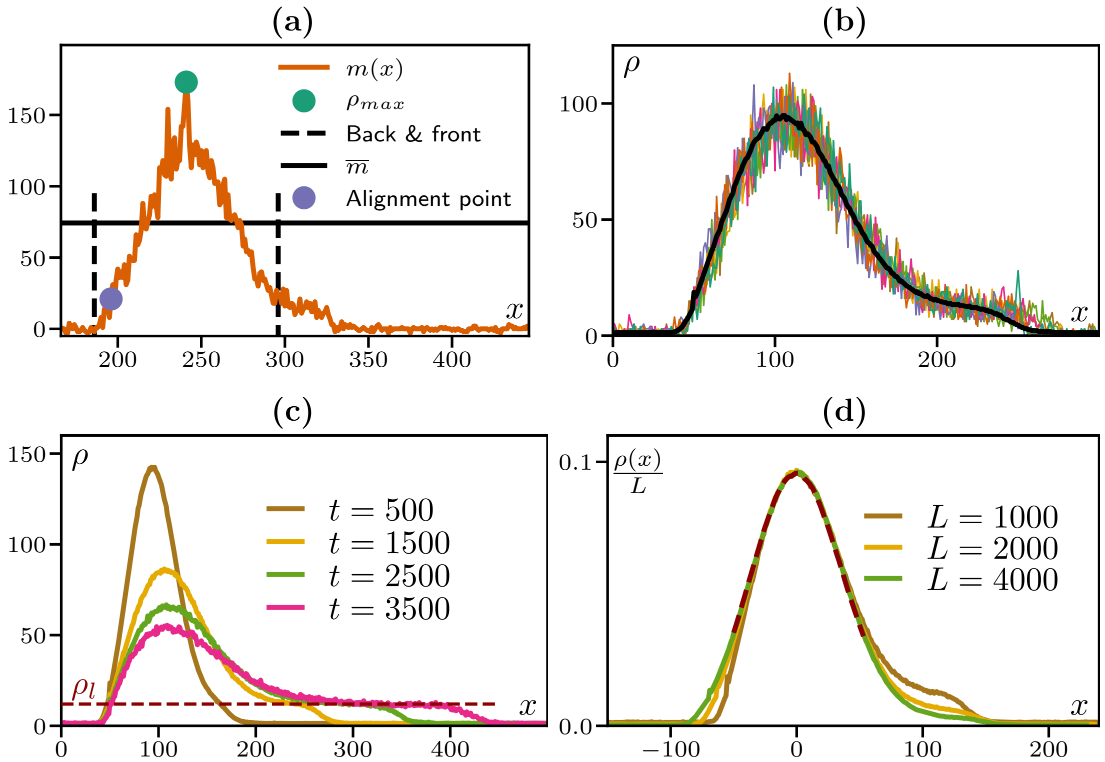

Figure 2.9: **(a):** Sketch of the procedure to align flocks of the same age as described in the text. **(b):** Seven representative instantaneous density profiles (colors) superimposed to the average profile (thick black line). **(c):** Evolution of the averaged density profile as a function of time. The red dashed line is a fit to the density ρ_ℓ of the protrusion. **(d):** Average density profiles at $t = 1200$ showing that the main peak is extensive in system size. The red dashed line is a Gaussian fit used to compute the variance σ^2 in 2.10a. Parameters: $\rho_0 = 10$, $\beta = 2$, $\varepsilon = 1$, $D = 0.5$, $t = 1000$ (b,d), $L = 1000$ (b,c)

Since the peak contains a high density of particles, we expect it to be well described by a mean-field theory that we now construct starting from the microscopic dynamics, following [Solon & Tailleur 2015]. To do so, we first write exact equations for the average density and magnetization $\langle \rho_i \rangle$ and $\langle m_i \rangle$ on site i, the

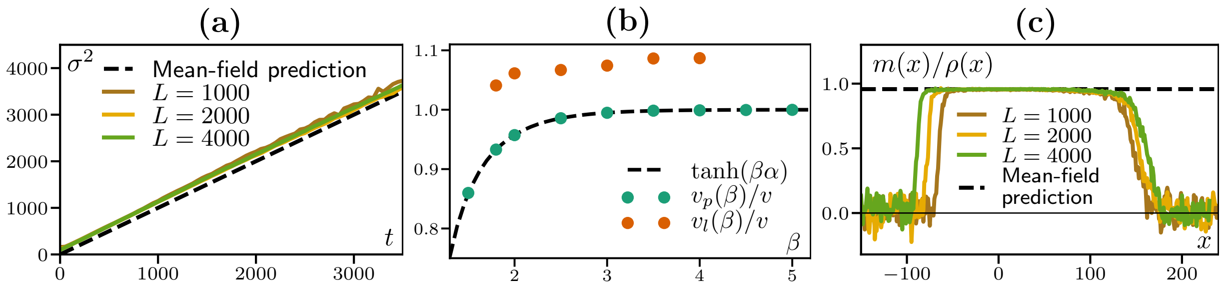

Figure 2.10: **(a):** Variance of the main peak. The dashed line is the mean-field prediction $\sigma^2 = 2Dt$. **(b):** Speeds v_p of the main peak (computed as the speed of the maximum) and v_l of the protrusion (computed as the speed of the point at $\rho = \rho_\ell/2$ in the average profiles) divided by the self-propulsion speed $v = 2D\varepsilon$. The dashed line is the mean-field prediction. **(c):** Average polarization profile $m(x)/\rho(x)$. The dashed line is the mean-field prediction, solution of $m/\rho = \tanh(\beta m/\rho)$. Parameters: $\rho_0 = 10$, $\beta = 2$, $\varepsilon = 1$, $D = 0.5$, $t = 1000$ (b,c), $L = 5000$ (b).

average being over realizations of the stochastic microscopic dynamics. This gives

$$\partial_t\langle\rho_i\rangle = D\langle\rho_{i+1} + \rho_{i-1} - 2\rho_i\rangle - \tfrac{v}{2}\langle m_{i+1} - m_{i-1}\rangle \tag{2.3}$$

$$\begin{aligned}\partial_t\langle m_i\rangle &= D\langle m_{i+1} + m_{i-1} - 2m_i\rangle - \tfrac{v}{2}\langle\rho_{i+1} - \rho_{i-1}\rangle \\ &\quad + 2\left\langle \rho_i \sinh\left[\beta\tfrac{m_i}{\rho_i}\right] - m_i\cosh\left[\beta\tfrac{m_i}{\rho_i}\right]\right\rangle\end{aligned} \tag{2.4}$$

with $v = 2D\varepsilon$. These equations are not closed since Eq. (2.4) involves the average of a nonlinear term. However, in the mean-field approximation where fluctuations and correlations are neglected, $\langle f(x)\rangle = f(\langle x\rangle)$ for any function f. Taking in addition the continuous limit, Eqs. (2.3)-(2.4) may be rewritten as

$$\partial_t\rho = D\partial_x^2\rho - v\partial_x m \tag{2.5}$$

$$\partial_t m = D\partial_x^2 m - v\partial_x\rho - 2m\cosh\left[\beta\tfrac{m}{\rho}\right] + 2\rho\sinh\left[\beta\tfrac{m}{\rho}\right]. \tag{2.6}$$

with $\rho(x = ia) = \langle\rho_i\rangle$ and similarly for m.

Contrary to the density field which is a conserved quantity, $m(x,t)$ is a fast mode which relaxes in a finite time to a value that makes the right-hand-side of Eq. (2.6) vanish. To leading order in a gradient expansion, this amounts to requiring that the interaction term in Eq. (2.6) vanishes, i.e. that $m/\rho = \tanh(\beta m/\rho)$. This thus predicts $\alpha = m/\rho$ to be the solution of $\alpha = \tanh(\beta\alpha)$, which is the value observed numerically in Fig. 2.10c except close to the edges of the flock. Using $m(x) = \alpha\rho(x)$ in Eq. (2.5), we obtain a diffusion-drift approximation for the density field:

$$\partial_t \rho = D\partial_x^2 \rho - v\tanh(\beta\alpha)\partial_x \rho. \tag{2.7}$$

The diffusion and drift coefficients read from Eq. (2.7) both match numerical measurements as seen in Fig. 2.10a-b.

Let us now turn to the protrusion appearing at the front of the flock. Since reversals start at the leading edge, this protrusion is expected to play an important role in the dynamics. Contrary to the main peak, it has a fixed height (in density and magnetization) independent of time (See Fig. 2.9b) and system size (See Fig. 2.11a). Its velocity results both from the persistent hop of the particles and from the recruitment of new sites at the leading edge due to the aligning dynamics. This explains why the leading edge of the protrusion moves with a speed larger than the individual particle speed v (Fig. 2.9b), much like the polar bands of the coexistence region in [Solon & Tailleur 2015]. The front speed is thus also larger than the drift velocity of the peak ($v_p = v\tanh\beta\alpha$), which explains the increase of the protrusion length as time passes. All this suggests that the flock is trying to relax to the fixed density ρ_ℓ of the homogeneous ordered liquid but is prevented to do so by the reversals. This is confirmed by choosing parameters such that the full phase separation can be observed before a reversal happens. This can be achieved by increasing D; one then observes the relaxation from a peaked aggregate (Fig. 2.11b) to a relatively long-lived phase-separated profile (Fig. 2.11c).

2.3.2 Reversals

The average time between two reversals, $\langle\tau\rangle$, shows a logarithmic increase with system size $\langle\tau\rangle \propto \log(L)$ (Fig. 2.12a). This is in line with previous results obtained by O'Loan and Evans for a different model [O'Loan & Evans 1999, Raymond & Evans 2006], which considers self-propelled particles on a $1d$ lattice aligning via a Voter-type majority rule.

To understand the physical origin of this logarithmic scaling observed in our model, we consider $P(\tau)$, the distribution of inter-reversal times. As shown in

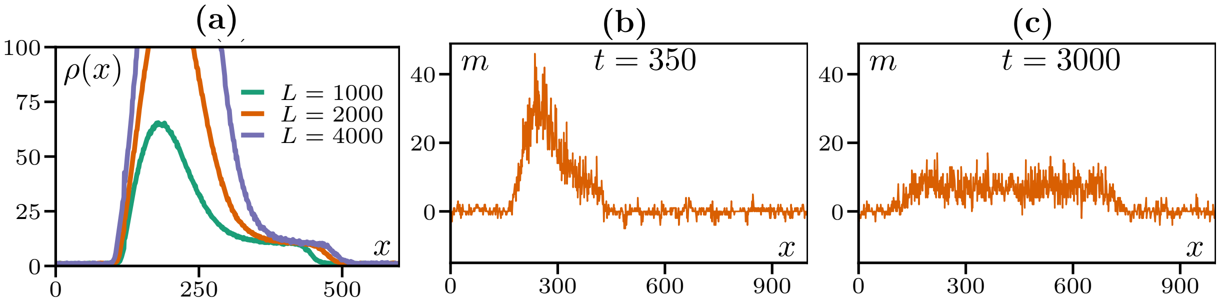

Figure 2.11: **(a):** Density profiles at time $t = 3000$, showing a protrusion of density independent of system size. Instantaneous density profile at times $t = 350$ **(b)** and $t = 3000$ **(c)** after the last reversal. The profile relaxes to a long-lived phase-separated state, whose shape is stationary (until the next reversal occurs). Parameters: $\rho_0 = 10$ (a) , $\rho_0 = 5$ (b,c), $L = 1000$ (b,c), $\beta = 2$, $\varepsilon = 1$, $D = 1$ (a), $D = 2$ (b,c).

Fig. 2.12b, it has a peak and an approximately exponential tail with a decay rate that is roughly independent of L. Increasing L, the distribution shifts slightly to the right. As shown in Fig. 2.12c, a horizontal shift by $\alpha \log L$, with α a constant, collapses reasonably well the distributions obtained for several values of L.

To better characterize the various processes at play, we compute the reversal rate $\lambda(t)$, defined via the probability $\lambda(t)dt$ that a flock of age t reverses within $[t, t + dt]$. This rate is related to the distribution $P(\tau)$ via the number of flocks $N_f(t)$ that have survived until time t from an initial population of $N_f(0)$: $\dot{N}_f(t) = -\lambda(t)N_f(t)$ so that $\lambda = -\dot{N}_f/N_f$. In addition N_f itself is related to P through $N_f(t)/N_f(0) = \int_t^\infty P(\tau)d\tau$, which yields

$$\lambda(t) = \frac{P(t)}{\int_t^\infty P(\tau)d\tau} . \tag{2.8}$$

In physical terms, Eq. (2.8) simply states that the probability that an event happens at time t is the rate of occurence of this event at time t multiplied by the probability that it did not happen before: $P(t) = \lambda(t)[1 - \int_0^t P(\tau)d\tau]$. Note that for an exponential distribution, λ equals the decay rate of the exponential. In Fig. 2.13a, we show $\lambda(t)$ computed using Eq. (2.8) for several system sizes. We see an initial rapid increase in λ, with a characteristic time that increases with system size, followed by an approximately flat plateau corresponding to the exponential tail of $P(\tau)$. As shown in Fig. 2.13b, shifting the time by $\alpha \log L$ provides

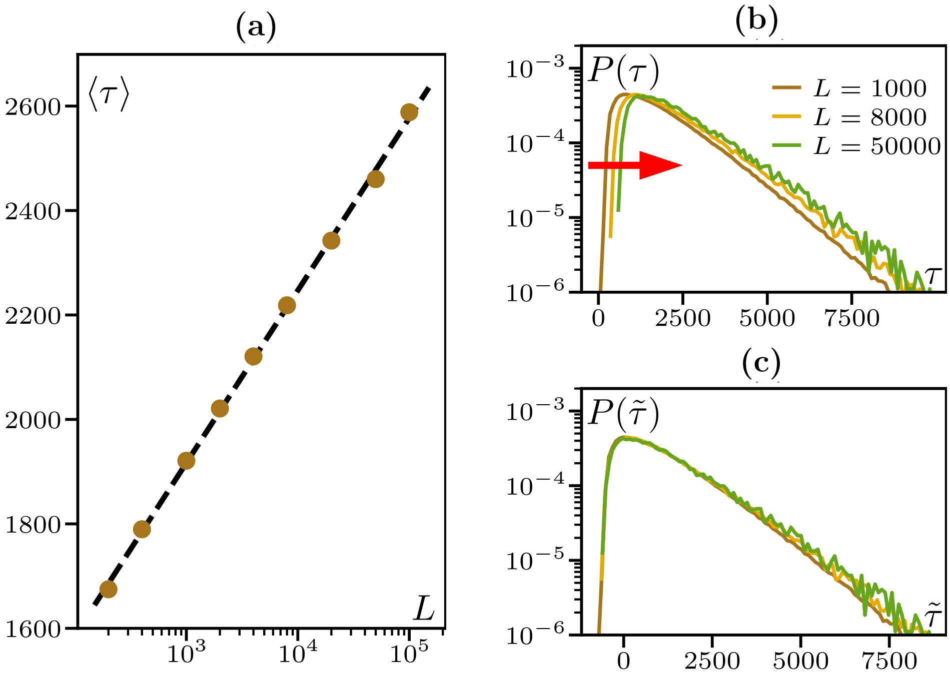

Figure 2.12: **(a):** Mean time between reversals with a fit to a logarithmic function $f(L) = a \log L + b$, leading to $a = 139$ and $b = 964$ (dashed line). **(b):** Probability density function of the reversal time τ. The red arrow emphasizes the shift of the distributions at small τ responsible for the logarithmic scaling of the mean. **(c):** Same as in (b) with an horizontal shift $\tilde{\tau} = \tau - \alpha \log L$ with $\alpha = 110$. Parameters: $\rho_0 = 10$, $\beta = 2$, $\varepsilon = 1$, $D = 0.5$.

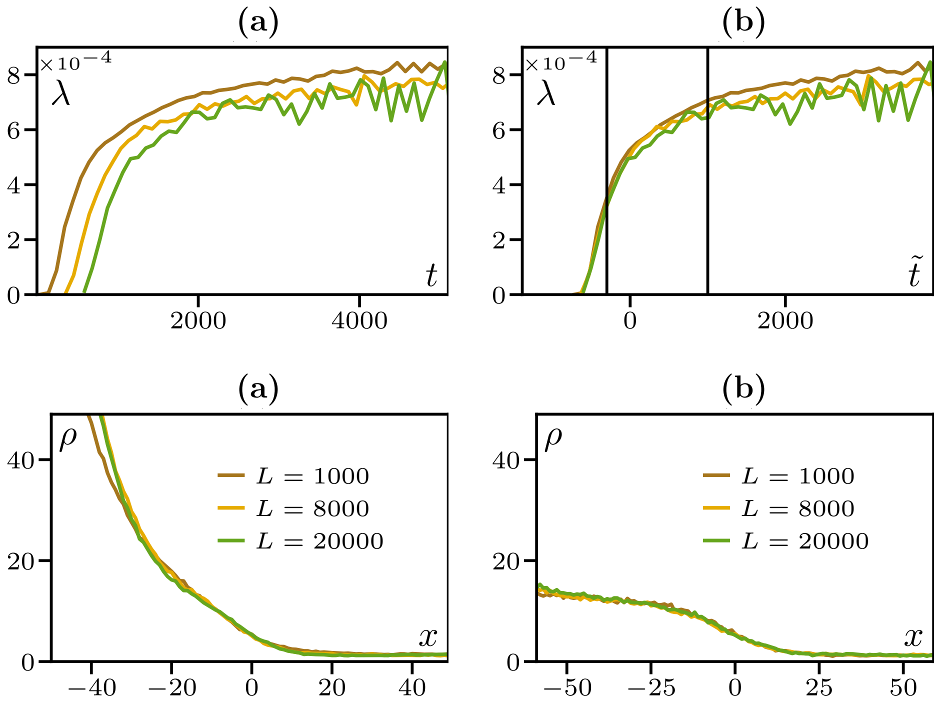

Figure 2.13: **Top:** Rate of reversal $\lambda(t)$ as a function of time since the last reversal **(a)** and with time shifted as $\tilde{t} = t - \alpha \log L$ **(b)**, $\alpha = 110$ as in Fig. 2.12. **Bottom:** Average profiles at fixed $\tilde{t}$, at $\tilde{t} = -300$ when the protrusion just begins to appear **(c)**, and at $\tilde{t} = 1000$ when it has developed **(d)**. The corresponding times are indicated by vertical lines in panel (b). The profiles are aligned on the point where $\rho = 5$. Parameters: $\rho_0 = 10$, $\beta = 2$, $\varepsilon = 1$, $D = 0.5$.

a good collapse of the curves $\lambda(t - \alpha \log L)$ measured for different system sizes, consistent with what was reported for $P(\tau - \alpha \log L)$ in Fig. 2.12.

The evolution of $\lambda(t)$ can be related to that of the shape of the flock. Reversals are initiated at the leading edge of flocks. At short times, the leading edge is very stiff so that there is little chance that a spontaneous fluctuation in the gas ahead, whose typical density is very low, triggers a reversal (Fig. 2.8a). Correspondingly, $\lambda(\tau) \to 0$ as $\tau \to 0$. At longer times two processes take place that make reversals more likely. First, flocks spread diffusively, due to the stochastic hopping of the particles. As the leading edge smoothens, it becomes more and more susceptible to fluctuations. Then, once the leading edge has sufficiently spread, its shape becomes compatible with the development of a liquid phase [Solon *et al.* 2015b]. As this liquid protrusion develops, the shape of its leading front becomes constant in time (Fig. 2.9b). The probability that a fluctuation flips the protrusion becomes time-independent, leading to a plateau value of $\lambda(t)$ at late times, independent of L.

Let us now try to rationalize the scaling form $P(\tau - \alpha \log L)$ and $\lambda(t - \alpha \log L)$ reported in Figs. 2.12 and 2.13. We see in Figs. 2.13c-d that the leading edges of the density profiles also collapse under the same shift. To account for this, we compute the time t^* it takes for the profile to reach a given slope $-k^*$ at a given density ρ_ℓ:

$$\rho(x,t^*) = \rho_\ell; \quad \partial_x \rho(x,t^*) = -k^*. \tag{2.9}$$

We first focus on the early-time dynamics, where we expect a Gaussian spreading in the co-moving frame. There, the density profile can be approximated as

$$\rho(x,t) = \frac{N_0}{\sqrt{2\pi D t}} e^{-\frac{x^2}{4Dt}} \ , \tag{2.10}$$

where D is an effective diffusion coefficient and $N_0 = L\rho_0$ is the number of particles in the aggregate. Denoting by x^* the position at which the density profile equals ρ_ℓ, we find that the slope satisfies $k^* = x^* \rho_\ell/(2Dt)$ while x^* is given by

$$x^* = 2\sqrt{Dt}\sqrt{\log \frac{N_0}{\rho_\ell} - \frac{1}{2}\log(2\pi D t)} \ . \tag{2.11}$$

The slope as a function of time then satisfies

$$k(t) = \rho_\ell \sqrt{\frac{\log \frac{N_0}{\rho_\ell}}{Dt}\left(1 - \frac{1}{2}\frac{\log 2\pi D t}{\log \frac{N_0}{\rho_\ell}}\right)}. \tag{2.12}$$

At early times and large system sizes, $\log(2\pi D t) \ll \log \frac{N_0}{\rho_\ell} \propto \log L$, so that k is a function of $t/\log L$. Note that since the reversals happen at the leading edge, it is natural to assume that the rate of reversal is controlled by the steepness of the forefront, a steeper front being more resistant to fluctuations. Quantifying the steepness by k, this would lead to scaling forms $P(\tau/\log L)$ and $\lambda(t/\log L)$ during the early Gaussian spreading of the flock.

After a time t_{prot} that can be estimated as the inflexion point in Fig. 2.13a, the protrusion grows out of the main peak. Afterwards, the diffusive spreading of the main peak does not affect the leading edge anymore. At this stage, $\lambda(t)$ keeps increasing for some time, since the flipping of larger protrusions is more likely to generate a peak with a mass sufficient to revert the whole flock. In addition, $\lambda(t)$ also increases after t_{prot} because of the slight dispersal in flock shapes shown in Fig. 2.9: as the time since the last reversal increases, so does the fraction of flocks with a liquid protrusion. For $t > t_{\text{prot}}$, the $\tau/\log L$ scaling stops since the leading edge converges to a well-defined steady profile. The time t_{prot} can then be estimated as the time it takes for the front to reach the slope corresponding to the liquid protrusion, so that $t_{\text{prot}} \propto \log L$.

We thus expect two different scaling regimes: an initial Gaussian spreading leading to $\lambda(t/\log L)$ and a late-time scaling form $\lambda(t - \alpha \log L)$, once the protrusion has grown out of the main peak. As shown in Fig. 2.13c-d, the protrusion grows out quite early so that the first regime is never observed in our simulations: most reversals take place after the protrusion has grown out. This explains why the $\lambda(t - \alpha \log L)$ and $P(\tau - \alpha \log L)$ scalings work satisfactorily.

2.3.3 Absence of symmetry breaking

Even though the average time between two reversals diverges with system size, so does the time needed for a flock to reverse. In other words, no true symmetry-breaking arises: the system spends finite fractions of time going to the right, to the left, and in the reversals [Solon & Tailleur 2013]. Indeed, starting from a localized flock, the ordered region spreads at constant speed, that of the protrusion. The mean flock size before a reversal L_f is thus proportional to the mean time between reversals. Since a reversal corresponds to the ballistic progression of a fluctuation from the front to the rear of a flock, progressively flipping all its sites, the average duration of a reversal is proportional to L_f and hence to the mean time between reversals. Therefore, when $L \to +\infty$, there is a nonzero probability to find the system in a reversal, $P(|\tilde{m}|)$ does not vanish between $\pm\tilde{m}_0$ and $\tilde{m} = 0$ (Fig. 2.14): there is no spontaneous symmetry breaking.

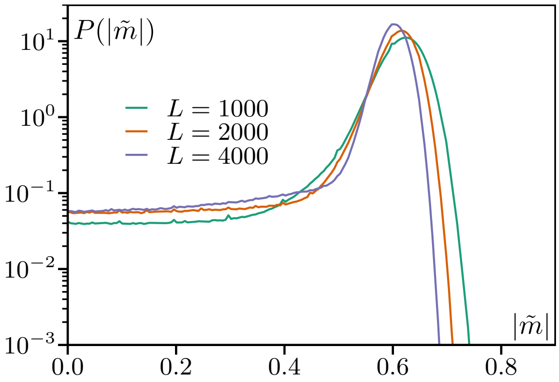

Figure 2.14: $P(|\tilde{m}|)$ showing that $P(|\tilde{m}| = 0)$ converges to a non-vanishing value as L increases. Parameters: $\rho_0 = 4$, $\beta = 1.8$, $D = 1$, $\varepsilon = 1$.

2.3.4 Role of the parameters D, ε and β

Most results presented so far were obtained at fixed, rather typical, parameter values. We now report on the effect of changing the three parameters D, ε and β. Figure 2.15 shows how $\langle\tau\rangle$ and λ, the reversal rate extracted from the exponential tail of $P(\tau)$, vary with each of these parameters, keeping the other two constant.

Comparing $\langle\tau\rangle$ with λ^{-1} (which is the mean of a normalized exponential distribution with rate λ), we see that λ^{-1} 'underestimates' $\langle\tau\rangle$ but that both quantities essentially vary in the same manner. (Their difference is due to the transient regime before $\lambda(t)$ reaches its asymptotic value, as shown in Fig. 2.13a-b.) To account for the variations of $\langle\tau\rangle$, we can thus focus on the reversals at late times, which take place after the protrusion has developed at the front of the flocks.

We find that the divergences of $\langle\tau\rangle$ visible on Fig. 2.15 can be explained by two different mechanisms. First, decreasing D or ε or increasing β while keeping the other parameters fixed brings the system from the flocking phase to the aster phase (see the phase diagrams in Fig. 2.5). Close to the transition, transient asters appear at the beginning of an attempted reversal, as shown in Fig. 2.16e. Once the aster is formed, the propagation of the fluctuation stops until the aster dissolves. (See section Sec. 2.4 for a detailed discussion on aster dynamics.) In the mean time, a large amount of particles arrive from the flock, which tends to destroy the aster and resume the forward motion of the flock. This process thus

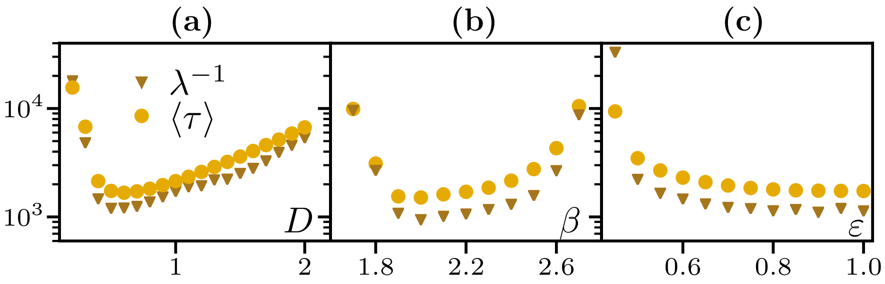

Figure 2.15: Mean reversal time $\langle\tau\rangle$ as a function of D for $\beta = 1.8$ and $\varepsilon = 0.8$ **(a)**, of β with $D = 0.5$ and $\varepsilon = 0.8$ **(b)**, and of ε with $\beta = 2$ and $D = 0.5$ **(c)**. The data are compared with the characteristic time λ^{-1} that corresponds to a purely exponential distribution $P_{\text{exp}}(\tau) = \lambda e^{-\lambda\tau}$, with λ measured from the tail of the true distribution $P(\tau)$. Parameters: $\rho_0 = 3$, $L = 1000$.

tends to suppress reversals: transient asters protect the flock against fluctuations, hence increasing their lifetime.

The other divergences of $\langle\tau\rangle$, in the large D and small β limits, can be accounted for by comparing the roles of diffusion and alignment during a reversal. Aligning interactions tend to flip particles from the flock, hence strengthening the fluctuation. On the contrary, diffusion damps the fluctuation as it propagates. Diffusion dominates when D/e^{β} —the ratio of hopping to alignment rates— increases, i.e. when D increases or β decreases. Figure 2.15 shows a steeper divergence when varying β compared to varying D, as expected from this reasoning.

To support these two scenarios, we now evaluate how likely a fluctuation is to reverse a flock in an idealized situation. We consider the deterministic mean-field evolution of an initial fluctuation of tunable size that encounters an ordered phase mimicking the protrusion of a flock at density ρ_ℓ and magnetization m_ℓ such that $m_\ell/\rho_\ell = \tanh(\beta m_\ell/\rho_\ell)$ (its mean-field value).

The initial condition is depicted in Fig. 2.16a and the evolution is that of Eqs. (2.3)-(2.4) after one takes a mean-field approximation for the nonlinear terms. We choose $\rho_\ell = 1$ without loss of generality, thus fixing the unit of density, and take the initial fluctuation to be fully ordered with magnetization $-\delta m$ and density δm, propagating to the left. We observe that there is a value δm^* such that

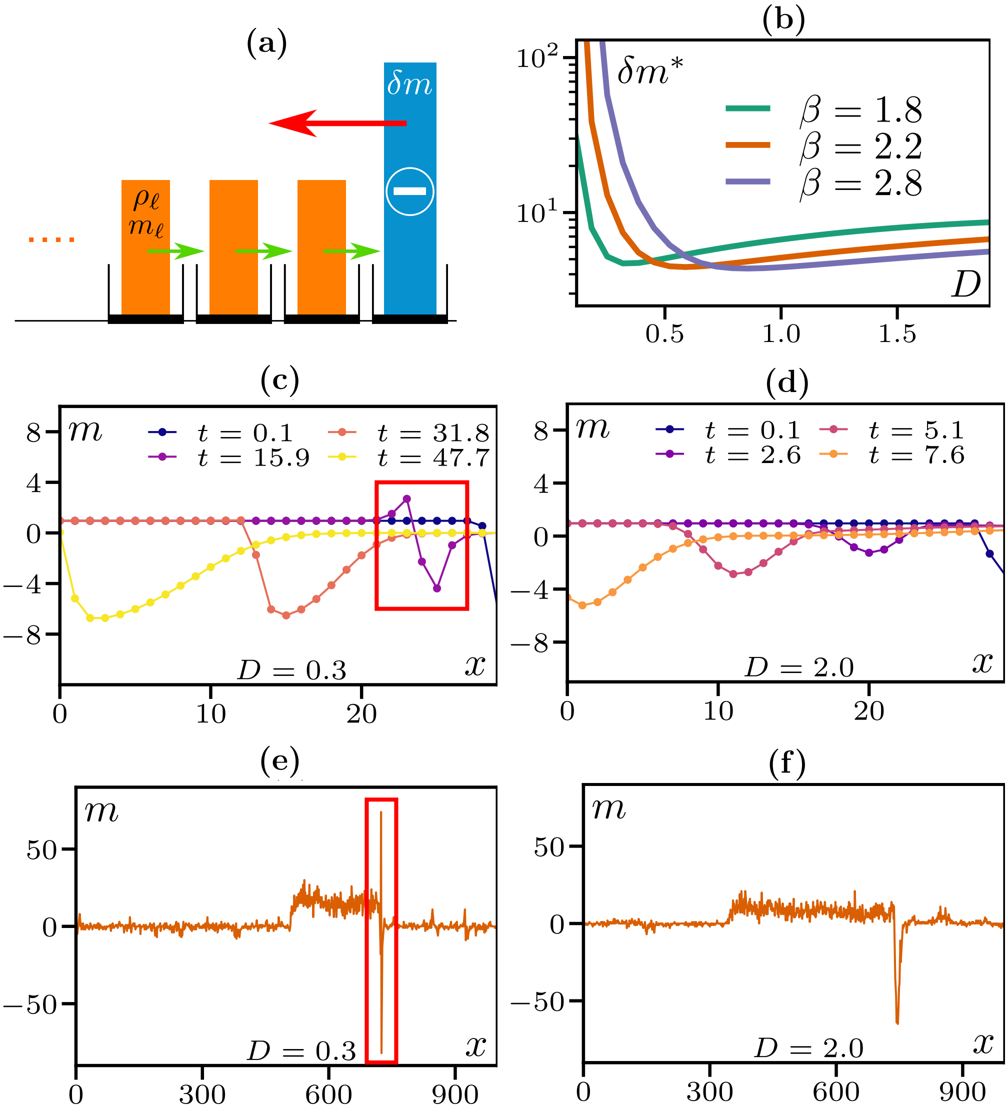

Figure 2.16: **(a):** Sketch of the initial condition in the reduced mean-field model. **(b):** Minimal fluctuation δm^* necessary to reverse the flock in the reduced model. **(c,d):** Evolution of the density profile in the reduced model at low $D = 0.3$ (c) and high $D = 2.0$ (d) for fluctuations $\delta m = 8$ (c) and $\delta m = 6$ (d), slightly bigger than δm^*. Other parameters: $\varepsilon = 1$ and $\beta = 2$. **(e,f)** Instantaneous profiles in the microscopic model at the beginning of a reversal at low $D = 0.3$ (e) and high $D = 2$ (f). The transient aster (red boxes) observed at low D in the reduced model also appears in the full AIM. $\rho_0 = 5$, $L = 1000$, $\varepsilon = 1$ and $\beta = 2$.

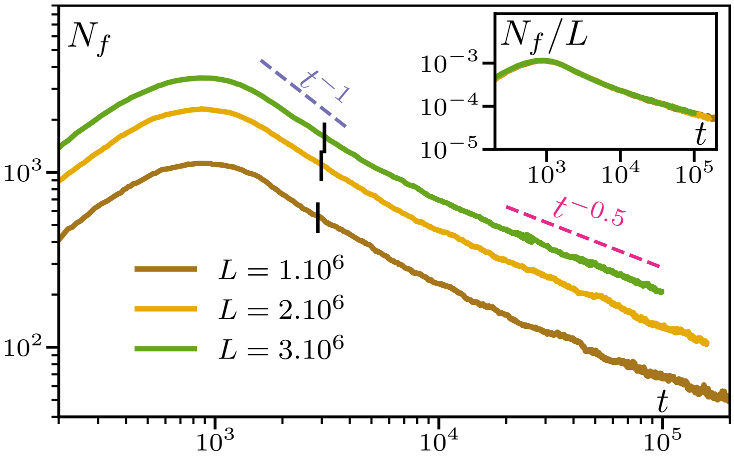

Figure 2.17: Number of flocks N_f as a function of time, starting from a homogeneous disordered initial conditions. The short vertical black lines indicate the crossover time t_c as given in Eq. (2.15). $\rho_0 = 10$, $\beta = 2$, $D = 0.5$, $\varepsilon = 1$.

small fluctuations $\delta m < \delta m^*$ do not propagate and the system remains ordered, whereas large fluctuations $\delta m > \delta m^*$ propagate and flip the entire initial flock [1]. This critical fluctuation size varies with the parameters, as shown in Fig. 2.16b where we vary D for several values of β. At small D we see the transient asters observed in the microscopic model whereas they are not observed for larger D (see Fig. 2.16c-d). The variations of δm^* are consistent with the variations of $\langle \tau \rangle$ in the microscopic model as we see a sharp increase at small D corresponding to the appearance of transient asters and a slower increase at high D with no asters. This minimal model of reversals, despite its simplicity, thus reproduces the basic features of the mean reversal time and supports the two scenarios outlined above for the divergences of $\langle \tau \rangle$.

2.3.5 Coarsening

So far we only considered the steady-state regime where the system contains a single flock. We now study the coarsening dynamics that bring the system from a disordered initial condition to such a steady state. As shown on the space-time diagram of Fig. 2.6e, many small flocks form at early times and merge when they

---

[1] In practice we choose as a criterion that the fluctuation has propagated if the magnetization at a distance $L = 30$ sites from the initial fluctuation has changed sign.

encounter until only one remains. The evolution of the number of flocks N_f can be written as

$$\dot{N}_f(t) = -\frac{N_f(t)}{t_{\text{coll}}(t)} \tag{2.13}$$

with a function $t_{\text{coll}}(t)$ that may depend on N_f and which we can interpret as the mean time before a flock collides with a neighboring one.

We can anticipate two regimes for this collision time. At early times, when flocks are close to one another, they typically encounter a neighbouring flock before reversing their direction. The collision time will then be the ballistic time $t^B_{\text{coll}} = \ell/v$ with $\ell = L/N_f$ the mean distance between flocks. At later times, flocks are further apart and thus reverse their direction of motion before colliding. The collision time then has a diffusive scaling $t^D_{\text{coll}} = \ell^2/(2D_{\text{eff}})$ with the effective diffusion coefficient $D_{\text{eff}} = v^2\langle\tau\rangle$. The crossover between these two regimes is expected at a time t_c such that $t^B_{\text{coll}}(t_c) = \langle\tau\rangle$. Solving Eq. (2.13) in the ballistic regime gives

$$N_f(t) = \frac{L}{\frac{L}{N_f(0)} + vt} \tag{2.14}$$

from which we deduce that the crossover time is

$$t_c = \langle\tau\rangle - \frac{L}{vN_f(0)}. \tag{2.15}$$

Neglecting the dependence of $\langle\tau\rangle$ on $\log L$, which would give subdominant corrections, the number of flocks in the diffusive regime then follows $\dot{N}_f \propto -N_f^3$ and thus $N_f(t) \sim 1/\sqrt{t}$.

Comparing with simulations in Fig. 2.17, we see that the late-time coarsening is indeed clearly diffusive. At short time, we first see an increase in the number of flocks corresponding to the time that they form and grow large enough to be detected by our algorithm (we use a system of two thresholds at $\rho = 2$ and $\rho = 8$ with spatial smoothing on the length $\delta x = 50$ to detect the flocks robustly). The crossover time t_c is then computed from Eq. (2.15), taking the initial time to be the time with the maximum number of flocks, and we indicate t_c by black lines in Fig. 2.17. Consistently with the analysis above, we do see a faster-than-diffusive coarsening in the short window before t_c.

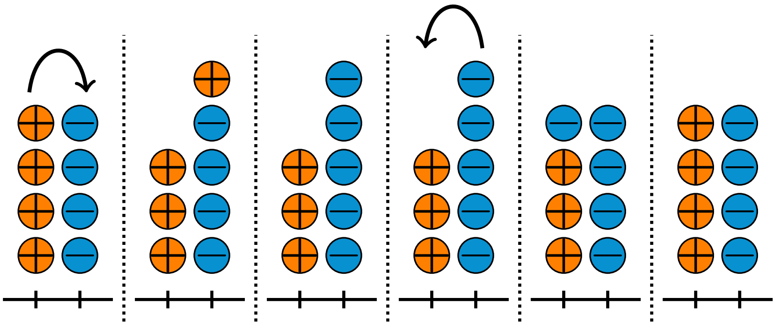

Figure 2.18: A typical sequence of configurations that make asters stable at low temperature.

2.4 Asters

At low temperature or small velocity, a phase develops in which static structures coexist with a dilute gas. (See the phase diagrams in Fig. 2.5 and the snapshot in Fig. 2.6b.) Each of these 'asters' consists in two peaks of right and left-moving particles which apparently 'block' each other. Remember, however, that there is no exclusion in our model so that the underlying mechanism is necessarily more complex and calls for an explanation. We termed these structures asters, by analogy to the star-shaped defects observed in 2d active systems [Kruse *et al.* 2004, Farrell *et al.* 2012].

A closer look at the microscopic dynamics of an aster reveals that its stability arises from periodic orbits in configuration space, as illustrated in Fig. 2.18. Starting from two peaks of opposite magnetization, one particle—say with positive spin—hops forward and lands onto the second site where it belongs to the minority phase. It then flips and aligns with its new environment. The most likely move is then that one of the minus particles hops forward onto the site populated by plus particles. Once again, this particle belongs to the minority phase and flips, leading the system back into its original state. At low temperatures, such trajectories are much more likely than trajectories leading to the evaporation of the aster. To quantify the stability of asters, we first consider in Sec. 2.4.1 a zero-temperature fully-asymmetric model in which the lifetime of an aster can be computed exactly. We then discuss the stability of asters at finite temperature and the corresponding coarsening dynamics in Sec. 2.4.2. Finally, we show in

Sec. 2.4.3 that, for $0 < \varepsilon < 1$, asters typically have a richer shape than suggested by Fig. 2.18: they are not perfectly localized and admit an exponential tail with a characteristic size. Using a mean-field approximation, we compute the corresponding decay length and determine a necessary condition for the existence of asters that captures qualitatively, albeit not quantitatively, the phase boundary between flocks and asters shown in Fig 2.5.

2.4.1 Lifetime of an aster at zero temperature

To make progress analytically, we first consider a $T = 0$, fully asymmetric version of the AIM. Particles hop at rate $v = 2D$ and the aligning interaction is resolved instantaneously, due to the $\beta \to \infty$ limit of the flipping rate (2.1). In practice, when a particle hops onto a new site with two particles or more, it immediately acquires the magnetization of the target site. The limit is ill defined when one has both $m_i = 0$ and $\beta = \infty$. For simplicity, we here assume that when a particle of spin s arrives on a site occupied by a particle of spin $-s$, it flips and acquires a $-s$ spin, so that the situation $m_i = 0$ does not occur. As a result, the sole microscopic time-scale of the system is v^{-1}. The case in which both particles keep their current spins and flip at rate ω_0 is qualitatively similar, albeit more involved due to the presence of the second time scale ω_0^{-1}.

Consider an initial condition in which N particles are randomly placed on the lattice and each site is given a magnetization at random. The dynamics is such that all sites remain fully ordered at all times, with $m_i = \pm\rho_i$, and the total escape rate is always Nv. A typical trajectory is shown in Fig. 2.19. It rapidly leads to the emergence of an extensive number of asters, whose rare and sudden evaporations lead to a coarsening dynamics. To characterize the latter, we compute the lifetime of an aster comprising M particles (spread out over the two sites).

Let us consider the situation depicted in Fig. 2.20 in which an aster is formed with n particles with $+1$ spins at site i and $M - n$ particles with -1 spins at site $i + 1$. We denote this configuration as $\mathbf{n} \equiv (n, M - n)$. The system evolves at rate $q_n = vn$ towards the configuration $\mathbf{n} - \mathbf{1}$ and $p_n = v(M - n)$ towards $\mathbf{n} + \mathbf{1}$. We denote by $r_n = p_n + q_n$ the escape rate from configuration $\mathbf{n}$, which is here given by $r_n = vM$. Given the expressions of q_n and p_n, there is a linear drift that takes the system towards the most likely configuration $\mathbf{n} = \mathbf{M}/2$. Note that the

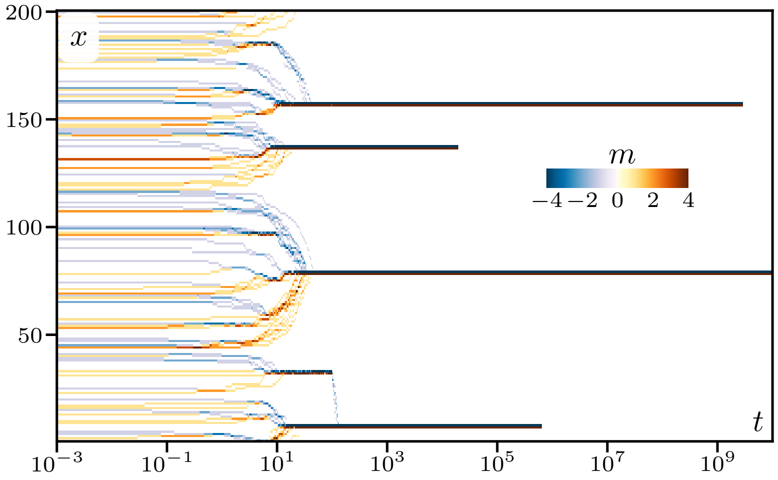

Figure 2.19: Starting from a random configuration at $t = 0$ in the zero-temperature model, the system rapidly evolves into a large number of small asters. These coarsen on much longer time scales, as smaller condensates evaporate and are redistributed into larger ones. Parameters: $L = 200$, $N = 100$, $v = 1$, $\varepsilon = 1$.

configurations $\mathbf{M}$ and $\mathbf{0}$ are limiting cases that correspond to the evaporation of the aster. To get an intuitive understanding of the aster dynamics, we consider the master equation of this process:

$$\partial_t P(n) = q_{n+1}P(n+1) + p_{n-1}P(n-1) - (q_n + p_n)P(n) \ . \tag{2.16}$$

Small Gaussian fluctuations close to the most likely configuration $\mathbf{n} = \mathbf{M}/2$ are well described by introducing $P(x = n/M) = MP(n)$ and expanding (2.16) to first order in $dx = M^{-1}$. Doing so yields the Fokker-Planck equation

$$\partial_t P(x) = \frac{\partial}{\partial x}\left[V'(x)P(x) + \frac{v}{2M}\frac{\partial}{\partial x}P(x)\right] \ , \tag{2.17}$$

which corresponds to the dynamics of a Brownian particle in a harmonic potential $V(x) = v(x - \frac{1}{2})^2$ at temperature $\frac{v}{2M}$, as illustrated on Fig. 2.20. The mean-first passage time τ until the evaporation of an aster with M particles can then be estimated using the Arrhenius scaling $\log\tau \propto M/2$. This scaling is not expected to hold quantitatively, since the diffusive approximation (2.16) is expected to fail in the large-deviation regime where $x \gg \frac{1}{\sqrt{M}}$, but it captures the physics that makes the aster long-lived at zero temperature.

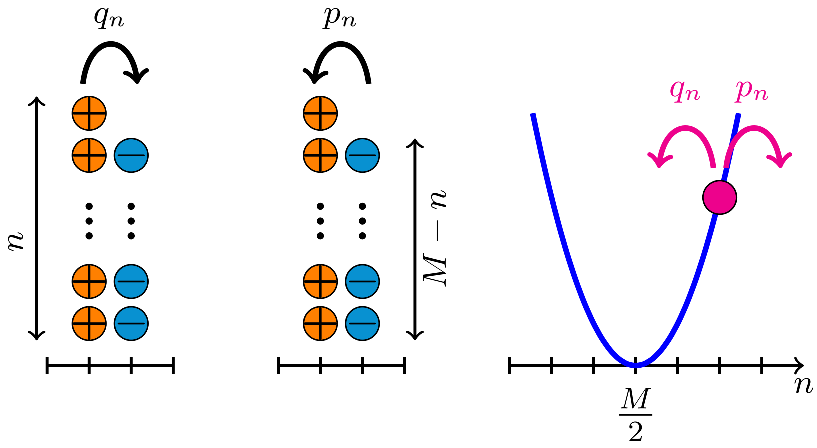

Figure 2.20: **Left:** A particle hops out of a site with n particles at a rate $q_n = nv$. This takes the aster from $(n, M-n)$ to $(n-1, M-n+1)$. **Center:** A particle hops out of a site with $M-n$ particles at a rate $p_n = (M-n)v$. This takes the aster from $(n, M-n)$ to $(n+1, M-n-1)$. **Right:** This dynamics is equivalent to the Brownian dynamics of a single particle at position n, confined in a harmonic potential $V(n) = \frac{v}{2}(\frac{n}{M} - \frac{1}{2})^2$, with $n = 0$ and $n = M$ being absorbing boundaries corresponding to the evaporation of the aster.

We now wish to compute exactly the mean-first passage time to reach either $\mathbf{M}$ or $\mathbf{0}$, which will trigger the redistribution of the aster particles into a neighboring aster, hence driving the coarsening process. Let us note T_n the average evaporation time, starting from configuration $\mathbf{n}$. In an average time r_n^{-1}, the system jumps to $\mathbf{n}-1$ or $\mathbf{n}+1$ with probabilities q_n/r_n and p_n/r_n, respectively. One thus has the recursive relation:

$$T_n = \frac{1}{r_n} + \frac{p_n}{r_n} T_{n+1} + \frac{q_n}{r_n} T_{n-1} \tag{2.18}$$

that has to be solved with the boundary conditions

$$T_0 = T_M = 0 \; . \tag{2.19}$$

To do so, we follow standard methods [Van Kampen 1992, Antal & Scheuring 2006] and introduce $U_n = T_{n-1} - T_n$. Equation (2.18) can then be rewritten as

$$p_n U_{n+1} = q_n U_n + 1 \; . \tag{2.20}$$

Introducing $\pi_0 = 1$ and, for $i \geq 0$,

$$\pi_i \equiv \prod_{k=1}^{i} \frac{q_k}{p_k} \quad \text{and, further,} \quad \sigma_i = \sum_{k=1}^{i} \frac{1}{p_k \pi_k} \ , \tag{2.21}$$

Eq. (2.20) is readily solved as

$$U_{n+1} = \pi_n U_1 + \pi_n \sigma_n \ . \tag{2.22}$$

Using $T_0 = 0$, we first get $T_1 = -U_1$. The definition of U_n then recursively leads to

$$T_{n\geq 2} = -U_1 \sum_{i=0}^{n-1} \pi_i - \sum_{i=1}^{n-1} [\pi_i \sigma_i] \ . \tag{2.23}$$

Finally, U_1 is determined by imposing the boundary condition $T_M = 0$, which gives:

$$U_1 = -\frac{\sum_{i=1}^{M-1} [\pi_i \sigma_i]}{\sum_{i=0}^{M-1} \pi_i} \ . \tag{2.24}$$

All in all, the mean time to evaporation starting from the configuration $\mathbf{n}$ is given by

$$T_n = \frac{\sum_{i=0}^{n-1} \pi_i}{\sum_{i=0}^{M-1} \pi_i} \sum_{i=1}^{M-1} [\pi_i \sigma_i] - \sum_{i=1}^{n-1} [\pi_i \sigma_i] \tag{2.25}$$

where the second sum vanishes for $n = 1$. The above results are valid for generic random walks with non-vanishing rates p_n and q_n. In the case at hand, using $p_n = v(M-n)$ and $q_n = vn$, we find

$$\pi_i = \binom{M-1}{i}^{-1} \ , \tag{2.26}$$

which allows the computation of T_n.

The mean first passage times to evaporation starting from all possible configurations are plotted in Fig. 2.21a, for M up to 14. Interestingly, T_n becomes rapidly independent of n. This can be understood as follows: due to the asymmetry between p_n and q_n, the most likely path to evaporation is to fall from n to $M/2$ and then to get absorbed. Furthermore, Fig. 2.21a suggests an exponential increase of T_n with M. To compute the leading order of T_n, consider the various terms

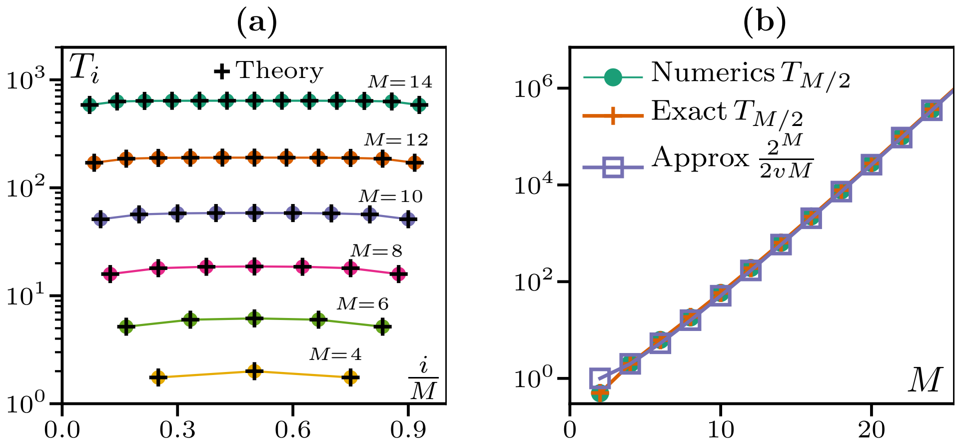

Figure 2.21: **(a):** Mean-first-passage times from site i to sites 0 or M, as M varies from 4 to 14. The circles correspond to numerical simulations whereas the crosses correspond to Eq. (2.25). **(b):** Mean-first passage times to evaporation for an aster with M particles. Green disks are results of numerical simulations, averaged over 10^4 realizations. Orange crosses correspond to the exact formula (2.25), and purple squares to approximation (2.31).

of Eq. (2.25) and their scaling as $M \to \infty$. We first note, using Eq. (2.26), that $\pi_0 = \pi_{M-1} = 1$, $\pi_1 = \pi_{M-2} = (M-1)^{-1}$, and $\pi_{1<i<M-2} = \mathcal{O}(M^{-1})$. Consequently, $\pi_1 + \pi_2 + \cdots + \pi_{n-1} \to 0$ for n<M and only π_0 and π_{M-1} contribute to the sums. Noting also that $(\pi_k p_k)^{-1}$ simplifies into

$$\frac{1}{\pi_k p_k} = \frac{(M-1)!}{vk!(M-k)!} = \frac{1}{vM}\binom{M}{k}, \tag{2.27}$$

we see that Eq. (2.25) can be approximated as

$$T_n \sim \frac{1}{2vM}\sum_{i=1}^{M-1}\left[\pi_i \sum_{k=1}^{i}\binom{M}{k}\right] - \frac{1}{vM}\sum_{i=1}^{n-1}\left[\pi_i \sum_{k=1}^{i}\binom{M}{k}\right]. \tag{2.28}$$

Finally, we note that, for $n < M-1$,

$$\sum_{i=1}^{n}\left[\pi_i \sum_{k=1}^{i}\binom{M}{k}\right] < \left[\sum_{i=1}^{n}\pi_i\right]\left[\sum_{k=1}^{M-2}\binom{M}{k}\right] \tag{2.29}$$

$$= o\left(\sum_{k=1}^{M-1}\binom{M}{k}\right), \tag{2.30}$$

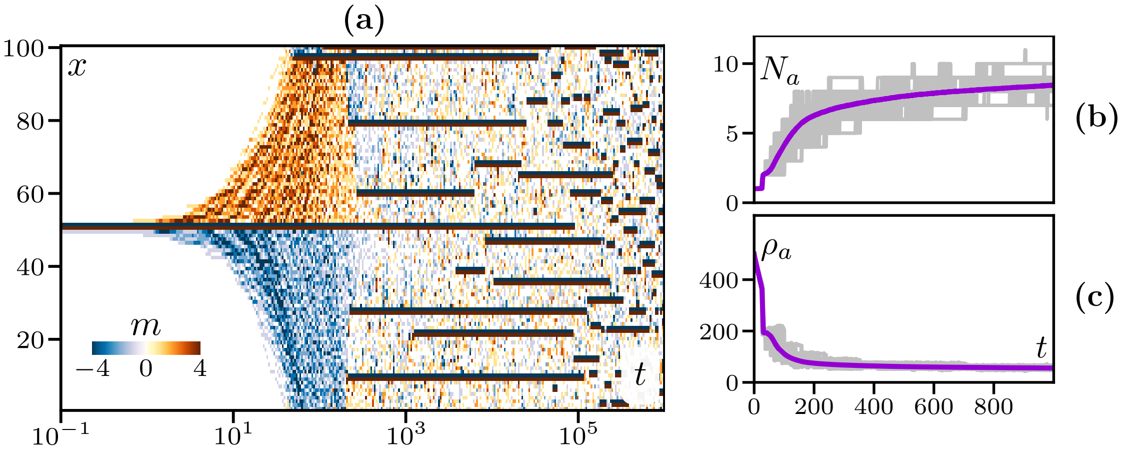

Figure 2.22: **(a)** Spatiotemporal plot of the relaxation dynamics from a single aster to the fluctuating aster phase of the AIM with rates (2.1). **(b-c):** Relaxation dynamics in the aster phase for the AIM with rates (2.1). Number of asters as a function of time, averaged over 1000 simulations (magenta) **(b)** and average density contained in one aster **(c)**. Fifty representative trajectories appear in gray. Parameters: $T = 0.2$, $\varepsilon = 1$, $L = 100$, $\rho_0 = 10$, $D = 0.5$.

so that

$$T_n \sim \frac{1}{2vM}\pi_{M-1}\sum_{k=1}^{M-1}\binom{M}{k} \sim \frac{2^M}{2vM} \tag{2.31}$$

Figure 2.21 (right) shows the comparison between numerical measurements of $T_{M/2}$, its exact expression (2.25) and the asymptotic estimate (2.31), which is remarkably close to the exact values. The stability of asters and their coarsening at zero temperature thus stems from an evaporation rate that vanishes exponentially with their density.

2.4.2 Coarsening at small temperature

At zero temperature, aster coarsening occurs via an extremal dynamics: smallest asters evaporate first and are redistributed among their neighbors. Since the lifetime of an aster diverges exponentially with its height, this leads to an extremely slow dynamics, as apparent from Fig. 2.19.

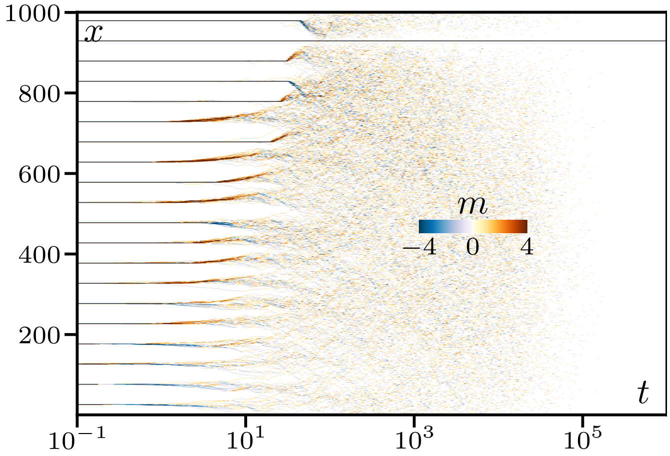

Figure 2.23: Spatiotemporal plot for the AIM with rates (2.34), starting from 20 asters whose initial density increases linearly from 6 to 25 as x increases; coarsening leaves a single macroscopic aster. Parameters: $D = 1$, $L = 1000$, $\omega_0 = 1$, $\beta = 0.375$, $\rho_0 = 0.29$.

At finite temperature, a new phenomenon sets in: when a particle hops forward, as in the second configuration of Fig. 2.18, it now has a finite probability $P_{\rm hop}$ of hopping further forward and leaving the aster before flipping its spin, with

$$P_{\rm hop} = \frac{p}{p + W(s \to -s)} \ . \tag{2.32}$$

In an aster comprising two sites with ρ particles, this leads to a flux of particle $j_{\rm leak}(\rho)$ leaving the aster, where

$$j_{\rm leak}(\rho) \propto p\rho P_{\rm hop} = \frac{p^2}{p + W(s \to -s)}\rho \ . \tag{2.33}$$

The variations of $j_{\rm leak}(\rho)$ with ρ then determine the late-stage dynamics. For the flipping rates (2.1), $j_{\rm leak}(\rho) \propto \rho$ at large densities since the hopping rate is bounded, $W(s \to -s) < \exp(\beta)$: large asters leak particles faster than smaller ones, which arrests the coarsening and leads to a steady-state with an extended number of finite-size asters, as illustrated in Fig. 2.22a and Fig. 2.22b-c. (It would be interesting to generalize approaches developed in the past to predict the size of competing finite condensates [Thompson *et al.* 2010] but this is beyond the scope of this study.) For the unbounded rates studied in [Kourbane-Houssene *et al.* 2018]:

$$W(s \to -s) = \omega_0 e^{-\beta s m_i}, \tag{2.34}$$

larger asters leak slower, leading to a single macroscopic aster, as illustrated in Fig. (2.23). Finally, in a related $1d$ flocking model, a coarsening into a single structure reminiscent of an aster was observed in the presence of "centering" interactions, which bias the motion of particles towards dense regions [Raymond & Evans 2006]. The generality of the mechanisms leading to aster-like structures and their stability is thus an interesting question beyond the sole case of the AIM.

2.4.3 Shape of asters

Let us now consider the case $\varepsilon < 1$, where hopping is not fully asymmetric. Thanks to diffusion, particles can hop backward and asters are then spread over several sites. Since they typically comprise many particles, we expect to be able to describe their shape using the mean-field equations (2.5,2.6) introduced in Sec. 2.3.1. It is straightforward to check that these equations admit stationary solutions of the form

$$\rho(x) = k e^{-\mu_c x}; \quad m(x) = k\phi e^{-\mu_c x} \tag{2.35}$$

with k a normalization constant and ϕ and μ_c (the subscript "c" stands for "continuous" for a reason that will become apparent shortly) solutions of

$$\frac{v^2}{2D}\phi(\phi^2 - 1) = \phi\cosh(\beta\phi) - \sinh(\beta\phi) \tag{2.36}$$

$$\mu_c = -v\phi/D. \tag{2.37}$$

Furthermore, these are the only stationary solutions of Eqs. (2.5,2.6) such that $\rho(x)$ and $m(x)$ are proportional to each other. Note that Eq. (2.35) does not describe the full aster but only half of it, for $x > 0$ or $x < 0$. We are not aware of any analytic solution describing the full aster, including its singularity at $x = 0$. Finally, the competition between the asymmetric hops leading particles towards the aster and the diffusive dynamics allowing them to explore neighboring sites is reminiscent of the diffusive motion of colloids under gravity. The solutions (2.35) can thus be seen as two exponential atmospheres pointing towards the core of the aster.

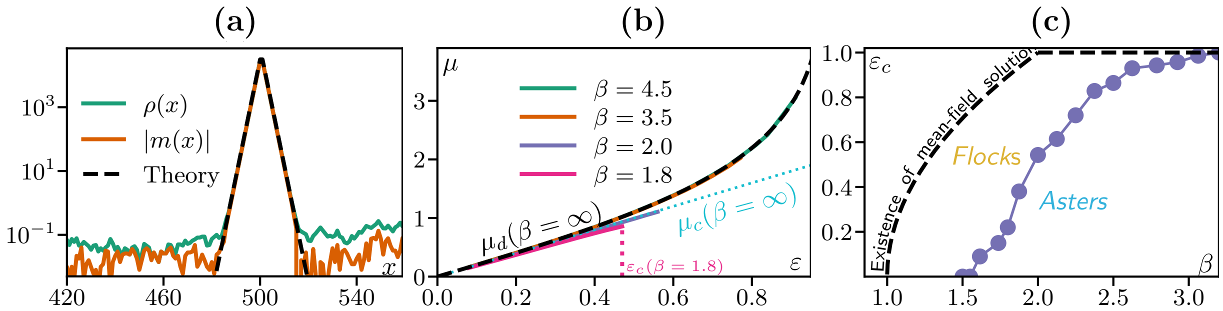

Figure 2.24: **(a):** Profile of an aster in the microscopic model. The dashed lines are the exponential decays predicted by Eqs. (2.39)-(2.40). $L = 1000$, $\rho_0 = 100$, $\beta = 4$, $\varepsilon = 0.5$, $D = 0.5$. **(b):** Measured values of μ in the microscopic model at different β compared with the predictions from the continuous mean-field equations (blue dotted line) and from the discrete ones (black dashed line). $L = 1000$, $\rho_0 = 100$, $D = 0.5$. **(c):** Phase boundary $\varepsilon_c(\beta)$ such that asters are observed for $\varepsilon < \varepsilon_c$ in microscopic simulations (symbols), compared to the limit of existence of aster solutions in the mean-field equations (dashed line). $L = 500$, $\rho_0 = 10$, $D = 0.5$.

We now compare these solutions with the aster profiles measured in the microscopic model in Fig. 2.24a. The profiles of density and magnetization indeed exhibit an exponential decay on both sides of the aster. In Fig. 2.24b, we see that the measured decay exponent μ agrees well with the solution μ_c of Eq. (2.37) at small ε but deviates for larger ε. Note that we plot only the curve $\mu_c(\beta = \infty)$ in Fig. 2.24b since the curves for different values of β would be indistinguishable on the scale of the figure. Setting $\beta = \infty$ also simplifies the calculation since it amounts to fixing $\phi = \pm 1$ in Eq. (2.36) so that $\mu_c(\beta = \infty) = \pm v/D = \pm 2\varepsilon$.

Increasing ε, we see that the discrepancy between μ_c and the measured μ increases. This deviation can be attributed to the continuous limit used to derive Eqs. (2.5,2.6). If instead we retain the full discrete equations Eqs. (2.3,2.4) in the mean-field approximation, and look in the same way for exponential solutions

$$\rho_i = k\kappa^i; \quad m_i = k\phi\kappa^i, \tag{2.38}$$

we find the conditions

$$\frac{4D(\kappa-1)^2\phi - v(\kappa^2-1)}{4\kappa} = \phi\cosh[\beta\phi] - \sinh[\beta\phi] \tag{2.39}$$

$$(\kappa + \frac{1}{\kappa} - 2) = \frac{v\phi}{2D}(\kappa - \frac{1}{\kappa}); \quad \mu_d = -\log\kappa \tag{2.40}$$

The decay exponent μ_d (where "d" stands for "discrete") predicted by Eqs. (2.39,2.40) is now in near-perfect agreement with microscopic simulations as shown in Fig. 2.24b.

Interestingly, we find that there is a maximum value of ε that we denote ε_c above which no physical exponential solution is found (we require that $\phi \in [-1, 1]$ and that μ_d be of opposite sign to ϕ for a physical solution). In Fig. 2.24c, we compare this limit value with the transition line between the flock and aster phases in the microscopic model. Both lines show the same trend as a function of β but are quantitatively different. This indicates that, unsurprisingly, exponential solutions can exist at the mean-field level while asters are not observed because either the full aster solutions do not exist at the mean-field level or because they are unstable to fluctuations.

2.5 Robustness of the results

2.5.1 Comparison with the model of O'Loan and Evans

We now compare our results on reversals to those obtain by O'Loan and Evans in [O'Loan & Evans 1999]. Contrary to our observations in Fig. 2.9, these authors did not report the growth of a protrusion. Consequently, they explain that $\langle\tau\rangle \propto \log L$ (See Fig. 2.25a) through a somewhat different argument compared to Sec. 2.3.2: Observing that the flock has the shape of a Poisson distribution $\rho(x,t) \propto e^{-t}t^x/x!$ in the zero-noise limit, they estimate the reversal time as the time where the leading edge is sufficiently spread that reversing one particle at the front is sufficient to flip the whole aggregate. This indeed predicts a logarithmic dependence but the presence of the exponential tail in $P(\tau)$ (that they also observe) does not fit easily in this picture.

To check if there are indeed qualitative differences between the flock shapes in the two models, we simulated the model of [O'Loan & Evans 1999]. Fig. 2.25b

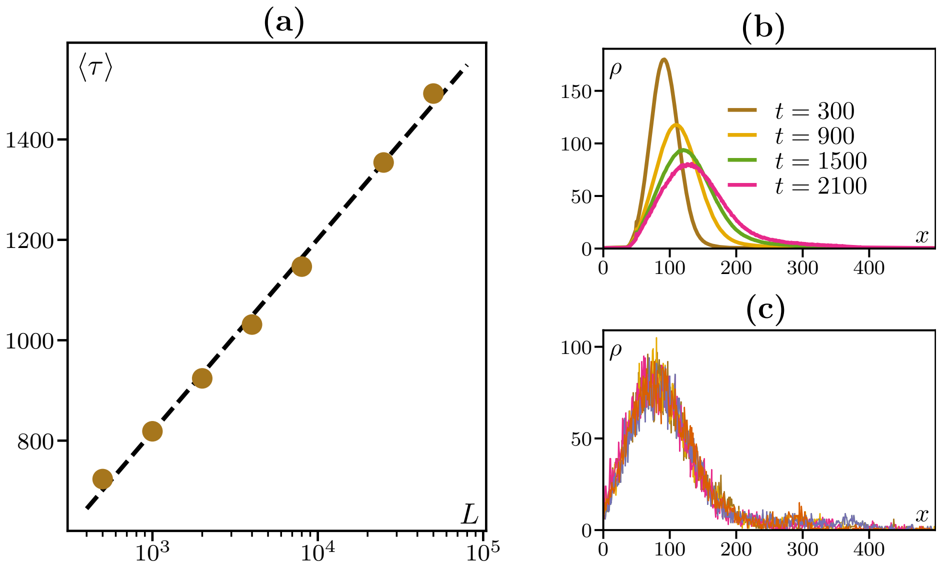

Figure 2.25: **(a) :** Mean time between reversals in the model of O'Loan and Evans. Evolution of the averaged density profile as a function of time **(b)** and instantaneous density profiles at a late time $t = 3600$ **(c)** in the model of O'Loan and Evans. Parameters: $\rho_0 = 10$, $L = 1000$ (b-c) and $\eta = 0.1$.

shows the average profiles obtained by the same procedure as for the AIM in Fig. 2.9. Contrary to the AIM, the density decays continuously to zero on the fore front and there is no obvious protrusion at a fixed density. However, looking at individual flocks that have survived the longest in Fig. 2.25c, one can observe such protrusions albeit with a rather large dispersion in the leading edge position so that the averaging procedure completely smears it out (See Fig. 2.25b). Nevertheless, the phenomenology seems to be the same as in the AIM, with protrusions appearing later in time so that, for the system sizes we simulated, most reversals take place before the protrusions develop.

This has consequences for the scaling of the reversal time distribution. In Fig. 2.26a-b we show the rate of reversal for several system sizes. In the AIM, changing the system size shifts $\lambda(t)$ so that a collapse is obtained by plotting $\lambda(\tilde{t})$ with $\tilde{t} = t - \alpha \log L$ (see Fig. 2.13), and we interpreted this shift essentially as the time for the protrusion to develop. For the model of O'Loan and Evans, we see in Fig. 2.26a-b that the collapse is obtained upon a *rescaling* $\tilde{t} = t/(\log L)^\gamma$ with $\gamma = 2.2$. This corresponds to the first regime described in Sec. 2.3.2 when

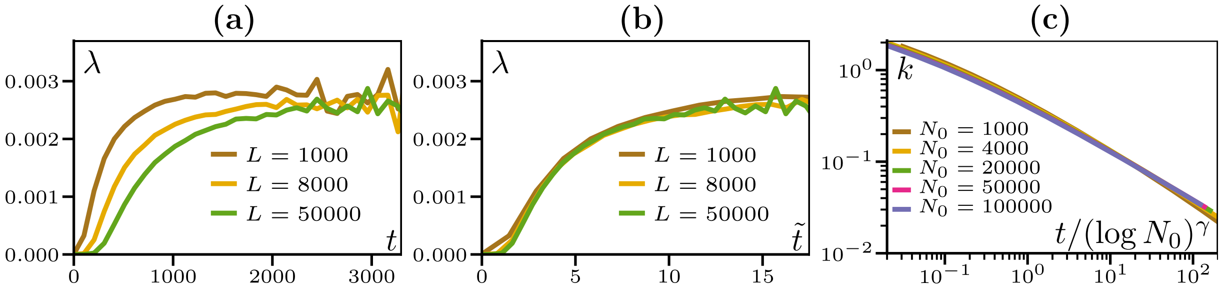

Figure 2.26: Rate of reversal λ as a function of time t since the last reversal **(a)** and of the rescales time $\tilde{t} = t/(\log L)^\gamma$, with $\gamma = 2.2$ **(b)**. Parameters: $\rho_0 = 10$ and $\eta = 0.1$. **(c):** slope $k(t)$ at the front of a Poisson flock as a function of rescaled time $t/(\log L)^\gamma$, with $\gamma = 1.8$ for several values of L.

the steepness of the leading edge is still evolving in time. The steepness can be estimated numerically for a Poissonian $\rho(x,t) \propto e^{-t}t^x/x!$ by looking at the slope $k(t) = -\partial\rho(x,t)/\partial x$ of this distribution at the front of the flock (at $\rho = 1$). We see in Fig. 2.26c that it scales with system size approximately as $k \propto (\log L)^\gamma$ with $\gamma = 1.8$, not too far from the value that rescales the distributions in Fig. 2.26b. The effect of the protrusion is seen only at late times and small enough system size where a plateau in $\lambda(t)$ is reached.

2.5.2 Off-lattice version

To close this chapter, let us address the fate of flocks and asters in the off-lattice counterpart of the 1d AIM. We thus consider N particles moving in continuous space. Each particle carries an Ising spin ±1, which flips at rate:

$$W(s \to -s) = \exp\left(-s\beta\frac{m_i}{\rho_i}\right) \tag{2.41}$$

where the local density ρ_i and magnetization m_i are computed on a segment of size $r = 1$ around each particle. The position evolves according to the Langevin equation:

$$\dot{x} = sv + \sqrt{2D}\eta \tag{2.42}$$

with v the speed, a continuous analogous of $2D\varepsilon$, and η a Gaussian white noise of unit variance. Simulations are carried using a forward Euler algorithm with parallel updates.

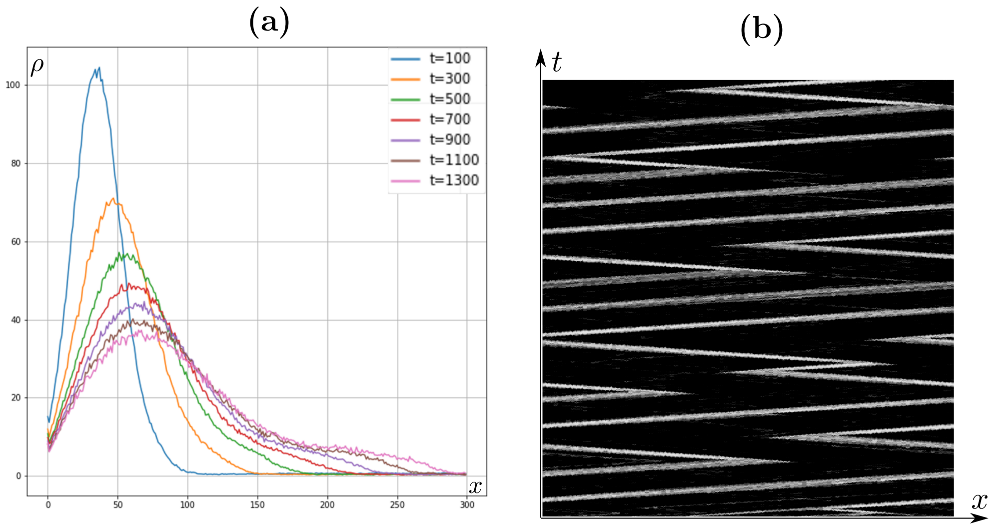

Figure 2.27: **(a)** : Evolution of the density profile averaged over 150 flocks. As in lattice models, we can observe a spreading peak and a protrusion. Parameters: $\rho = 5$, $v = 0.5$, $\beta = 1.7, L = 1000, D = 1$. **(b)** : Space-time diagram in the flocking phase. Lighter grey levels represents higher particle density. Parameters: $\rho_0 = 2$, $v = 1$, $\beta = 2, L = 300$.

The phenomenology of this model is very similar to that of the on-lattice version of the AIM. We do observe flocks presenting a protrusion and reversals (Figure 2.27), which are qualitatively in accordance with the on-lattice model.

However, lowering the temperature, we do not see asters. Preparing the system in a initial aster configuration (Fig. 2.28a) – two peaks with exponential profiles facing each other, as described in Sec. 2.4.3 – we witness one side of the aster taking over the other by reversing its spins (Fig. 2.28b), until a flock remains (Fig. 2.28c). One way to account for this instability is as follows: Starting from an idealized completely symmetric situation, slightly disturbing the magnetization – say by increasing its value on the positive side – will create a zone of positive magnetization on the initially negative side of the aster. On-lattice, due to the discreteness of space, this zone would be contained on a single site and the aligning dynamics would restore the symmetry. Here, the zone of positive magnetization progresses through the negative side of the aster, flipping the particles as it advances, much like what happens during a reversal. The typical sequence of configurations that made asters stable on-lattice does not exist in continuous space and asters are

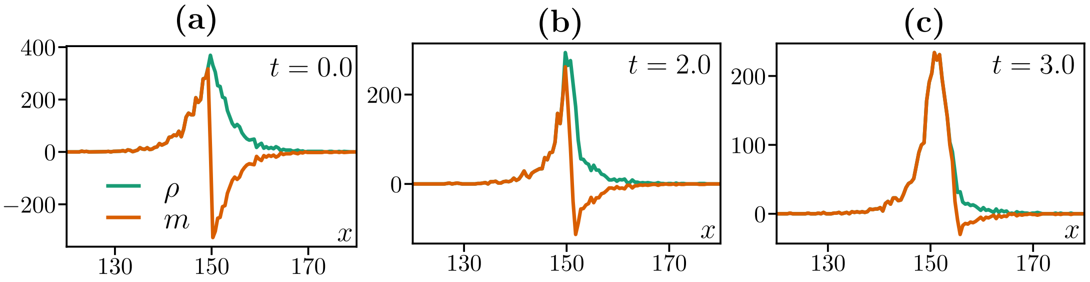

Figure 2.28: Destabilization of an aster in the off-lattice version of the AIM. Parameters : $\rho = 10$, $L = 300$, $v = 1$, $D = 1$, $\beta = 4$.

thus unstable. Note that this instability is also observed if the model is simulated using random sequential updates.

We also examined the stability of asters in the hydrodynamic equations Eqs. (2.5, 2.6). We simulated the equations using a finite difference algorithm, starting from the typical exponential shape of an aster. Consistently with the off-lattice model, we observed a rapid destabilization, hinting that such solutions are not stable at the hydrodynamic level. All these observations point to the fact that asters do not exist off-lattice.

2.6 Conclusion

We have provided a detailed study of the active Ising model in one spatial dimension. Despite its simplicity, the AIM shows two non-trivial phases characterized by flocks and asters. We found the flocking phase to exhibit the same phenomenology as other one-dimensional flocking models [Czirók *et al.* 1999, O'Loan & Evans 1999, Raymond & Evans 2006, Dossetti 2011, Solon & Tailleur 2013, Laighléis *et al.* 2018, Sakaguchi & Ishibashi 2019]: Large ordered aggregates spread while propagating, merge when they collide, and regroup when stochastically reversing their direction of motion. As reported before [O'Loan & Evans 1999, Raymond & Evans 2006, Solon & Tailleur 2013], the time between two reversals of a flock increases logarithmically with system size. We went further and explained this dependence as well as the variations with the velocity of particles and the temperature. In addition, we have also analyzed in detail the flock shapes and how they evolve in time. The global picture that emerges is that of a liquid-gas phase separation which cannot relax to steady state because of reversal events. Since this is expected to be generic for $1d$ flocking models, we also expect our results to be relevant to other systems. We therefore discussed our analysis of the reversal times based on the flock shapes by examining the model of [O'Loan & Evans 1999] and observed qualitative agreement.

We reported a new phase of the AIM populated by "asters" which are composed of two peaks of opposite magnetization facing each other. These asters appear only because of the interplay of alignment and self-propulsion and thus through a mechanism qualitatively different from traffic jams due to steric interactions or from the "dipoles" observed in [Raymond & Evans 2006] which rely on centering interactions that favor motion towards high-density regions. We have provided an exact solution of the zero-temperature dynamics of an aster and showed that they dissolve in a time that is exponential in their size. At infinite time, this leads to a single aster in the zero-temperature limit but to a finite density of asters at small but finite temperature. Finally, we have shown that asters generically exhibit exponential tails with decay exponents that are well predicted by a mean-field theory. Although we find that asters are unstable in continuous space, it would be interesting to see if the simple mechanism which leads to their existence on-lattice could be realized in different contexts, numerically and experimentally.

Common statistical mechanics wisdom states that fluctuations become more important as the dimension of space becomes lower. In equilibrium, this goes as far as preventing the existence of an ordered state in a model with only short-ranged interactions. In our active system, the flocking phase shows that ordering is possible but fluctuations still prevent true symmetry breaking by inducing reversals of the flock direction. Fluctuations play a somewhat different but also essential role in the dynamics of asters: we found that the dissolution of asters and thus their coarsening is due to rare fluctuations, giving rise to extremal dynamics. In contrast, we found that some features of flocks and asters are accounted for to a good accuracy by a mean-field approach that neglects fluctuations.

Chapter 3

Metastability of discrete symmetry flocks

Contents

3.1 Introduction

The stability of the ordered phase of the equilibrium Ising model against nucleation is guaranteed by Peierls' argument in $d > 1$ [Domb & Green 1972, Peierls 1991], which essentially states that surface tension makes any finite droplet of the minority phase shrink. On the other hand, spin waves are well known to prevent the emergence of true long-range order in the two-dimensional ($2d$) equilibrium XY model, as dictated by the Mermin-Wagner theorem [Mermin & Wagner 1966, Kardar 2007]. It was therefore a surprise when the Vicsek model [Vicsek *et al.* 1995], which can be seen as an active version of the XY model, was shown to possess a flocking phase with true long-range polar order, 'escaping' the theorem. This phase was first described by Toner & Tu in [Toner & Tu 1995]. Since long-range order survives spin waves, it seemed reasonable that the ordered phase should also survive stronger excitations. This may be part of the reason why its robustness to large fluctuations has long remained unexplored.

3.1.1 Fragility of the order

Recently, however, numerical results in $2d$ have questioned the stability of the flocking phase. First, it has been shown in [Codina *et al.* 2022] that, for large enough noise, a small obstacle or a group of particles oriented against the flow can break order in the Vicsek model by triggering a counter-propagating front that grows and eventually reverses the global polarity (See Fig.3.1a). This happens in a finite fraction of the phase diagram close to the disordered phase, hence shifting the flocking phase to lower noise values. Second, [Besse *et al.* 2022] studied the stability of the Malthusian flocks introduced in [Toner 2012a] in which particles die and reproduce on a fast scale, smearing out the density field fluctuations around its average value. In the limit case of constant-density, they showed that the flocking phase is metastable to the spontaneous nucleation of aster-shaped defects (See Fig. 3.1b). Nucleation events eventually lead to a constantly evolving active foam made of asters surrounded by a network of shock lines, destroying the ordered phase. These numerical results question the stability of the $2d$ orientationally-ordered phases of active systems. So far this question has not been approached theoretically. Furthermore, higher dimensions remain uncharted territory.

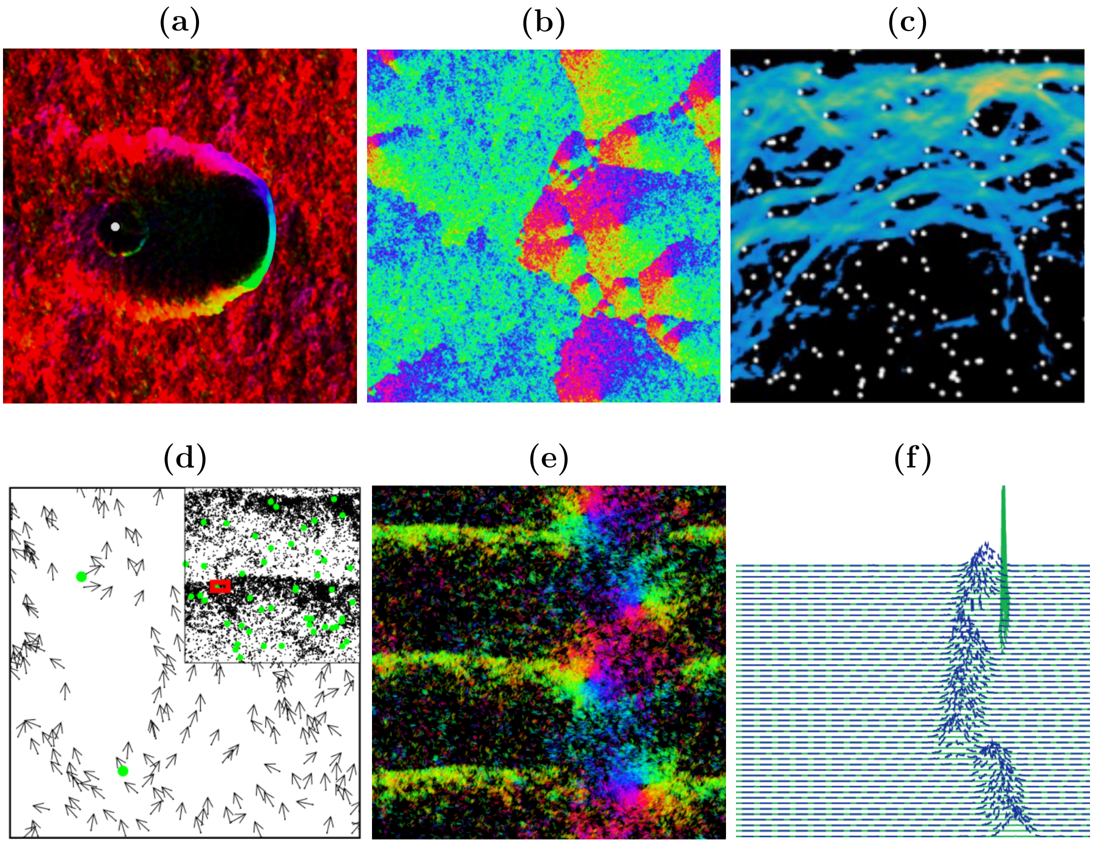

Figure 3.1: In **(a)**, **(b)** and **(e)**, the color indicates the local orientation of the velocity. **(a):** Snapshot of the propagating wave triggered by the presence of an obstacle in the ordered phase of the Vicsek model [Codina *et al.* 2022]. **(b):** Snapshot showing the nucleation of aster-shaped defects in constant-density flocks [Besse *et al.* 2022]. **(c):** Magnitude of the current for a flock of motile colloids cruising through obstacles in the experiment of [Morin *et al.* 2016]. **(d):** Snapshot of the band phase being stable in the presence of multiple localized obstacles (green dots) [Chepizhko *et al.* 2013]. **(e):** Snapshot of polar vortices in the Vicsek model with chiral disorder [Ventejou *et al.* 2021]. **(f):** Snapshot of a band reversal in the model of [Sakaguchi & Ishibashi 2019].

The homogeneous ordered phase is also unstable in the presence of extensive disorder. [Ventejou *et al.* 2021] introduced disorder in the form of chirality, by endowing the particles with an intrinsic will to rotate. They showed that any amount of chirality destroys the order and gives rise to, among other types of structures, polar vortices. They traced this back to the generic instability of the ordered homogeneous solution of the hydrodynamic theory that they derived from the particle-level model. Scattered obstacles also qualitatively modify the nature of the ordered phase, which was first believed to have quasi long-ranged order [Chepizhko *et al.* 2013, Toner *et al.* 2018] but recent numerical evidence shows that strong non-self-averaging effects prevent elucidating the nature of the asymptotic state [Duan *et al.* 2021]. This problem has also been approached experimentally in [Morin *et al.* 2016] by examining how motile colloids cruise between randomly positioned microfabricated obstacles (See Fig. 3.1c). The study reported that the system undergoes a first-order phase transition from collective to isotropic motion when increasing the amount of disorder. In contrast, the characteristic Vicsek bands were found to be robust structures in the presence of spatial quenched disorder [Duan *et al.* 2021, Chepizhko *et al.* 2013] (See Fig. 3.1d). [Ventejou *et al.* 2021] reported the Vicsek bands to coexist with polar vortices (See Fig. 3.1e) and even resist a finite amount of chirality in the infinite size limit, confirming the stability of such bands. Contrary results were obtained in [Sakaguchi & Ishibashi 2019]. They studied a simple model consisting of stacked $1d$ AIM-like models interacting only through alignment between adjacent rows, without vertical diffusion of the particles, and observed the formation of a band traveling the system. They witnessed the reversal of a single row propagating to the nearby rows, triggering a destabilization of the band (See Fig. 3.1f). As will be explained in this chapter, such reversals are also observed in the original bidimensional AIM and constitute natural $2d$ extensions of the $1d$ reversals detailed in Chapter 2.

In another recent development, the Toner-Tu phase was shown to be fragile to rotational anisotropy [Solon *et al.* 2022]. A field with q-fold symmetry influencing particle orientations destroys the scale-free nature of the ordered phase at large scales, leading to Gaussian fluctuations and short-range correlations. The large scale behaviour of Vicsek-type models, in presence of anisotropy, is then the same as that of the AIM in the homogeneous ordered and coexistence phases.

3.1.2 Metastability of the flocking phase

In this chapter, we analyze the stability of the ordered phases in the AIM and establish their metastability in any $d \geq 2$. We first explore the stability of the order in the coexistence phase of the bidimensional AIM, where we observe destabilizations to spontaneously occur at the front of the bands and propagate through it. Increasing density, we also report nucleation of destabilizations in the homogeneous ordered phase, leading to a counter-propagating droplet. In both the coexistence and the homogeneous ordered phase, we find destabilizations to be the result of local, fluctuation-induced events. To test if destabilizations occur for all parameters, we induce them “by hand” and find that finite-size perturbations can destabilize the ordered phase everywhere on the phase diagram. In the thermodynamic limit, even if its rate of occurence is very small, such a perturbation can happen spontaneously so that the entire homogeneous ordered phase is metastable. We also introduce an obstacle against which particles collide and observe that it can trigger the nucleation of a droplet, depending on the collision scenario that we use.

To support our statement about the metastability of the flocking phase, we use a d-dimensional continuum description of the AIM and we show that droplets of particles moving in the direction opposite to that of the ordered phase can propagate while expanding. Finally, considering the same continuum theory in $2d$, albeit with a vectorial order parameter, we numerically show that any amount of vertical advection hinders the propagation of induced perturbations, pointing towards a fundamental difference between scalar and vectorial order parameter.

This chapter is organized as follows: after defining the d-dimensional AIM and exploring its $2d$ phase diagram in Sec. 3.2, we consider numerical simulations and report in Sec. 3.3 spontaneous nucleation of counter-propagating growing droplets both in the coexistence phase (Sec. 3.3.1) and in the ordered phase (Sec. 3.3.2). We then probe the nonlinear response of the ordered phase to strong localized perturbations in Sec. 3.4 and demonstrate in Sec. 3.4.1 that a droplet polarized oppositely to the surrounding ordered background can grow in all directions. We also observe the formation of such droplet to be triggered by the presence of an obstacle in Sec. 3.4.2. We then show numerically and analytically that the same scenario takes place in the relevant hydrodynamic theory in Sec. 3.5. We find that droplet growth is induced by the ballistic propagation of its domain walls in Sec. 3.5.2 and characterize its shape in any dimension $d \geq 2$ in Sec. 3.5.3. We conclude by observing the fate of such a droplet in a vectorial version of the hydrodynamic theory in Sec. 3.6.

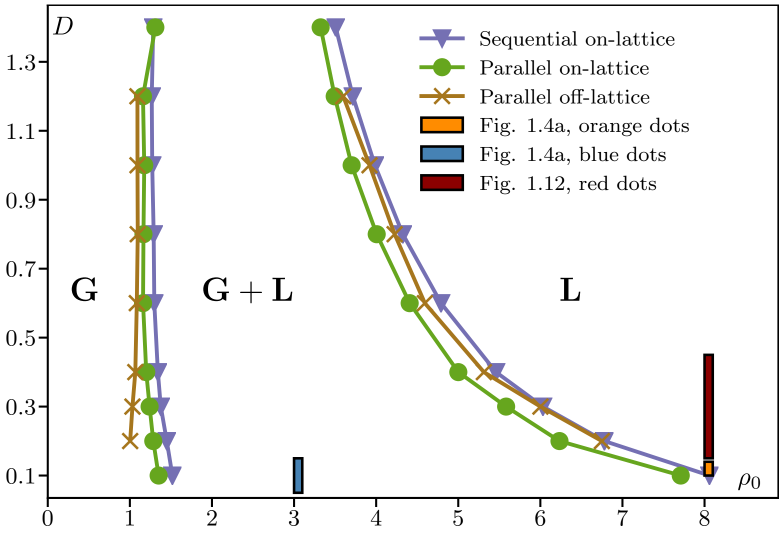

Figure 3.2: $\rho_0 - D$ phase diagram for the three simulation techniques. The separation between Gas and Gas+Liquid is the density of the liquid band, while the separation between Gas and Gas+Liquid corresponds to the density of the gas. We observe qualitative agreement. The colored squares correspond to the parameters used in the figures indicated in the legend. Parameters : $L_x = 400$, $L_y = 100$, $\rho_0 = 3$, $v = 1$.

3.2 Active Ising model

We consider the same model as in Chapter 2 but on a d-dimensional hypercubic lattice. The alignment dynamics is the same on-site ferromagnetic alignment. We consider a slightly different parametrization of the hopping rates compared with Chapter 2 with self-propulsion taking place along the lattice vector $\mathbf{e}_x$ in a direction given by the particles spins s: particles at site $\mathbf{i}$ hop at rate v to the site $\mathbf{i} + s\mathbf{e}_x$ and we add a symmetric diffusion at rate D in the remaining $(d-1)$ dimension. We first compute the phase diagram in the $D - \rho_0$ plane using three different simulation techniques (Fig. 3.2). Consistently with previous work [Solon & Tailleur 2013, Solon & Tailleur 2015], we report a phase diagram with three phases: a disordered gas phase (**G**) and an ordered, flocking, liquid phase (**L**) separated by a coexistence region where a macroscopic dense liquid domain moves in the remaining gas (**G + L**). Remarkably, the coexistence region widens as D is approaching zero, so that the homogeneous ordered phase is

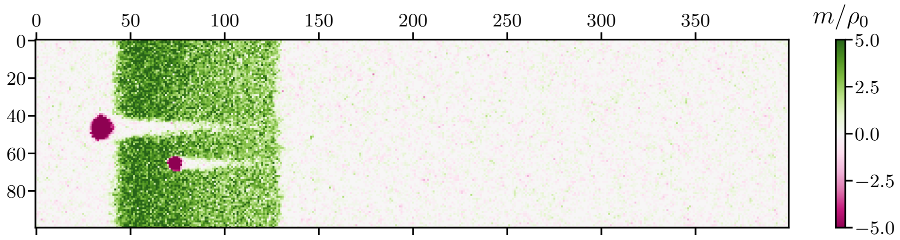

Figure 3.3: Spontaneous reversals off-lattice. Parameters : $\rho_0 = 3$, $L_x = 400$, $l_y = 100$, $v_0 = 1$, $D = 0.08$, $\beta = 2$.

observable only at very high densities.

The results presented in this chapter were mainly obtained through a random sequential update simulation of the AIM dynamics, already detailed in Chapter 2. The observed phenomenology remains the same for other simulation techniques. To support this claim, we compare the effect of parallel updates on-lattice (green dots in Fig. 3.2), random sequential updates on-lattice (purple triangles) and parallel updates off-lattice (brown crosses). In the parallel update scenario, all positions and spins are updated in parallel during a timestep. The off-lattice simulation was described in Chapter 2. We find that the different algorithms give the same qualitative phase diagram, with only quantitative differences of the order of 30%.

3.3 Spontaneous destabilizations

3.3.1 In the coexistence phase

In the coexistence phase of the AIM, a single ordered band travels in a disordered background [Solon & Tailleur 2015]. At small D, we observe spontaneous destabilizations in the band. The scenario in $2d$ is somewhat similar to a reversal in the $1d$ case detailed in Chapter 2: A fluctuation at the front of the band, in the region connecting the liquid and the gas, can reverse the first few sites. It then propagates through the liquid band, reversing the particles as it progresses (See Fig. 3.3 for a snapshot off-lattice).

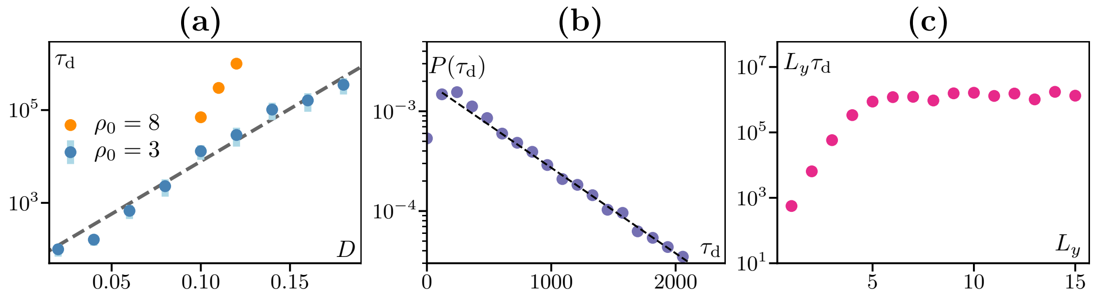

Figure 3.4: Destabilization time. **(a):** Average time for a spontaneous destabilization to occur in the coexistence phase (blue dots) and in the homogeneous phase (orange dots), indicated by the squares of same colors in the phase diagram Fig. 3.2. Errorbars at 3 standard deviations over 50 runs are shown in lighter colors. **(b):** Probability density function of the destabilization time τ_d. **(c):** Average destabilization time multiplied by the vertical size L_y as a function of L_y. Parameters : $\rho_0 = 3$ (b,c); $L_x = 200$; $L_y = 100$ (a,b); $D = 0.06$ (b), $D = 0.1$ (c); $\beta = 2$; $v = 1$.

We compute the time τ_d needed for such a destabilization to occur as a function of D. To do so, we organize particles in a vertical strip which quickly relaxes to the phase separated state: a dense band of positive magnetization in a dilute gas. We detect a destabilization whenever one of the rows reaches a negative total magnetization. Looking at the blue dots in Fig. 3.4a, we observe an exponential increase, compatible with the intuition that diffusion damps fluctuations, hindering their propagation in the liquid band. At fixed diffusion coefficient D, looking at the probability density of τ_d on Fig. 3.4b, we observe an exponential tail indicating a constant rate of destabilization, in line with fluctuation-induced events, except at small times where the initial condition is important. Since destabilizations are initiated at the front of the band, we expect their rate of occurence to increase with the interface length between liquid and gas. This is indeed what we observe in Fig. 3.4c: computing the destabilization time as a function of vertical size, $L_y\tau_\mathrm{d}$ quickly reaches a plateau[1] indicating that $\tau_\mathrm{d} \propto {L_y}^{-1}$: destabilizations result from local events. Together with a constant rate of occurrence, we deduce that in the thermodynamic limit ($L_y \to \infty$), the band is metastable.

---

[1] Note the intermediate region where the destabilization time increases from the 1d case ($L_y = 1$) to the 2d case ($L_y \gtrsim 5$).

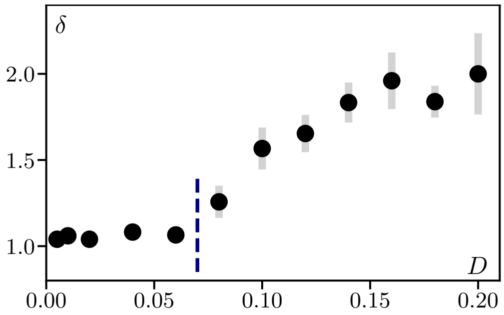

Figure 3.5: Vertical spreading δ of the destabilizations in the band phase as a function of D. The blue dashed line is the theoretical prediction of the transition from one-row reversal to multiple-row reversal Eq. (3.2). Parameters : $\rho_0 = 3$, $L_x = 200$, $L_y = 100$, $\beta = 2$, $v = 1$.

At small D, the rows constituting the system are weakly interacting and we observe the $1d$ behaviour: destabilizations take the form of a $1d$ reversal on a single row (Fig. 3.6a), leaving the rest of the band unaffected. At larger D, the destabilization propagates to adjacent rows, and we observe a vertical spreading (Fig. 3.6b). A simple argument can explain the transition between these two behaviours. Let us reintroduce the lattice spacing explicitly to understand its effect. Particles thus hop at rate Da^2 plus a rate va in the direction of their spin. For a droplet to spread vertically it must be able to “invade” the adjacent sites. Concretely, when a particle jumps on a site of opposite magnetization, it aligns with the new environment on a time scale $\tau_a = \omega_0 e^{\beta}$. If a sufficient number of particles have jumped during this time scale they can overwhelm the particles of opposite magnetization and flip the site. In practice, the vertical flux is

$$J = -D\,\frac{m_\mathrm{o} - m_\mathrm{d}}{a} \tag{3.1}$$

During a time τ_a, $J\tau_a/a$ particles hop on (say) the site on top, so that they flip the arriving site if

$$D > \frac{a^2}{\tau_a}\frac{1}{1 + \left|\frac{m_\mathrm{d}}{m_\mathrm{o}}\right|} \tag{3.2}$$

$m_\mathrm{d}/m_\mathrm{o}$ is of order 1 as we see in Fig. 3.6. Together with the lattice spacing $a = 1$, $\omega_0 = 1$ and $\beta = 2$, this gives us an estimate critical value $D_c \approx 0.07$ for the fluctuation to grow vertically.

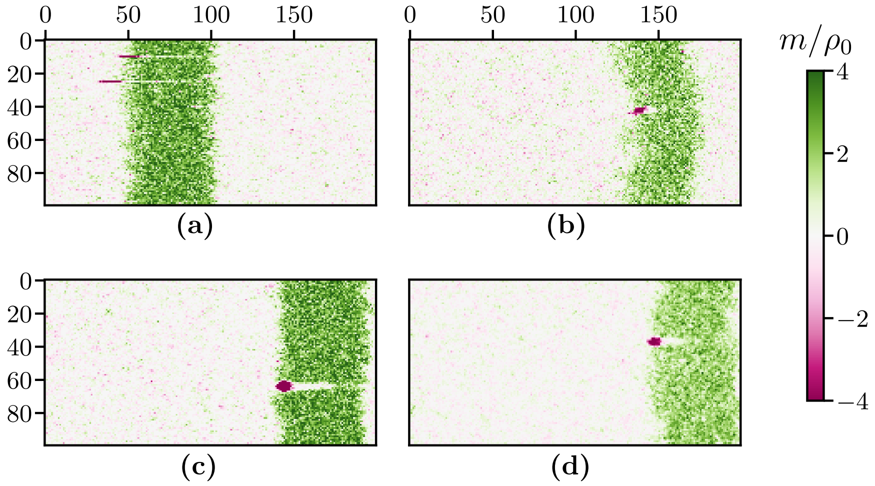

Figure 3.6: Spontaneous reversals on-lattice in the coexistence region varying the lattice spacing a. **(a-b):** $a = 1$. **(c-d):** $a = 1/3$. Parameters: $\rho_0 = 3$, $L_x = 200$, $L_y = 100$, $\beta = 2$, $v = 1$, $D = 0.02$ (left column), $D = 0.16$ (right column).

We first test this prediction by measuring the maximal vertical extension δ of spontaneous destabilizations as a function of D which corresponds to the number of vertically contiguous sites of negative magnetization when it leaves the band. The results are shown in Fig. 3.5a, where we observe a transition from single-row to multiple-rows reversals, occurring for $D_c \approx 0.08$, consistent with the value predicted by our theory. Next, we test the effect of lattice spacing. In order to change a keeping the interaction surface constant, we need to allow for alignment with neighbouring sites. We consider here alignment on 3×3 sites around the particle. Rescaling $D \to 9D$, $v \to 3v$, $\rho_0 \to \rho_0/9$ then amounts to choosing $a = 1/3$. Eq. (3.2) then predicts a much lower threshold $D_c = 0.007$ that is consistent with the vertically spreading droplets that we observe in simulations in this case, see Fig. 3.6c.

3.3.2 In the ordered phase

We also observe spontaneous destabilizations in the ordered phase at small D (See Fig. 3.7, top row, for a serie of snapshots during a destabilization). As in the coexistence phase, the average destabilization time τ_d diverges exponen-

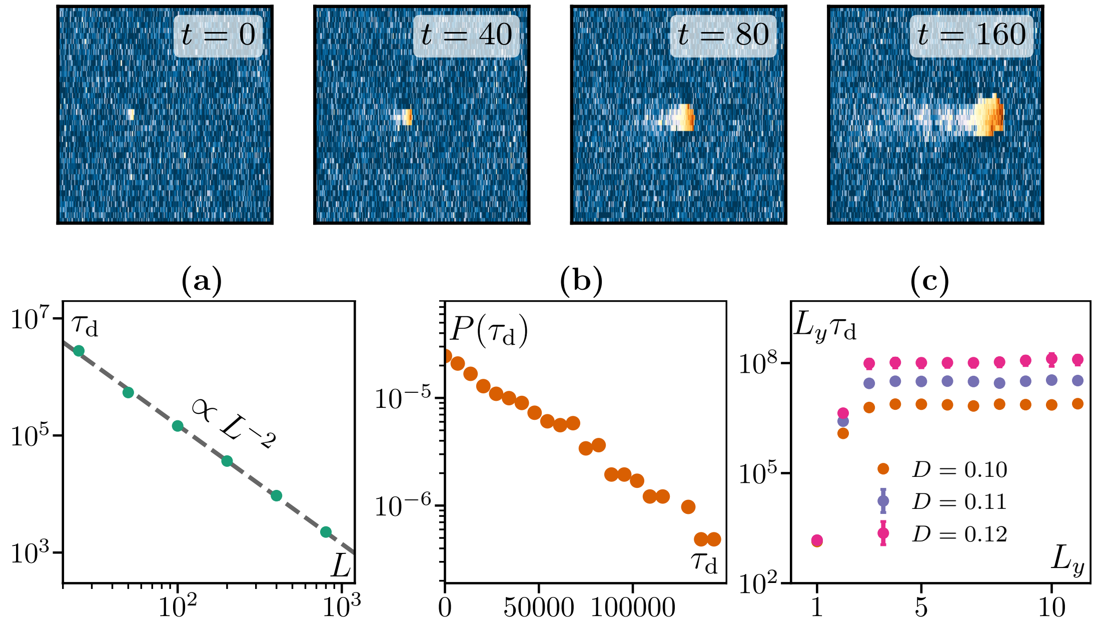

Figure 3.7: **Top:** Snapshots of a spontaneous destabilization showing the growing droplet. Size of the window 400×40. **(a):** Average nucleation time τ_d in a system of size $L \times L$. **(b):** Probability density function of the nucleation time τ_d on a system of size 200×200. **(c):** Average time required for a spontaneous nucleation to occur in the ordered phase of a system of size $200 \times L_y$ multiplied by L_y as a function of L_y. Parameters (See orange square in the phase diagram Fig. 3.2): $\rho_0 = 8$, $v = 1$, $\beta = 2$, $D = 0.1$ (top row, b, c).

tially with D (See orange dots on Fig. 3.4a). This explains why no one ever reported any destabilization for the parameter values usually considered in the literature (around $D = 1$ and thus with very long destabilization times at practically unattainable system sizes). We find that $\tau_\mathrm{d} \sim 1/L^2$ (Fig. 3.7a) which is characteristic of nucleation events resulting from local fluctuations, at uniform rate per unit area. The exponential distribution of the destabilization times in Fig. 3.7b moreover indicates that the rate is constant in time, as expected in a stationary regime. To conclude, in both the coexistence and the ordered phase, the destabilizations result from local fluctuation-induced nucleations occurring at constant rate, so that the entire flocking phase is metastable in the thermodynamic limit.

Since the ordered phase was established to be unstable in the $1d$ AIM (See Chap. 2), in the limit of small vertical size, we expect to recover the $1d$ behaviour of a metastable ordered phase. Considering systems of size $200 \times L_y$ (Fig. 3.7c), we indeed observe destabilizations, τ_d increasing rapidly with L_y from its low $1d$ value (at $L_y = 1$). We observe that $\tau_\mathrm{d} L_y$ quickly reaches a plateau so that beyond a certain width, flipping the ordered phase does not require a larger fluctuation. This size can thus be interpreted as a critical nucleus r_c needed for a droplet to invade the system and happens for strips as narrow as $L_y = 3 \sim 5$. Note that the asymptotic saturation value of $\tau_\mathrm{d} L_y$ increases exponentially fast with D, as already mentioned above.

3.4 Induced destabilizations

Extrapolating the data shown in the previous section, we concluded that the ordered phase should be metastable for all parameters. However, since τ_d increases exponentially with D, destabilizations are not observed in practice in simulations for D of order 1. To test our scenario, we instead induce "by hand" the destabilization by introducing a counter-propagating droplet in the ordered phase in Sec. 3.4.1. We find a critical radius beyond which a perturbation propagates and destroys the ordered phase. We then probe the stability of the order to the presence of a localized obstacle in Sec. 3.4.2, and report the formation of a droplet at the front of the obstacle which then plays the role of a nucleation point.

3.4.1 Droplet propagation

Introducing a large enough counter-propagating droplet of density ρ_d^0 in the ordered phase of density ρ_o, we observe that it grows (purple region) (Fig. 3.8a-b) at the expense of the ordered phase, leaving in its wake a dilute, disordered comet-like structure (white region). These different regions are separated by domain walls that we characterize later. The local density and polarization, defined as $p_\mathbf{i} \equiv m_\mathbf{i}/\rho_\mathbf{i}$, in these three regions are illustrated in Fig. 3.8c, which shows their profile along the central axis. The maximal density in the droplet $\rho_\mathrm{d} > \rho_\mathrm{o}$ and magnetization m_d are constant in time. We note that the polarization inside the droplet is also constant and approximately opposite to that of the ordered phase: $p_\mathrm{d} \simeq -p_\mathrm{o}$.

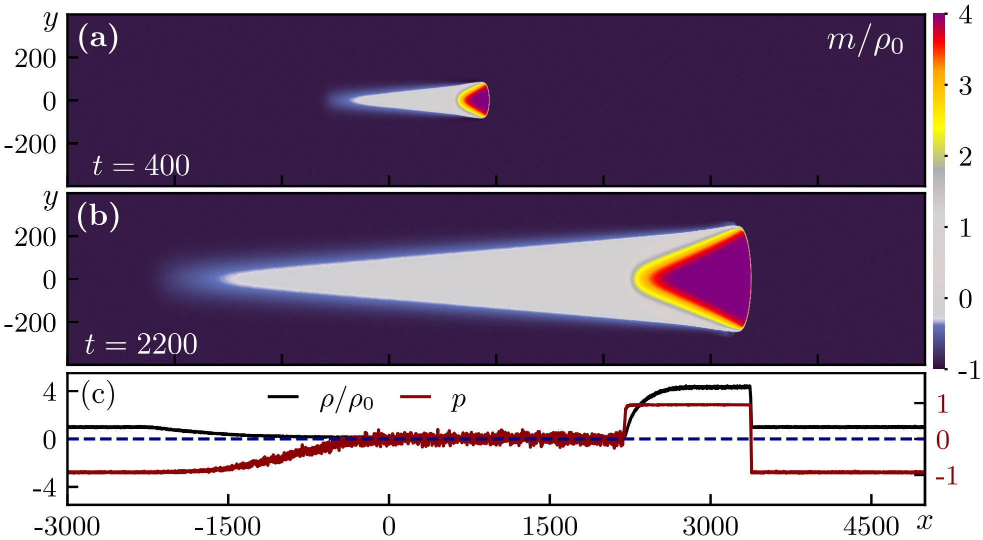

Figure 3.8: Simulations of the 2d AIM. **(a-b)** Snapshots of the magnetization field following the introduction in the ordered phase of a counter-propagating droplet at $x = y = t = 0$ ($r = 10$, $\rho_{\rm d}^0 = 5\rho_{\rm o}$), averaged over 100 runs. **(c)** Polarization (red) and density (black) profiles at $y = 0$ for the snapshot shown in (b). Parameters: $v = 1$, $D = 1$, $\rho_{\rm o} = 10$, $\beta = 2$, $(L_x, L_y) = (8000, 800)$.

For an initial droplet of small radius r, the perturbation typically disappears and the ordered phase is restored. Varying r allows us to estimate the radius $r_{\rm c}$ beyond which the initial droplet grows[2]. Repeating the experiment many times (100 times in Fig. 3.9), we find that the probability that the droplet reverses the ordered phase, that we denote by $P_{\rm r}(r)$, increases sharply from near-0 to near-1 values when r is increased and we define $r_{\rm c}$ by $P_{\rm r}(r_{\rm c}) = \frac{1}{2}$. In practice we consider that we have a reversal when the droplet has propagated over a large enough distance ($\Delta x = 50$), so that we are sure it will continue to propagate. The precise procedure used to detect a reversal is detailed in appendix A.

We find that $P_{\rm r}(r)$ becomes rapidly independent of the system size as the latter is increased (Fig. 3.9a) and measure finite values of $r_{\rm c}$ at all parameter values probed in the ordered phase. Remarkably, $r_{\rm c}$ decreases weakly as T is decreased deeper into the ‘ordered’ phase (Fig. 3.10a). This is markedly different from

---

[2] Keeping r fixed and increasing $\rho_{\rm d}^0$ leads to similar results, see Fig. 3.9b.

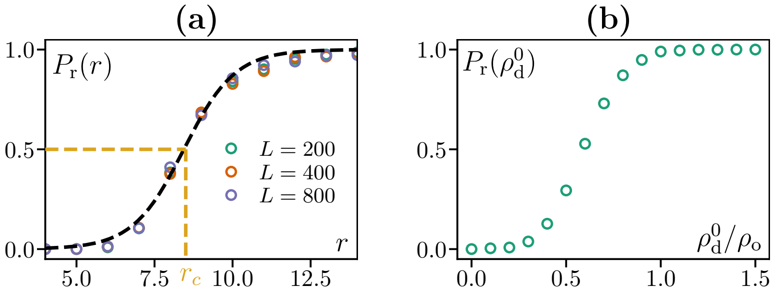

Figure 3.9: **(a):** Reversal probability $P_r(r)$ for $\rho_d^0 = 1.2\rho_o$. The dotted line is a fit to a hyperbolic tangent used to extract r_c. **(b):** Same as (a), for a droplet of initial radius $r = 6$ as a function of the droplet initial density ρ_d^0 for $(L_x, L_y) = (200, 100)$. Parameters: $v = 1$, $D = 1$, $\rho_o = 5$, $\beta = 2$.

what was reported for the Vicsek model [Codina *et al.* 2022] where a perturbation reverses the ordered phase only in a finite fraction of the phase diagram next to the coexistence region, with r_c diverging sharply as T is decreased. Note that r_c increases roughly linearly with D, consistently with the intuition that diffusion suppresses perturbations (Fig. 3.10b). We measure r_c for values of D larger than $D = 0.5$ because, as seen in the phase diagram Fig. 3.2, decreasing D at smaller values would bring the systems into the coexistence phase if keeping the same density $\rho_o = 5$. We found r_c to approximately diverge as $1/v$ in the limit $v \to 0$ (see Fig. 3.10a), therefore recovering at $v = 0$ an equilibrium-like behavior where finite-size droplets shrink. Finally, increasing the density of the ordered phase, the critical radius remains almost constant (Fig. 3.10d).

A simple scaling argument based on the characteristic lengthscale in the continuum equation of the AIM accounts for this dependence in v, D and ρ_0. We start with the mean-field hydrodynamic equations presented in Chapter 2:

$$\partial_t \rho = -v\partial_x m + D\nabla^2 \rho \tag{3.3}$$

$$\partial_t m = -v\partial_x \rho + D\nabla^2 m + \omega_0 F(\rho, m)\ , \tag{3.4}$$

where ρ and m are the density and magnetization fields, respectively, and $F = 2\rho\sinh(\beta m/\rho) - 2m\cosh(\beta m/\rho)$. We identify a characteristic lengthscale $\xi = D/v$ and timescale $\tau = D/v^2$. Using rescaled coordinates $\tilde{t} \leftarrow \tau t$ and $\tilde{x} \leftarrow \xi x$, the

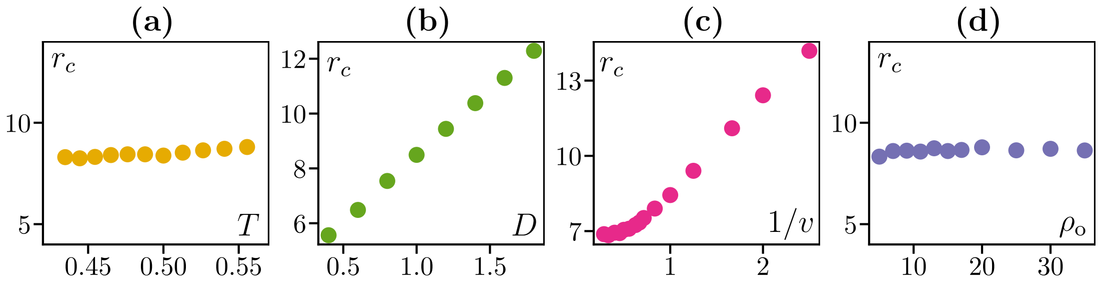

Figure 3.10: Variations of r_c with system parameters. Parameters: $v = 1$ (a,b,d), $D = 1$ (a,c,d), $\rho_o = 5$ (a,b,c), $\beta = 2$ (b,c,d), $\rho_d^0 = 1.2\rho_o$, $(L_x, L_y) = (200, 100)$

dimensionless equations read

$$\partial_{\tilde{t}}\rho = -\partial_{\tilde{x}}m + \tilde{\nabla}^2\rho \tag{3.5}$$

$$\partial_{\tilde{t}}m = -\partial_{\tilde{x}}\rho + \tilde{\nabla}^2 m + \tilde{\omega}_0 F(\rho, m)\ , \tag{3.6}$$

where $\tilde{\omega}_0 = \omega_0 D/v^2$ controls the relaxation time of m. When $\tilde{\omega}_0 \gg 1$, the field m relaxes very rapidly since all other terms in Eq. (3.6) are of order 1, so that its dynamics, on times of order 1, is expected to become independent of the precise value of $\tilde{\omega}_0$. The critical dimensionless radius $\tilde{r}_c$ is then related to the dimensional critical radius r_c by the relation $r_c = \xi\tilde{r}_c$. Thus, restoring the units yields:

$$r_c \propto \frac{D}{v} \tag{3.7}$$

This scaling is only valid in the limit of large $\tilde{\omega}_0$ and is indeed consistent with numerical simulations, where we observe $r_c \propto D$ (Fig. 3.10b) and $r_c \propto v^{-1}$ for small value of v (Fig. 3.10c). Note also that Eqs. (3.5, 3.6) are invariant under a rescaling of ρ and m, so that r_c is independent of ρ_o as observed in Fig. 3.10d.

The behavior of r_c shown in Fig. 3.10 indicates that a finite-size fluctuation can destabilize the ordered phase everywhere on the phase diagram. Since the nucleation process is local (Fig. 3.7b and Fig. 3.9a), in the infinite-size limit even rare fluctuations happen quickly. This leads us to conclude that the ordered phase is metastable in the thermodynamic limit for all parameters.

3.4.2 Obstacle

We now introduce a small circular obstacle in the ordered phase of the AIM. Concretely, a particle that attempts to hop in the obstacle does not move. Its spin is either reversed (scenario 1) or not (scenario 2).

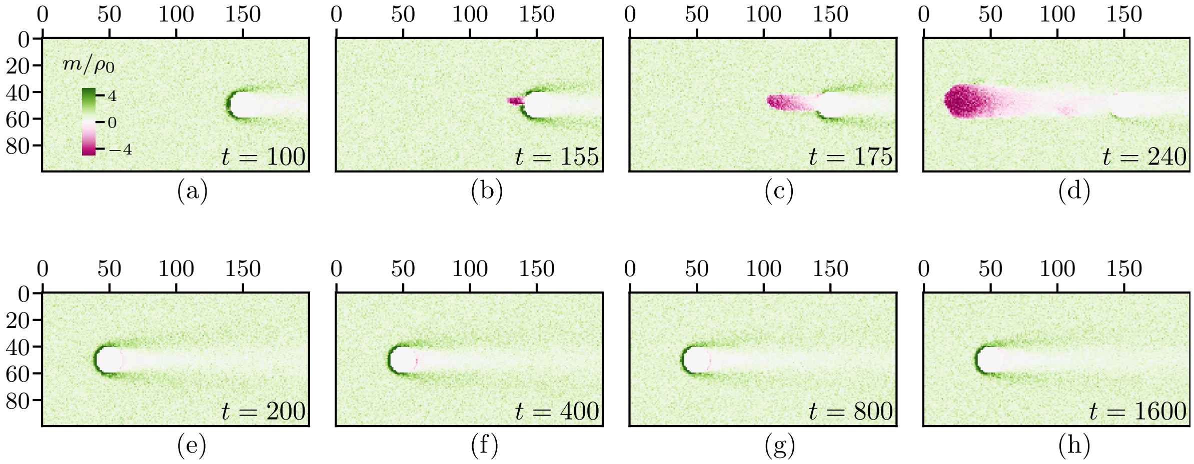

Figure 3.11: Effect of the introduction of an obstacle of radius 10 in the ordered phase of the AIM. **Top row:** Nucleation of a droplet in scenario 1. **Bottom row:** The ordered dense region at the front of the obstacle in scenario 2. Parameters : $\rho_0 = 8$, $L_x = 700$, $L_y = 100$, $\beta = 2$, $v = 1$, $D = 0.4$.

We could imagine the obstacle to serve as a nucleation point for destabilizations in both cases. In fact, we report a more complex picture. In scenario 1, at fixed density, we progressively increase the diffusion coefficient D, starting near the boundary between coexistence phase and order, as indicated by the blue rectangle in Fig. 3.2. At low values of D, the presence of an obstacle triggers the formation of a cluster of counter-propagating particles at the front (Fig. 3.11b). It eventually separates from the obstacle (Fig. 3.11c) and grows following the droplet dynamics (Fig. 3.11d) described in Sec. 3.4. This obstacle-induced droplet nucleation remains observable while increasing D, albeit on much larger timescales, as can be seen on Fig. 3.12. On the contrary, in scenario 2, in which the particles' spin remain unchanged upon collision, they aggregate at the front of the obstacle, eventually sliding along its edges by diffusion (Fig. 3.11e-h). This creates an ordered dense region in the flow which does not trigger the nucleation of a droplet, in opposition to scenario 1. To summarize, in scenario 1, the obstacle serves as a nucleation point and thus decreases τ_d. This is not the case in scenario 2 so we conjecture that τ_d is the same as in the absence of obstacle.

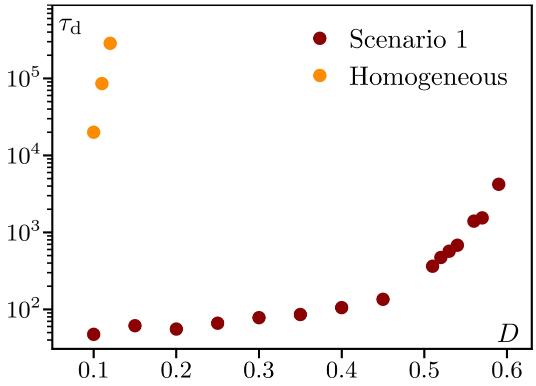

Figure 3.12: Destabilization time of the ordered phase as a function of D in the presence of an obstacle for scenario 1 compared with the spontaneous destabilization time of the homogeneous ordered phase. Parameters (See red square in the phase diagram Fig. 3.2): $\rho_0 = 8$, $L_x = 700$, $L_y = 100$, $\beta = 2$, $v = 1$.

Comparing with the results of [Codina *et al.* 2022], we observe that the mechanisms leading to a reversal are different. In the Vicsek case, when particles keep their direction upon collision, the nucleation takes place at the rear of the obstacle. It then recruits more and more particles as it moves along and detaches from the obstacle, forming a dense, curved band. We did not observe this to happen in the AIM case, where fluctuations at the rear of the obstacle are confined within its wake. Conversely, when particles reverse their direction upon collision, no reversals are reported in the Vicsek case, while they are easily observed in a region extending far into the AIM ordered phase.

3.5 Hydrodynamic description of the propagating droplet

To characterize the mechanisms underpinning droplet growth and to test their robustness to microscopic details, we now study a continuum description of the AIM. Through the simulation and analysis of continuous equations, we first identify a ballistic scaling in the droplet growth in Sec. 3.5.1. We then show the existence of propagating domain walls and predict their velocity, that we find in agreement with numerical measurements in Sec. 3.5.2. We then turn to the characterization of the droplet and rationalize analytically its front shape in Sec. 3.5.3.

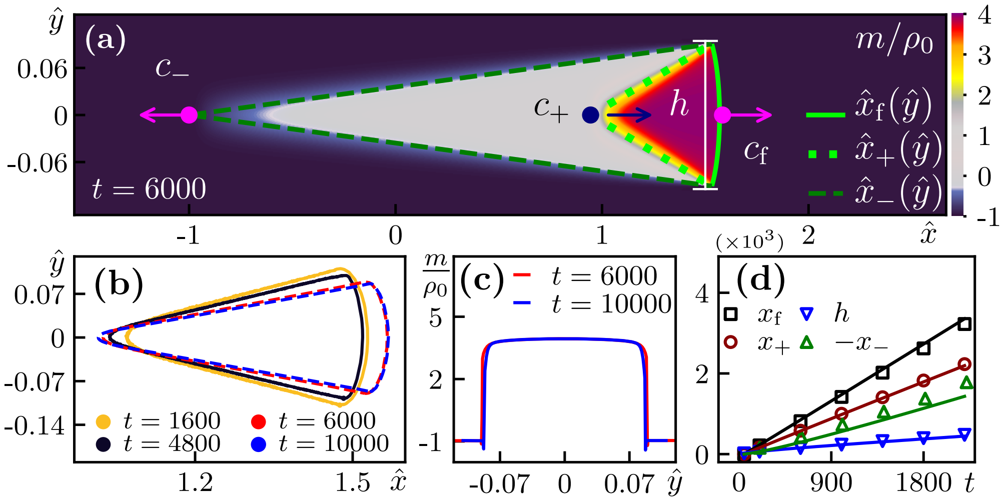

Figure 3.13: **(a)** Snapshot of the m/ρ_o field obtained by integrating Eqs. (3.8,3.9) starting from a counter-propagating droplet introduced in the ordered phase solution at $t = 0$ ($r = 10$, $\rho_\mathrm{d}^0 = 12\rho_\mathrm{o}$). Straight and parabolic green lines are guides to the eye. **(b)** Isodensity curves at $\rho = (\rho_\mathrm{d} + \rho_\mathrm{o})/2$ in ballistically-rescaled coordinates for microscopic (solid lines) and hydrodynamic (dashed lines) simulations. **(c)** Cross-sectional plots of the magnetization in PDE simulations along the maximal-width line shown in white in (a). **(d)** Positions of the front (x_f) and rear (x_+) droplet interfaces, and of the end of the comet (x_-) at $y = 0$, together with the droplet width h. Symbols and lines correspond to microscopic and PDE simulations, respectively. Parameters: As in Fig. 3.8(a-b) except $(L_x, L_y) = (8000, 600)$ in panel (a).

3.5.1 Ballistic scaling

Following established procedures used to study coarsening and nucleation [Bray 2002, Krapivsky *et al.* 2010], we focus on the low-T large-density regime where the ordered phase is expected to be most stable. We consider the mean-field hydrodynamics of the AIM [Solon & Tailleur 2015] in d dimensions:

$$\partial_t \rho = -v\partial_x m + \nabla \cdot \bar{D}\nabla\rho \tag{3.8}$$

$$\partial_t m = -v\partial_x \rho + \nabla \cdot \bar{D}\nabla m + F(\rho, m) \;, \tag{3.9}$$

where $\bar{D}$ is a diagonal matrix whose elements are $D_x = D + v/2$ and, for any other coordinate, $D_\perp = D$. Numerical integration of Eqs. (3.8,3.9) in 2d, shown in Fig. 3.13a for the same parameters as in Fig. 3.8a-c, recapitulate the phenomenology observed in microscopic simulations: an initial droplet grows, leaving in its wake a low-density comet. We observe that the system grows ballistically. To show this, we plot iso-density lines in the ballistic rescaling $(\hat{x}, \hat{y}) = (x/t, y/t)$ in Fig. 3.13b which shows a good collapse. The cross-section along the y direction also obeys the same scaling as shown in Fig. 3.13c. Finally, we define the position of the three interfaces between the ordered background, the droplet, and the comet, which we parametrize as $\hat{x}_{\rm f}(\hat{y})$, $\hat{x}_+(\hat{y})$, and $\hat{x}_-(\hat{y})$, respectively (Fig. 3.13a) and show in Fig. 3.13d that, consistently, they increase ballistically. We now turn to the analytical study of Eqs. (3.8,3.9) in $d \geq 2$.

3.5.2 Propagating domain walls

Assuming that the axisymmetry observed in 2d is maintained in higher dimensions, we distinguish coordinates parallel and normal to the self-propulsion: $\mathbf{r} = x\mathbf{e}_x + \mathbf{r}_\perp$. We first characterize the domain walls connecting the droplet, the comet, and the ordered background along the symmetry axis of the droplet ($\mathbf{r}_\perp = 0$) before discussing the full droplet shape. Due to the ballistic scaling, we expect that the unscaled interfaces become locally flat at $\mathbf{r}_\perp = 0$ at late times in any direction normal to $\mathbf{e}_x$. The domain walls connecting the different regions at $\mathbf{r}_\perp = 0$ can then be analyzed by setting $\nabla_{\mathbf{r}_\perp} = 0$ in Eqs. (3.8,3.9), which makes the problem effectively one-dimensional. To proceed, we employ a Newton mapping, as was used before to find propagating solutions in the phase coexistence region [Caussin *et al.* 2014, Solon *et al.* 2015b], to cast the characterization of the interfaces into a classical mechanics problem.

We first discuss the front interface between the droplet and the ordered background, whose (unknown) speed we denote by $c_{\rm f}$. Shifting to the comoving frame by considering $z = x - c_{\rm f}t$, we look for stationary solutions of Eqs. (3.8,3.9), which reduce to

$$D_x\rho'' = vm' - c_{\rm f}\rho' \tag{3.10}$$

$$D_x m'' = v\rho' - c_{\rm f}m' - F(\rho, m) \tag{3.11}$$

where primes denote derivatives with respect to z. At leading order in a gradient expansion, Eq. (3.10) is solved by $\rho(z) \simeq \rho_{\rm o} + v[m(z) - m_{\rm o}]/c_{\rm f}$, where $m_{\rm o}$ is the magnetization in the ordered phase. Using this in Eq. (3.11) then leads to

$$D_x m'' = -\gamma(c_\mathrm{f}) m' - \partial_m V(m, c_\mathrm{f}) \ , \tag{3.12}$$

where $\gamma(c_\mathrm{f}) = v(c_\mathrm{f}/v - v/c_\mathrm{f})$ and $\partial_m V(m; c_\mathrm{f}) = F[\rho(m, c_\mathrm{f}), m]$. Interpreting z as time and m as a position, Eq. (3.12) describes the dynamics of a fictitious particle of mass D_x in a potential V with a friction coefficient γ that can be positive or negative depending on whether c_f is larger or smaller than v, respectively.

Propagating fronts correspond to heteroclines $m(z)$ connecting extrema of $V(m)$, which is always bimodal in the ordered phase (Fig. 3.14a). When $v = 0$, $V(m)$ is symmetric and heteroclines exist only for $\gamma = c_\mathrm{f} = 0$, which corresponds to static domain walls and a droplet magnetization $m_\mathrm{d} = -m_\mathrm{o}$, as in equilibrium. When $v \neq 0$, $c_\mathrm{f} = 0$ corresponds to a diverging friction and no static heterocline exist: fronts are thus always propagating, $V(m)$ is asymmetric so that $|m_\mathrm{d}| \neq |m_\mathrm{o}|$, and $c_\mathrm{f} = v(m_\mathrm{d} - m_\mathrm{o})/(\rho_\mathrm{d} - \rho_\mathrm{o})$. To show that such heteroclines exist, we look for a trajectory $m(z)$ that corresponds —without loss of generality— to a right-going droplet. The fictitious particle then starts with a vanishing speed $m' = 0$ at $m = m_\mathrm{d}$, the positive maximum of V, and ends—also with a vanishing speed—at $m = m_\mathrm{o} < 0$. Equation (3.10) implies that $m_\mathrm{d} = \frac{c_\mathrm{f} - v p_\mathrm{o}}{c_\mathrm{f} + v p_\mathrm{o}} m_\mathrm{o}$, where $p_\mathrm{o} = m_\mathrm{o}/\rho_\mathrm{o} \in [-1, 0]$, so that $\rho_\mathrm{d} = \frac{c_\mathrm{f} - v p_\mathrm{o}}{c_\mathrm{f} + v p_\mathrm{o}} \rho_\mathrm{o}$. Using the explicit expression of F, one finds that $\Delta V \equiv V(m_\mathrm{d}) - V(m_0) > 0$ so that we need a positive friction —and thus $c_\mathrm{f} \geq v$— that dissipates exactly the energy ΔV. By continuity, a solution with $v < c_\mathrm{f} < \infty$ always exists as shown by considering the limiting cases: For $c_\mathrm{f} = v$, $\gamma(c) = 0$, the energy is conserved and the particle overshoots to $m = -\infty$; for $c_\mathrm{f} \to \infty$, the friction diverges and the particle ends up trapped at the minimum $m = 0$. The value of c_f can then be found, e.g., by dichotomy.

In Fig. 3.14b, we compare the mean-field predictions of our domain-wall theory for the front speeds to microscopic simulations in the large ρ_o limit, where mean-field is expected to work well. Despite the crude approximate solution of Eq. (3.10), the agreement is very good without any fitting parameters. Importantly, our theory predicts that $c_\mathrm{f} > v > c_+$ so that the droplet grows in time. Similarly, the comet spreads at a speed $c_+ - c_- = 2v|p_\mathrm{o}|$. We note that a more complex structure emerges as β decreases away from the low-temperature limit studied here. In particular, the density of the comet increases, eventually leading to its polarization, as can be seen in Fig. 3.15.

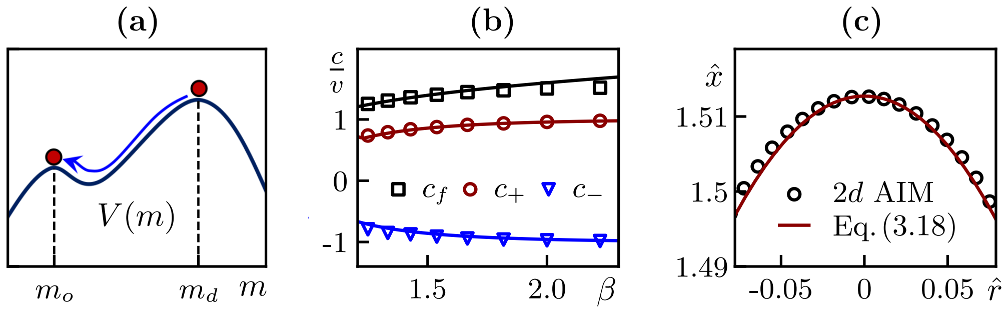

Figure 3.14: **(a)** Potential $V(m)$ entering the Newton mapping with an illustration of the heterocline corresponding to the interface between the droplet and the ordered phase. **(b)** Speeds of the 3 interfaces as a function of β. Solid lines correspond to values predicted by the Newton mapping. Symbols are measurements from microscopic simulations with $(L_x, L_y) = (3000, 300)$ and $\rho_\text{o} = 30$. Parameters: $D = v = 1$. **(c)** Comet front profiles aligned at $\hat{r} = 0$ from 2d AIM simulations at $t = 4800$ and as predicted by Eq. (3.18).

3.5.3 Droplet shape

We now use the mean-field Eqs. (3.8,3.9) to characterize the transverse droplet shape, which is constant at large time under the ballistic scaling. The diffusion terms in Eqs. (3.8,3.9) then decay as $1/t$ and can be neglected. Using the radial symmetry of the droplet, Eq. (3.8) reduces to

$$(\hat{x}\partial_{\hat{x}} + \hat{r}\partial_{\hat{r}})\hat{\rho} = v\partial_{\hat{x}}\hat{m} \; , \tag{3.13}$$

where $\hat{\rho}$ and $\hat{m}$ are the density and magnetization fields expressed in the reduced coordinates $\hat{x}$ and $\hat{r}{=}|\mathbf{r}_\perp|/t$.

Our domain-wall theory predicts a fixed interface width which therefore vanishes under the ballistic scaling. Therefore, the droplet shape is entirely characterized by the curves $\hat{x}_\pm(\hat{r})$ and $\hat{x}_\text{f}(\hat{r})$ in the large-time limit. (See Fig. 3.13a for an illustration in 2d, where $\hat{r} = |\hat{y}|$.) The three interfaces can be characterized using a similar method. First, we center the profiles around an interface $\hat{x}_i(\hat{r})$ by changing variables to $(\bar{x}, \bar{r}) = (\hat{x} - \hat{x}_i(\hat{r}), \hat{r})$. Using the chain rule and integrating $\bar{x}$ from $-\varepsilon$ to ε then leads to:

$$[\hat{x}_i(\hat{r}) - \hat{r}\partial_{\hat{r}}\hat{x}_i(\hat{r})]\Delta\hat{\rho} = v\Delta\hat{m} + \mathcal{O}(\varepsilon) \; , \tag{3.14}$$

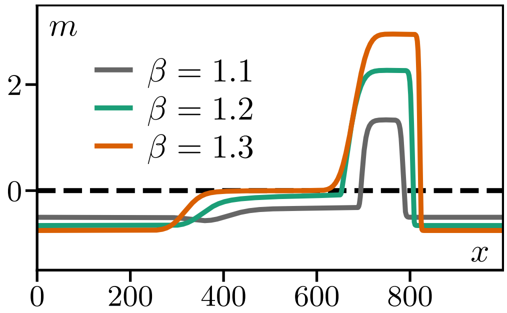

Figure 3.15: Cross-sectional plots of the magnetization in PDE simulations at high T along the horizontal symmetry axis of the droplet. Parameters: $L = 1000$, $\rho_\text{o} = 1$, $v = 1$, $D = 1$.

where $\Delta\hat{\rho}$ and $\Delta\hat{m}$ are the density and magnetization differences across the interface. In the comet, the magnetization vanishes and the density is much smaller than ρ_o, so that $\hat{x}_-(\hat{r})$ satisfies $\hat{x}_- - \hat{r}\partial_{\hat{r}}\hat{x}_- = vp_\text{o}$. Inside the droplet, the ballistic scaling enforces $F = 0$ at long times so that $\hat{m}(\hat{x},\hat{r}) = -p_\text{o}\hat{\rho}(\hat{x},\hat{r})$. For the comet-droplet interface, Eq. (3.14) then leads to $\hat{x}_+(\hat{r}) - \hat{r}\partial_{\hat{r}}\hat{x}_+(\hat{r}) = -vp_\text{o}$. These equations are readily solved by linear relations:

$$\hat{x}_\pm(\hat{r}) = \mp vp_\text{o} + a_\pm\hat{r} \ , \tag{3.15}$$

where $a_\pm$ are finite constants. ($a_\pm = \infty$ corresponds to bands spanning the system.) The case $a_\pm = 0$ corresponds to a degenerate droplet that does not spread in the transverse directions, which is forbidden for $D_\perp \neq 0$. Note that finite $a_\pm$ correspond to the straight interfaces shown in Figs. 3.8 and 3.13.

Finally, we consider the interface between the droplet and the ordered phase. Since ρ_d diverges as $\rho_\text{o} \to \infty$, the density and magnetization jumps require a closer inspection. Inside the droplet, using $\hat{m} = -p_\text{o}\hat{\rho}$, Eq. (3.13) can be rewritten as

$$\left[(\hat{x} - c_+)\partial_{\hat{x}} + \hat{r}\partial_{\hat{r}})\right]\hat{\rho} = 0 \ , \tag{3.16}$$

where we have used $c_+ \simeq -vp_\text{o}$. This implies that $\hat{\rho}$ is a function of $\hat{r}/(\hat{x} - c_+)$ so that, in the large-time limit, isodensity surfaces are cones originating at $(\hat{x} = c_+, \hat{r} = 0)$. In particular, density and magnetization are constant along $\hat{r} = 0$, equal to ρ_d and $m_\text{d} = -p_\text{o}\rho_\text{d}$, respectively. For small $\hat{r}$, we thus expand the density profile as

$$\hat{\rho}(\tfrac{\hat{r}}{\hat{x}-c_+}) = \rho_\text{d}[1 - \tfrac{k}{2}(\tfrac{\hat{r}}{\hat{x}-c_+})^2] \ . \tag{3.17}$$

To solve the interface Eq. (3.14), we first use that $\hat{m} = p_\text{o}\rho_\text{o}$ in the ordered phase and $\hat{m} = -p_\text{o}\hat{\rho}$ in the droplet, to express $v\frac{\Delta\hat{m}}{\Delta\hat{\rho}}$ in terms of $\hat{\rho}$. Using Eq. (3.17) and the expression of c_f, one then gets perturbatively in $\hat{r}$

$$\hat{x}_\text{f} = c_\text{f} - \frac{k\rho_\text{d}}{4v|p_\text{o}|\rho_\text{o}}\hat{r}^2 + \mathcal{O}(\hat{r}^4). \tag{3.18}$$

The transverse density modulation inside the droplet thus leads to the curved shape of the front interface. To compare with simulations, we first estimate the coefficient k by fitting Eq. (3.17) to the density field inside the droplet, and then use it to compare the prediction of Eq. (3.18) with the measured shape, which shows a good agreement (Fig. 3.14c).

All in all, our analytical study puts on even firmer ground the fact that ordered phases are metastable by showing that there always exists ballistically growing solutions with a shape that we can compute and that compares very well to numerical measurements.

3.6 Droplet propagation in vectorial PDEs

As described in Sec. 3.4, simulations of the continuous theory of the AIM show that the order can be reversed through the introduction of a small circular perturbation oriented against the ordered phase. In comparison, [Codina *et al.* 2022] report that the standard Toner-Tu hydrodynamic theory is unable to account for the reversals that they observe in the Vicsek model. There thus seems to be a fundamental difference between scalar and vectorial field theories regarding the stability of the ordered phase to perturbations. To probe this difference, we start from the continuous theory of the AIM Eqs. (3.8,3.9) and consider its vectorial counterpart:

$$\begin{cases} \partial_t\rho = -v\boldsymbol{\nabla}\cdot\mathbf{m} + D\Delta\rho \\ \\ \partial_t\mathbf{m} = -v\boldsymbol{\nabla}\rho + D\boldsymbol{\Delta}\mathbf{m} + \boldsymbol{\mathcal{F}}(\rho,\mathbf{m}) \end{cases} \tag{3.19}$$

where we choose $\boldsymbol{\mathcal{F}} = \left(1 - \gamma\dfrac{\mathbf{m}^2}{\rho^2}\right)\mathbf{m}$ a standard Ginzburg-Landau term imposing a non-vanishing magnetization $|\mathbf{m}| = \rho\sqrt{1/\gamma}$. We find that indeed, no matter how large the initial droplet is, it always splits into two wings that dissolve by

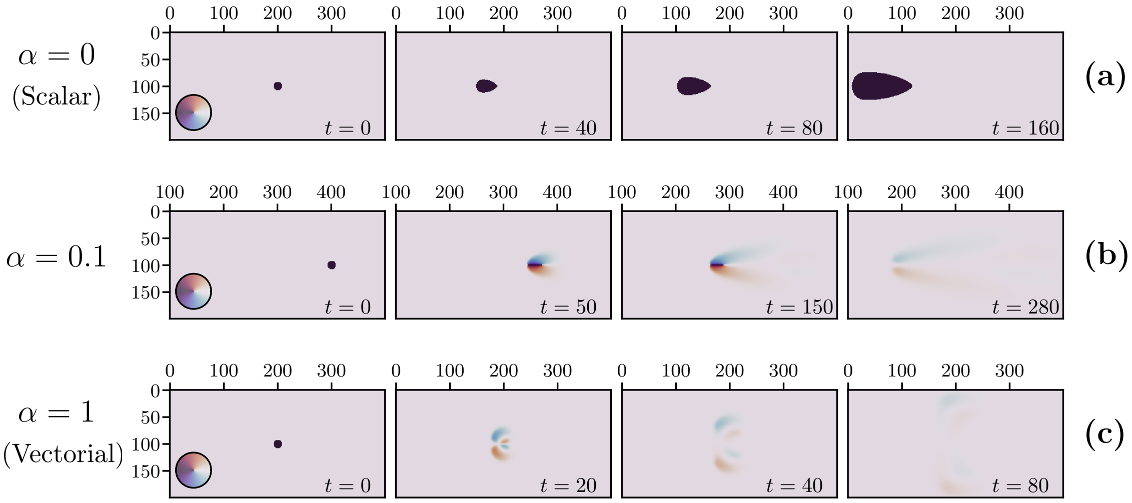

Figure 3.16: Introduction of a counter-propagating circular droplet in the ordered phase of the interpolating continuum theory Eqs. 3.20. The circular colormap on the left panels indicates the direction of the order parameter $\mathbf{m}$. Parameters : $\rho_0 = 1$, $L_x = 400$ (a,c), $L_x = 500$ (b), $L_y = 200$, $v = 1$, $\gamma = 2$, $D = 1$. Initial circular perturbation of radius 10 and of density 10.

spreading away (See Fig. 3.16c), so that the droplet is not able to destabilize the ordered phase.

Going further, we interpolate between the vectorial and scalar cases by introducing a parameter $\alpha \in [0, 1]$ controlling the vertical advection. Eqs. (3.19) are then slightly modified to take into account the interpolation parameter:

$$\begin{cases} \partial_t \rho = -v(\partial_x m_x + \alpha \partial_y m_y) + D\Delta\rho \\ \\ \partial_t m_x = -v\partial_x \rho + [D\mathbf{\Delta m} + \boldsymbol{\mathcal{F}}(\rho, \mathbf{m})]_x \\ \\ \partial_t m_y = -\alpha v \partial_y \rho + [D\mathbf{\Delta m} + \boldsymbol{\mathcal{F}}(\rho, \mathbf{m})]_y \end{cases} \tag{3.20}$$

The case $\alpha = 1$ corresponds to the vectorial version, while we recover the scalar continuum theory for $\alpha = 0$, albeit with a different $\mathcal{F}$. As discussed earlier, droplets can grow in the later, provided that the initial perturbation is large enough, as shown in Fig. 3.16a. Looking at an intermediate case $\alpha = 0.1$ in

Fig. 3.16b, the perturbation initially propagates ballistically, the two wings staying connected at the center. At $t = 280$, they eventually separate and diffuse in the flow. This observation, combined with the analysis of films at larger system sizes and lower values of α, shows that the case $\alpha = 0$ is singular. At any $\alpha > 0$, the perturbation eventually disappears even if it propagates during a transient regime that becomes longer as $\alpha \to 0$.

3.7 Discussion

We have shown that the ordered phases of the active Ising model are metastable to the nucleation of minority-phase droplets. We have first provided numerical evidence of spontaneous destabilizations occuring in the band phase and in the homogeneous ordered phase. We have then probed the response of the ordered phase to induced perturbations and to the presence of a small circular obstacle and have found it to be unstable to such perturbations. Using mean-field theory, we have revealed how the ballistic spreading of the droplet results from the selection of its domain walls and we predicted its asymptotic shape in any dimension. Our results imply that the stability of ordered phases with a discrete symmetry is very different in flocking and equilibrium models.

As suggested by our hydrodynamic analysis, we expect our results to be robust to microscopic details and to apply more broadly to flocking models with discrete-symmetry order parameters. We have verified that off-lattice versions of the AIM also have a metastable ordered phase. We also expect that our results will apply to flocking models with continuous symmetries in the presence of rotational anisotropysince they are well-described by the AIM on large scales [Solon *et al.* 2022]. Moreover, one expects mean-field results to hold better in higher dimensions, so we anticipate our growing droplet solutions to remain valid beyond the $2d$ case studied here. Finally, we evaluated the influence of the symmetry of the order parameter on the stability of the homogeneous ordered phase in continuous descriptions. At least for the parameter values that we tested, we showed numerically that even minor vertical advection inhibits the propagation of induced perturbations.

From a broader perspective, our results suggest two scenarios for the flocking phase of active models, given the numerical results obtained on the Vicsek model in [Codina *et al.* 2022], that suggest that metastability only occurs in a fraction of the Toner-Tu phase. Either these results are confirmed analytically through further research on the Vicsek model and its corresponding continuous theory, thus making systems with discrete symmetries less stable than their continuous-symmetry counterparts – in opposition to the equilibrium case –, or the Toner-Tu phase is also generically metastable.

Chapter 4

Bubbly phase separation

Contents

4.1 Introduction

4.1.1 Motility-Induced Phase Separation

Motility-Induced Phase Separation (MIPS) occurs when interactions between active particles slow them down. As a result, they aggregate in dense regions, triggering a positive feedback loop that leads to the emergence of growing compact aggregates of particles. These aggregates undergo a coarsening process until full phase separation is achieved. Two types of active particles have been shown to display MIPS: Quorum-Sensing Active Particles (QSAPs) and Pairwise-Forces Active Particles (PFAPs). QSAPs mimic bacteria that adapt their speed according to the local density of bacteria that they sense through a chemical released in the surrounding medium. It is more generally common in the biological world in which the motion of individuals is influenced by the local density around them. On the other hand, PFAPs interact via short-range pairwise repulsive interactions, such as hard-core interactions. This interaction slows them down because when two PFAPs collide, they block each other until one of them rotates and resumes its motion. This type of particle includes active Brownian particles and Run-and-Tumble particles.

Both QSAPs and PFAPs undergo MIPS and present similar phase diagrams, but QSAPs are best amenable to analytic treatment because their self-propulsion speed can be written as a functional of the local density. Coarse-graining their large-scale dynamics was shown in [Solon *et al.* 2018a] to lead to an out-of-equilibrium generalization of the Cahn-Hilliard equation for the conserved density field ρ:

$$\partial_t \rho = \nabla \cdot (M \nabla g[\rho]) \tag{4.1}$$

$$g[\rho] = g_0(\rho) + \lambda(\rho)(\nabla\rho)^2 - \kappa(\rho)\Delta\rho \tag{4.2}$$

where M, $g_0(\rho)$, $\lambda(\rho)$ and $\kappa(\rho)$ can be written in term of the microscopic coefficients of the QSAPs dynamics. Note that this description differs from an equilibrium description because for generic functions $\lambda(\rho)$ and $\kappa(\rho)$ which do not satisfy $2\lambda(\rho) + \kappa'(\rho) = 0$, the gradient terms in $g[\rho]$ cannot be written as a functional derivative with respect to the density ρ. However, this description can be mapped onto an equilibrium description upon introduction of a generalized free energy $\mathcal{G}$ and a new non-trivial variable R playing the role the density. The resulting generalized thermodynamics then provide a direct method to predict the phase diagram of QSAPs using standard equilibrium tools [O'Byrne *et al.* 2022]. Moreover, it offers a definition for the generalized pressure as the diagonal coefficients of a generalized stress tensor $\mathbf{\Sigma}$, which is written in term of $\mathcal{G}$ and R.

4.1.2 Negative surface tension and reversed Ostwald ripening

At an interface (say normal to the x-axis) between two regions, the surface tension σ can be related to the pressure P through the Young-Laplace law:

$$\int_{x_g}^{x_\ell} (\mathbf{\Sigma}_{xx} - \mathbf{\Sigma}_{yy}) dx = \Delta P = \frac{\sigma}{R} \tag{4.3}$$

where ΔP is the difference of pressure between the two regions and R is the radius of curvature. In equilibrium systems, phase separation is driven by the Ostwald ripening process: because the surface tension of a cluster of particles is positive, small clusters shrink at the advantage of large clusters, causing the system to evolve towards a complete phase separation. It therefore came as a surprise when in various particle-level simulations of PFAPs showing MIPS, the surface tension between the dense phase and the gas was measured to be negative [Bialké *et al.* 2015, Solon *et al.* 2018a, Patch *et al.* 2018].

This unexpected discovery subsequently lead to an argument on the very definition of pressure and surface tension for active systems. [Hermann *et al.* 2019] proposed an alternative definition of pressure which only considers forces deriving from potentials and hence recovered a positive surface tension. [Omar *et al.* 2020] investigated the effect of a stress tensor that balances the force density created by the polarization of the active particles and also found a positive surface tension. [Fausti *et al.* 2021] showed that capillary wave interfacial tension differs from the surface tension σ defined in Eq. (4.3), in constrast to the equilibrium case. More generally, these studies point towards the fact that the equilibrium surface tension controls several properties (e.g. capillary waves and the Laplace pressure) that, out-of-equilibrium, are in general controlled by different quantities.

The existence of a negative Laplace pressure was then rationalized at the field-theoretical level in [Tjhung *et al.* 2018], based on the introduction of an additional term in the Generalized Cahn-Hilliard (GCH) equation (4.1). The resulting new model, termed Active Model B+, was first introduced on the basis of symmetry considerations in [Nardini *et al.* 2017] and describes how the local density ϕ evolves in time. In addition to the GCH equation, AMB+ includes a term of the form $(\nabla^2\phi)\nabla\phi$ in the expression of the current, which then contains all terms that break time-reversal symmetry (TRS) at order $\mathcal{O}(\nabla^4)$:

$$\partial_t\phi = -\nabla\cdot(\mathbf{J}+\sqrt{2DM}\boldsymbol{\Lambda}), \tag{4.4}$$

$$\mathbf{J}/M = -\nabla\left[\frac{\delta\mathcal{F}}{\delta\phi}+\lambda|\nabla\phi|^2\right]+\zeta(\nabla^2\phi)\nabla\phi, \tag{4.5}$$

$$\mathcal{F}[\phi] = \int\left\{\frac{a}{2}\phi^2+\frac{b}{4}\phi^4+\frac{K}{2}|\nabla\phi|^2\right\}d\mathbf{r} \tag{4.6}$$

Eq. (4.4) describes the evolution of the conserved field ϕ in terms of the gradient of a current $\mathbf{J}$ supplemented by a Gaussian white noise with zero mean and unit variance $\boldsymbol{\Lambda}$. M is the mobility which may depend on the field but is usually considered constant, D is the temperature and $\mathcal{F}[\phi]$ is a standard equilibrium free-energy functional. As in the GCH equation, $\mathbf{J}$ does not derive from a free energy. It also contains the terms λ and ζ which are breaking TRS and cannot be written as the functional derivative of a free-energy. Their microscopic origin was later shown to emerge from explicit coarse-graining of the microscopic dynamics of PFAPs in [Tjhung *et al.* 2018].

Using AMB+, [Tjhung *et al.* 2018] considered a spherical droplet of radius R and showed, with the definition of the generalized pressure that it obeys Eq. (4.3) with a coefficient σ that can become negative for some values of the parameters (λ,ζ), as shown in Fig. 4.1a in zones B and C. Crucially, the presence of a negative tension does not cause the interface to become unstable. It however results in large droplets shrinking at the advantage of small ones in a process termed reverse Ostwald ripening. Going further, they obtained the time evolution of a droplet of radius $R(t)$ interacting with another droplet of size R_s:

$$\dot{R} = \frac{\beta}{R}\left[\frac{1}{R}-\frac{1}{R_s}\right] \tag{4.7}$$

where β is a parameter which can be related in a non-trivial way to σ. Importantly, $\beta>0$ when $\sigma<0$, so that Eq. (4.7) correctly predicts that the droplet of radius R will grow if $R_s>R$, in line with the reverse Ostwald ripening.

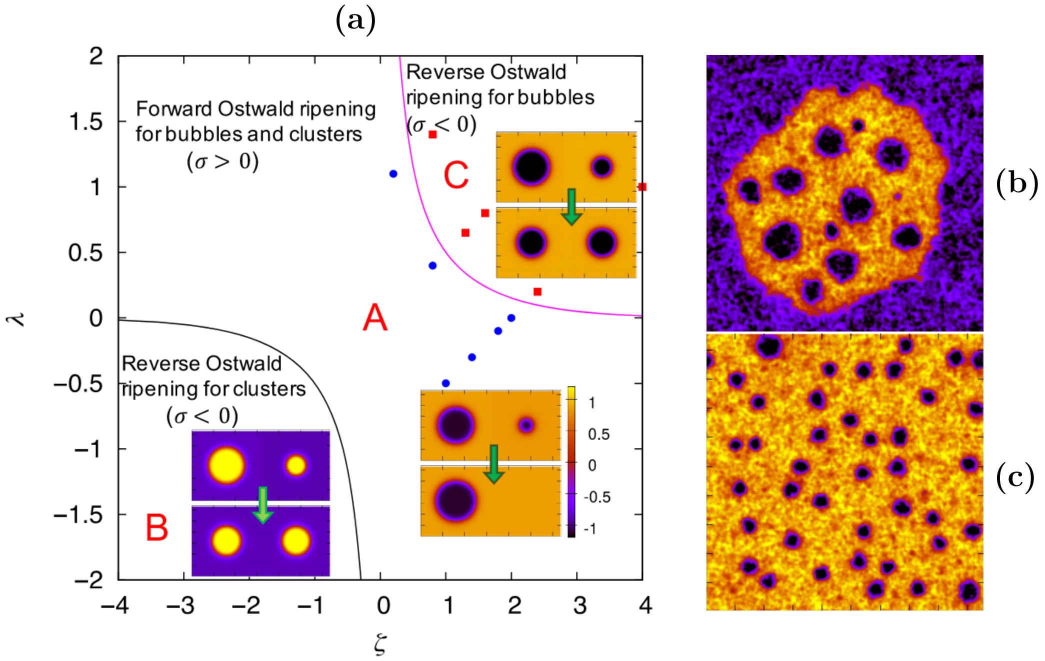

Figure 4.1: Phases in AMB+. Lighter colors indicate larger densities. **(a):** Mean-field (corresponding to $D = 0$ in Eq. (4.4)) phase diagram in the $\zeta - \lambda$ plane, showing that the surface tension σ is negative and triggers the reverse Ostwald ripening in zones B and C. In zone A, standard forward Ostwald ripening is recovered. Finite-size simulations of AMB+ in zone C showing bubbles in the phase coexistence **(b)** and microphase separation **(c)**. Adaptated from [Tjhung *et al.* 2018].

4.1.3 Bubbly phase separation

In contrast with the common phase separation observed in equilibrium systems, numerical simulations of AMB+ showed that the interplay between reverse Ostwald ripening and bubble coalescence leads to the coexistence of a dense phase populated by bubbles with an outer gas (Fig. 4.1b) or to a homogeneous bubbly microphase separation (Fig. 4.1c). In both cases, gas bubbles do exist in the liquid phase, even in stationary state.

Large-scale analysis of PFAPs exhibiting MIPS had previously shown the appearance of bubbles in the dense phase. In a model of ABP with short-range repulsive potential, [Stenhammar *et al.* 2014, Bialké *et al.* 2015] found "voids" forming within the bulk of the dense phase, as a result of large density fluctu-

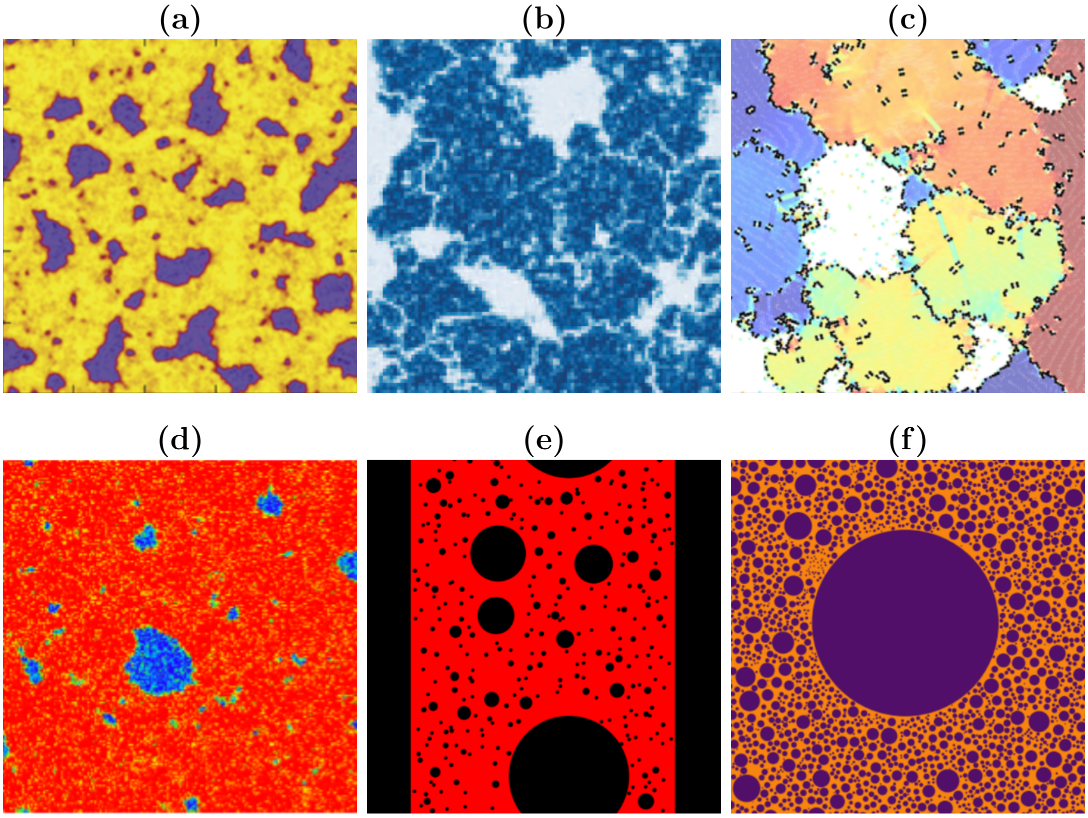

Figure 4.2: Bubbles in MIPS. **(a):** Simulations of $2d$ active Brownian particles showing bubbles (dark region) in the dense region (yellow) [Stenhammar *et al.* 2014]. **(b):** Dense region developping "holes" (white) [Bialké *et al.* 2015]. **(c):** Bubbles (white) forming within the mosaic of hexatic domains [Caporusso *et al.* 2020]. **(d):** Persistent bubbles (blue) with a range of sizes, surrounded by a liquid (red) [Shi *et al.* 2020] and **(e):** typical snapshot of the reduced Bubble model in phase coexistence, the black bands represent the gas reservoir. **(f):** Bubbly phase separation in the model of [Fausti 2021].

ations (Fig. 4.2a-b). More recently, [Digregorio *et al.* 2018] found gas defects within the mosaic of hexatic microdomains composing the MIPS phase at coexistence that [Caporusso *et al.* 2020], in light of the results stemming from the analysis of AMB+, interpreted as bubbles (Fig. 4.2c). They measured their radius of gyration and reported a scale-free distribution. Likewise, in two models of active particles interacting by pair-wise repulsion – an ABP-based model with repulsive interactions and a lattice gas –, [Shi *et al.* 2020] showed that the resulting dense phase contains gas bubbles (See Fig. 4.2d) distributed algebraically up to a typically large cutoff scale that grows with system size.

The scale-free distribution of bubble sizes seems to be a generic feature across models displaying the bubbly phase separation in MIPS. Quantitatively, the bubble areas a are approximately distributed as $P(a) \propto a^{-\alpha}$ with $\alpha \approx 1.6$ in [Caporusso *et al.* 2020, Digregorio *et al.* 2022], $\alpha \approx 1.75$ in both models of [Shi *et al.* 2020], and $\alpha \approx 1.4$ in a model of Repulsive Quorum-Sensing Active Particles by Shi *et al.* (unpublished). In simulations of AMB+, [Fausti 2021] estimated $\alpha = 1.5 \sim 2$, the precise value depending heavily on the noise amplitude.

In finite-size systems at low density, the bubbles coexist with a large gas reservoir, formed by the remaining dilute gas surrounding the dense phase. Increasing the density at fixed system size, more and more of the gas is contained in the bubbles. Above a critical density, the gas reservoir disappears and only the algebraic distribution remains, terminated by a density-dependent exponential cutoff, consistently with the homogeneous bubble phase reported in [Tjhung *et al.* 2018] (Fig. 4.1c).

[Shi *et al.* 2020] showed that the presence of a large reservoir is actually a finite-size effect. Increasing system size at fixed density, the cutoff bubble size a_c increases as $a_c \propto S^\gamma$ with a power $\gamma > 1$ of system size S. The total gas contained in the bubbles

$$a_{\text{bubbles}} = \int_0^{a_c} aP(a)da \propto S^{1+\gamma(2-\alpha)} \tag{4.8}$$

diverges with S since $\alpha < 2$. Therefore, since the total area of gas (bubbles + reservoir) is fixed, at large S the reservoir disappears and the cutoff a_c becomes independent of system size. All the gas is contained in the bubbles and we observe microphase separation. In the thermodynamic limit, the system thus displays three phases. At low density, only a dilute gas is observed. Increasing density, in the coexistence phase between gas and liquid, the system undergoes MIPS but the resulting dense phase contains bubbles in the form of a microphase separation. Finally, at high density, the system is in a liquid state.

4.1.4 Bubble models

Several minimal models implementing the basic idea of reverse Ostwald ripening were introduced to account for the phenomenology observed in the bubbly phase separation. [Shi *et al.* 2020] reduced the system to a collection of bubbles and presented a model where the bubbles are the degrees of freedom of the system. To take into account the reverse Ostwald scenario put forward in [Tjhung *et al.* 2018], they made the approximation that it can be modeled by nucleating small gas bubbles in the liquid at the expense of the larger ones, so that in practice large bubbles shrink at the advantage of small bubbles. All bubbles diffuse with a constant coefficient and, if the move brings bubbles into contact, they merge into a bubble located at their center of mass, conserving total area. Despite its simplicity, this model successfully reproduces both the bubbly phase separation (Fig. 4.2e) and the homogeneous bubble phase, along with exhibiting power-law distributions of bubble size with exponent $\alpha \approx 1.77$, terminated by a size-dependent cutoff with exponent $\gamma \approx 1.44$. A model of the same class is presented in [Fausti 2021], in which the reverse Ostwald ripening is introduced through the equilibration equation on the radius of each bubble in interaction with its nearest neighbour Eq. (4.7). A bubbly phase separation with algebraically distributed bubble sizes is observed (see Fig. 4.2f), albeit they do not report on the value of the decay exponent. All in all, the role of the various ingredients in these bubble models remains unclear. Furthermore, the question of the universality of the exponents has not been adressed.

In this Chapter, we investigate several models of aggregation and nucleation to account for the observed bubble dynamics. We find that they generically feature scale-free distributions in stationary state. In Sec. 4.2, we introduce two classes of bubble models in $1d$, $2d$ and $3d$. In the Aggregation-Nucleation Model (ANM) presented in Sec. 4.2.1, bubbles are point-like and evolve on a lattice. The system displays algebraic distributions of bubble sizes with an exponent $\alpha = 5/2$, a system-size dependent exponential cutoff that we compute analytically and a gas reservoir. In Sec. 4.2.2, we present a mean-field description of the ANM that we solve using a mapping to a chipping model introduced in [Krapivsky *et al.* 2010]. This allows to compute the phase diagram and an explicit solution. Consistently, we also find an algebraic asymptotic behaviour with exponent $\alpha = 5/2$. In the Reduced Bubble Model (RBM) introduced in Sec. 4.2.3, we add a new ingredient by taking into account the spatial extension of bubbles. We report an algebraic de-

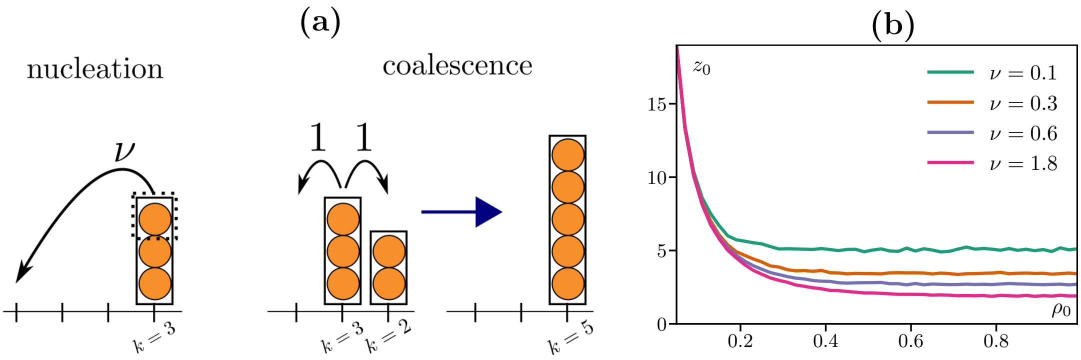

Figure 4.3: Definition of the Aggregation-Nucleation Model (ANM). **(a):** Sketch of the two possible actions in the ANM and their rates of occurrence. **(b):** Mean distance to the closest non-empty site in the 1d ANM as a function of the density of gas ρ_0. Parameters: $L = 1000$.

cay with exponent compatible with the value $\alpha = 5/2$. Importantly, the measured value of this exponent is greater than 2 so that, as detailed earlier in Sec. 4.1.3, the asymptotic phase diagrams of these models differ qualitatively from those of MIPS. Supplementing the models with a bubble size-dependent diffusion in Sec. 4.3, we find on the contrary that the scaling exponent α can be smaller than 2, thus changing the nature of finite size effects (Sec. 4.3.1). We compare the mean-field prediction with the ANM in Sec. 4.3.2 and the RBM in Sec. 4.3.3, through an analysis of the reservoir dynamics. Finally, coming back to MIPS phenomenology in Sec. 4.4, we argue in favor of a homogeneous reversed Ostwald ripening by analyzing the influence of neglecting spatial effects in the nucleation process of the models.

4.2 Bubble dynamics

4.2.1 Aggregation-Nucleation Model

The Aggregation-Nucleation Model (ANM) is a minimal model in which bubbles constitute the degree of freedom of the system and are assumed to have no spatial extension. They move on a d-dimensional hypercubic lattice of linear size L with periodic boundary conditions. Each bubble carries its discrete gas volume k as a dynamic variable. The total density of gas ρ_0 is fixed by initially distributing bubbles on the lattice so that their total volume is equal to ρ_0. Bubbles jump at unit rate on a neighbouring lattice site. If the target site is occupied, the bubbles coalesce conserving the total gas volume. Moreover, any vacant site can nucleate a unit bubble (*i.e.* of volume 1) with rate ν by extracting it from the nearest non-empty site (See Fig. 4.3a for a sketch of these actions). This is a simple way to model the reverse Ostwald scenario, as it creates small bubbles by shrinking larger ones. Note that the nucleation process is local in the sense that the extracted gas volume is as close as possible to the nucleating site. In practice, the closest non-empty site is found to be at a mean distance z_0 that depends on ν and ρ_0 as shown in Fig. 4.3b but not on system size. We z_0 to be smaller than 20 for typical values of parameters, confirming that the nucleation process remains local. In the rest of the chapter, we study the system as a function of ρ_0 and ν.

Looking at the phase diagram in 1d and 2d on Fig. 4.4a, we report two phases. At low gas density and high nucleation rate, the bubble sizes are algebraically distributed with an exponent $\alpha = 5/2$ and an exponential cutoff at a maximal bubble size k_c independent of system size (See Fig. 4.4b, in purple and red). In Fig. 4.4c, we present a typical snapshot in this phase, each line corresponding to the volume k of the bubble located on the site. Increasing density or decreasing nucleation rate, the exponential cutoff moves towards larger values of bubble sizes k, until it reaches a critical value above which a macroscopic aggregate develops, as shown by the peak in Fig. 4.4d, coexisting with a background low-density phase, distributed as a power-law with the same exponent α (See Fig. 4.4b, orange and blue). This macroscopic aggregate is analogous to the gas reservoir in microscopic simulations displaying MIPS. To distinguish between the two phases, we estimated the value of ρ_0 above which a peak develops (yellow and green dots on Fig. 4.4a) using the scaling of its size with density. The transition lines in 1d and 2d are in qualitative, though not quantitative, agreement.

A model of the same type was investigated in [Rajesh & Majumdar 2001]. They studied a chipping model in which masses diffuse and unit masses are chipped off at a constant rate from piles of particles and placed on an adjacent site. Apart from the interpretation of bubbles as piles of particles, the two models differ only because nucleation in our model happens on empty sites, possibly at a distance from the nearest occupied site. Consistently with the phenomenology of our model, they found a phase transition from a phase without aggregate to a phase with aggregate. The aggregate coexists with a dilute background consisting of masses

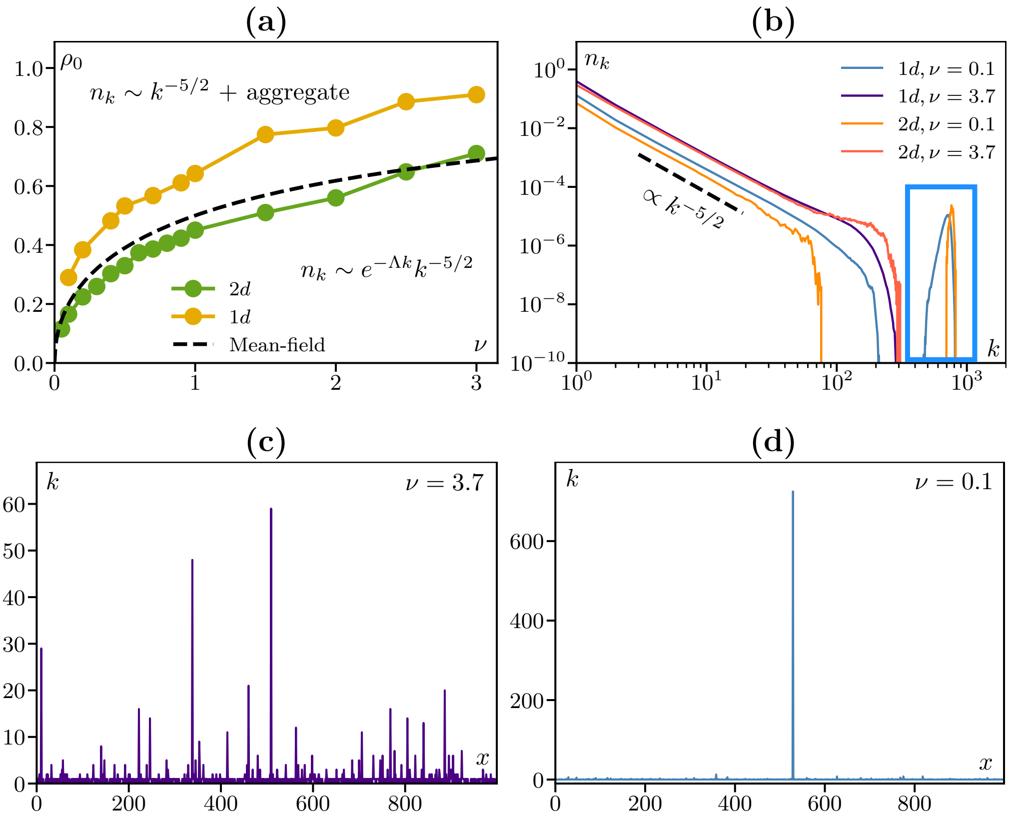

Figure 4.4: Phases of the ANM. **(a):** Comparison of the phase diagram in the ρ_0–ν plane for the ANM in 1d and 2d with the mean-field prediction Eq. (4.23). **(b):** Distributions obtain in 1d and 2d, displaying an algebraic $k^{-5/2}$ decay, terminated by a cutoff with an additional peak (blue square) in the coexistence phase ($\nu = 0.1$), analogous of the gas reservoir in microscopic simulations. **(c):** Typical profile of bubble sizes in simulations in the exponential phase. **(d):** Typical profile of bubble sizes in simulations in the aggregate phase. Parameters: $L = 1024$ (1d), $S = 32 \times 32$ (2d); $\rho_0 = 1$ (1d), $\rho_0 = 0.9$ (2d).

which sizes are power-law distributed with the same exponent $\alpha = 5/2$ that we observe. By analyzing two-point equal time correlation functions, they obtained the expression of the transition line without resorting to the mean-field approximation and showed it to be independent of the dimension of space. In our case, the phases have the same phenomenology but the phase diagram, shown in Fig. 4.4a, depends on the dimension of space which must reflect the fact that the exact relations between correlation functions uncovered by [Rajesh & Majumdar 2001] are

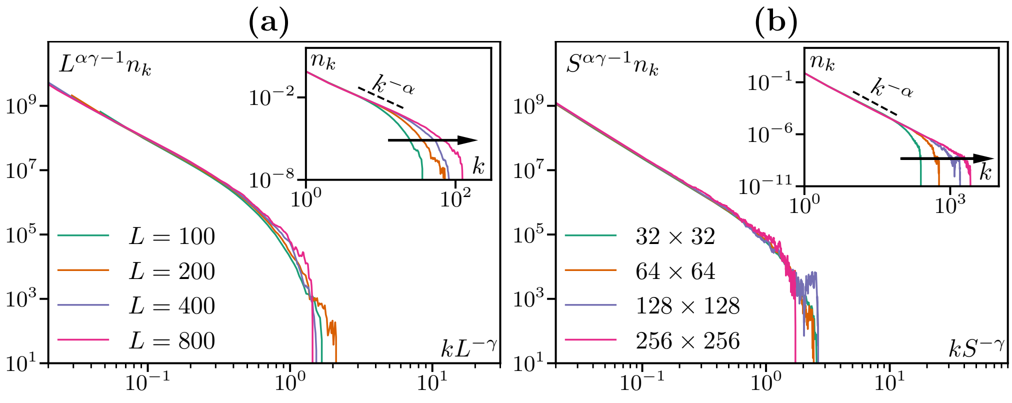

Figure 4.5: Pile size distributions at various system sizes in the Aggregation-Nucleation Model. **(a):** $1d$ simulations, showing the curves collapsing on a master curve for the predicted mean-field exponents $\alpha = 5/2$ and $\gamma = 2/3$. Inset: without rescaling. The black arrow emphasizes the shift $k_c \sim V^\gamma$. **(b):** Same as (a) in the $2d$ case. Parameters: $\rho_0 = 1$ (a), $\rho_0 = 0.9$ (b); $\nu = 10^{-2}$ (a), $\nu = 0.5$ (b).

not obeyed with our update rules.

We look in more details at finite-size effects in the ANM. In a finite system, at high density or small ν, the aggregate coexists with bubbles algebraically distributed upto an exponential cutoff k_c which shifts with system size, as indicated by the black arrow in the insets of Fig. 4.5.

Introducing the scaling exponent γ such that the cutoff scales as $k_c \sim V^\gamma$, we show how it can be computed. We denote k_p the size of the aggregate. Although it is contained on a single site (Fig. 4.4d), it is extensive: $k_p \propto V$. The size distribution can thus, as in [Rajesh *et al.* 2002], be written

$$n_k = k^{-\alpha} f\left(\frac{k}{k_c}\right) + \frac{1}{V}\delta(k - k_p) \tag{4.9}$$

where n_k is the mean fraction of lattice sites occupied by bubbles of size k and $f(\cdot)$ is a scaling function exponentially decaying at large argument. Since we work at large system sizes, we treat k as a continuous variable. Enforcing the normalization constraint

$$\int_0^{+\infty} n_k dk = 1 \tag{4.10}$$

leads to

$$\int_0^{+\infty} \left[k^{-\alpha} f\left(\frac{k}{V^\gamma}\right) + \frac{1}{V}\delta(k - k_p) \right] dk = 1. \tag{4.11}$$

Taking the derivative with respect to V followed by a proper change of variable, we obtain

$$\gamma(1-\alpha)V^{\gamma(1-\alpha)-1} \int_0^{+\infty} u^{-\alpha} f'(u) du = V^{-2} \tag{4.12}$$

Since the integral does not depend on V, requiring consistency of the exponents in the limit $V \to \infty$ yields:

$$\gamma(\alpha - 1) = 1 \tag{4.13}$$

Using the exponent $\alpha = 5/2$ measured in simulations of the ANM (See Fig. 4.4b) gives $\gamma = 2/3$. We test this prediction by dividing the bubble sizes k by V^γ, with $\gamma = 2/3$, as shown in Fig. 4.5. This collapses reasonably well the distributions obtained for several values of V[1].

When $V \to \infty$, both k_c and k_p diverge but $k_c \sim V^\gamma$ with $\gamma < 1$ diverges slower than $k_p \sim V$. In the thermodynamic limit, the coexistence thus persists. This is consistent with the fact that the fraction of the gas volume contained in bubbles (excluding the aggregate)

$$\rho_b = \sum_{k=0}^{k_c} k\, n_k, \tag{4.14}$$

converges to a finite value as $k_c \to \infty$. Decreasing the density, the transition to the microphase separated state happens when $\rho_0 = \rho_b$ at which point the aggregate disappears. This is in stark contrast with microscopic systems that have $\alpha < 2$ so that ρ_b diverges with system size and we always observe the microphase separation in the system.

4.2.2 Mean-field description

We now present a mean-field description of the ANM. Bubbles of discrete gas volume aggregate at unit rate with another bubble, combining their gas into a single bubble. The density of bubbles of volume k is denoted $n_k(t)$ and we introduce

---

[1] Note that to keep the distributions normalized with respect to the new argument $kV^{-\gamma}$, we also multiply n_k by $V^{\alpha\gamma-1}$.

$\varphi(t) = \sum_{k=1}^{+\infty} n_k(t)$ the total bubble density, $1-\varphi$ thus representing the fraction of empty space. Since in the ANM bubbles of unit volume are nucleated on empty sites, the nucleation process occurs at a rate proportional to the fraction of empty sites $1-\varphi$: With rate $\nu(1-\varphi)$, a unit gas volume can detach from its bubble to generate a bubble of unit size. The system contains a mean density ρ_0.

In order to write the master equation for the dynamics of n_k, we first assume the system to be well-mixed, so that we can make the mean-field approximation $\langle n_i n_j \rangle = \langle n_i \rangle \langle n_j \rangle$ and remove the averages to write $n_i = \langle n_i \rangle$. We now write the governing equations for n_k:

$$\partial_t n_k = \frac{1}{2}\sum_{i=1}^{k-1} n_{k-i} n_i - n_k \sum_{i=1}^{+\infty} n_i + \nu(1-\varphi)\delta_{1,k} + \frac{\nu(1-\varphi)}{\varphi}(n_{k+1} - n_k) \tag{4.15}$$

The first term corresponds to the aggregation of two bubbles of sizes $k-i$ and i to form a resulting bubble of size k. The prefactor $1/2$ avoids double-counting. The second term is the aggregation of a bubble of size k with any other bubble. The third and last terms account for nucleation: bubbles of unit size form at the expense of the other bubbles.

The total density $\varphi(t)$ of bubbles is then subject to the following evolution:

$$\partial_t \varphi = -\frac{1}{2}\left(\sum_{i=1}^{+\infty} n_i\right)^2 + \nu(1-\varphi) - \frac{\nu(1-\varphi)}{\varphi} n_1 \tag{4.16}$$

This model can be mapped in stationary state onto a chipping model introduced and solved in [Krapivsky *et al.* 2010] by a change of variable [2]. We now follow their method and introduce the generating function

$$\mathcal{C}(z,t) = \sum_{k=1}^{+\infty} n_k z^k \tag{4.17}$$

to recast the infinite system Eqs. (4.15, 4.16) into

$$\partial_t(\mathcal{C}-\varphi) = \frac{1}{2}(\mathcal{C}-\varphi)^2 - \frac{\nu(1-\varphi)}{\varphi}(\mathcal{C}-\varphi)(1-\frac{1}{z}) + \frac{\nu(1-\varphi)}{\varphi}\varphi\frac{(1-z)^2}{z}. \tag{4.18}$$

---

[2] $\nu(1-\varphi)/\varphi = \lambda$, using their notation.

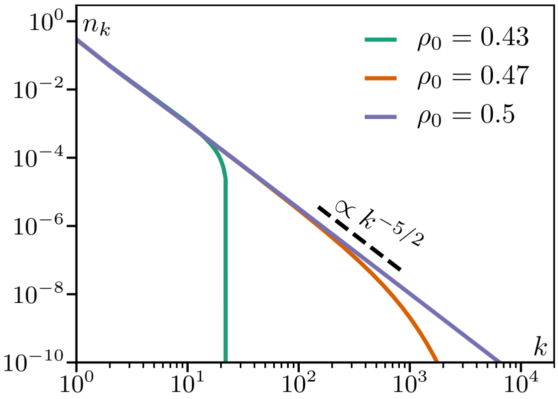

Figure 4.6: Plots of the analytical solution Eq. (4.24) below ρ_0^c and at $\rho_0^c = 0.5$ for $\nu = 1$.

Eq. (4.18) implies that, in stationary state, the function $\mathcal{Z} = \mathcal{C} - \varphi$ is solution of a quadratic equation and admits the following expression:

$$\mathcal{Z} = \frac{\nu(1-\varphi)}{\varphi}(1-z^{-1})\left(1-\sqrt{1-\frac{2\varphi^2 z}{\nu(1-\varphi)}}\right). \tag{4.19}$$

The value of φ is readily obtained by differentiating Eq. (4.19) with respect to z and setting $z = 1$. Indeed, the density ρ_0 must be equal to the total gas volume contained in the bubbles:

$$\rho_0 = \sum_{k=1}^{+\infty} k n_k = \left.\frac{d\mathcal{Z}}{dz}\right|_{z=1} = \frac{\nu(1-\varphi)}{\varphi}\left(1-\sqrt{1-\frac{2\varphi^2}{\nu(1-\varphi)}}\right) \tag{4.20}$$

At high enough ν, when $2\varphi^2 \leq \nu(1-\varphi)$, the solution reads

$$\varphi = \frac{1}{2}\left(1+\rho_0+\frac{\rho_0^2}{2\nu}\right)\left(1+\sqrt{1-\frac{4\rho_0}{(1+\rho_0+\rho_0^2/(2\nu))^2}}\right) \tag{4.21}$$

In the case $2\varphi^2 > \nu(1-\varphi)$, Eq. (4.20) has no real solution. This happens when φ reaches the critical value φ_c such that $2\varphi_c^2 = \nu(1-\varphi_c)$ and it indicates that the total gas of the system cannot be contained in the n_k. Increasing the density ρ_0, φ saturates at $\varphi = \varphi_c$ and the excess density is accommodated in an aggregate that contains a fraction m_p of the gas of the system such that

$$\rho_0 = \varphi_c + m_p \tag{4.22}$$

Similarly to earlier works on condensation [Evans & Hanney 2005], the phase boundary separating the regime with an infinite aggregate and without it is obtained when the volume of the aggregate vanishes. Setting $m_p = 0$ in Eq. (4.22), we obtain

$$\rho_0^c = \varphi_c = -\frac{\nu}{4} + \frac{1}{4}\sqrt{\nu + 8\nu^2} \tag{4.23}$$

This allows to draw the phase diagram presented in Fig. 4.4a.

The complete distribution can be obtained by expanding Eq. (4.19) in powers of z to identify the n_k using the definition of $\mathcal{C}(z)$ (Eq. (4.17)). This procedure leads to:

$$n_k = \frac{\nu(1-\varphi)}{\varphi}(-1)^{k+1}\left(\frac{2\varphi^2}{\nu(1-\varphi)}\right)^k \left[\binom{1/2}{k} + \frac{2\varphi^2}{\nu(1-\varphi)}\binom{1/2}{k+1}\right] \tag{4.24}$$

We now focus on the asymptotic behaviour of the distribution n_k at large k. We find two distinct regimes in the two phases:

$$n_k \sim \begin{cases} e^{-\Lambda k}\left[\phi_1 k^{-3/2} + \phi_2 k^{-5/2}\right], & \rho_0 < \rho_0^c \\ \\ \dfrac{3\nu(1-\varphi)}{4\sqrt{\pi}\varphi} k^{-5/2} + \text{aggregate}, & \rho_0 \geq \rho_0^c \end{cases} \tag{4.25}$$

where $\Lambda = \ln\left[\dfrac{(1-\varphi)\nu}{2\varphi^2}\right]$ is an exponential cutoff,

$$\phi_1 = \frac{\nu(1-\varphi) - 2\varphi^2}{2\sqrt{\pi}\varphi}, \tag{4.26}$$

$$\text{and} \quad \phi_2 = \frac{3\left(\nu(1-\varphi) + 6\varphi^2\right)}{16\sqrt{\pi}\varphi} \tag{4.27}$$

At low density $\rho_0 < \rho_0^c$, Eq. (4.25) seems to indicate that the leading behaviour is an algebraic $k^{-3/2}$ decay cut-off by the exponential prefactor for $k > \Lambda^{-1}$, as was reported in [Krapivsky *et al.* 2010]. However, plotting the solution in this regime (see Fig. 4.6b) we only observe a $k^{-5/2}$ decay. To explain this, we compute the crossover value k^* between the $k^{-3/2}$ and $k^{-5/2}$ regimes in Eq. (4.25), defined as

$$\phi_1 k^{*-3/2} = \phi_2 k^{*-5/2} \tag{4.28}$$

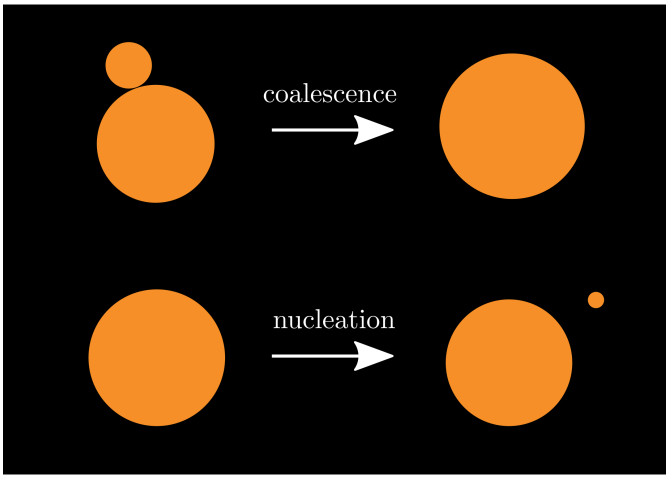

Figure 4.7: Sketch of the two possible actions in the RBM.

Using the expressions of ϕ_1 and ϕ_2 of Eq. (4.26) and Eq. (4.27), this yields

$$k^* = \frac{3}{8}\frac{6\varphi^2 + \nu(1-\varphi)}{\nu(1-\varphi) - 2\varphi^2} = \frac{3}{8}\frac{e^\Lambda + 3}{e^\Lambda - 1} \tag{4.29}$$

A straightforward analysis of the function $x \mapsto \frac{3}{8}\frac{e^x + 3}{e^x - 1} - \frac{1}{x}$ allows to conclude that $k^* > \Lambda^{-1}$ so that the exponential cutoff always occurs before the $k^{-3/2}$ regime, leaving the dominant $k^{-5/2}$ decay as the only algebraic decay observable. Increasing ρ_0, $\varphi \to \varphi_c$ and the cutoff Λ^{-1} is sent to $+\infty$, so that in the aggregate phase ($\rho_0 \geq \rho_0^c$), the distribution is algebraic with a decay exponent $\alpha = 5/2$.

Our mean-field model is thus able to predict the correct value of the exponent α observed in the ANM. As we will see in the next section, the value of this exponent seems to be a common features of our models. We now turn to a more realistic model of bubbles.

4.2.3 Reduced Bubble Model

In the Reduced Bubble Model (RBM), we add a new ingredient by considering the spatial occupation of bubbles. To do this, we introduce a model in which bubbles are spherical of radius r and evolve in continuous periodic space of dimension $d \in \{1, 2, 3\}$ and of linear size L. Their behaviour is summarized in Fig. 4.7. As

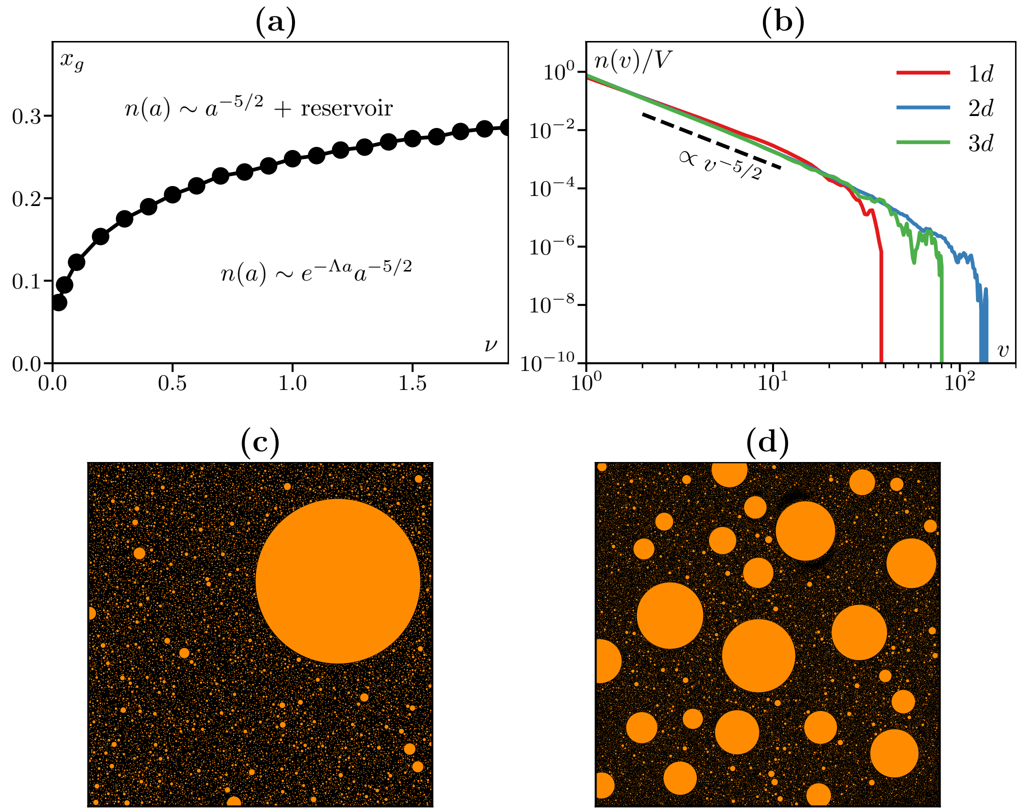

Figure 4.8: Phases of the RBM. **(a):** Phase diagram in the $\rho_0 - \nu$ plane in $2d$ for system size 50×50. **(b):** Bubble sizes distributions obtain in $1d$ ($L = 8000$), $2d$ ($S = 800 \times 800$) and $3d$ ($V = 100 \times 100 \times 100$), displaying an algebraic $k^{-5/2}$ decay, terminated by a cutoff (reservoir not shown). **(c):** Typical snapshot of the RBM in $2d$ in the reservoir phase and in the exponential phase **(d)**. Parameters: $x_g = 0.3$ ($1d$, $2d$), $x_g = 0.2$ ($3d$); $\nu = 10^{-4}$ ($1d$, $2d$), $\nu = 10^{-3}$ ($3d$).

before, bubbles diffuse at constant unit rate. When two bubbles touch each other, they merge into a bubble of volume equal to that of the two initial bubbles that is placed at the center of mass, thus conserving the total bubble volume. Small bubbles of radius $r_0 = 1$ are nucleated in the empty space at rate ν per unit volume. The reverse Ostwald scenario is taken into account in the following way: the newly formed bubbles are nucleated by extracting their volume from the closest bubble of radius r_n with a probability $1 - r_0/r_n$, so that large bubbles shrink with probability 1 at the advantage of small bubbles. All the rules conserve the volume,

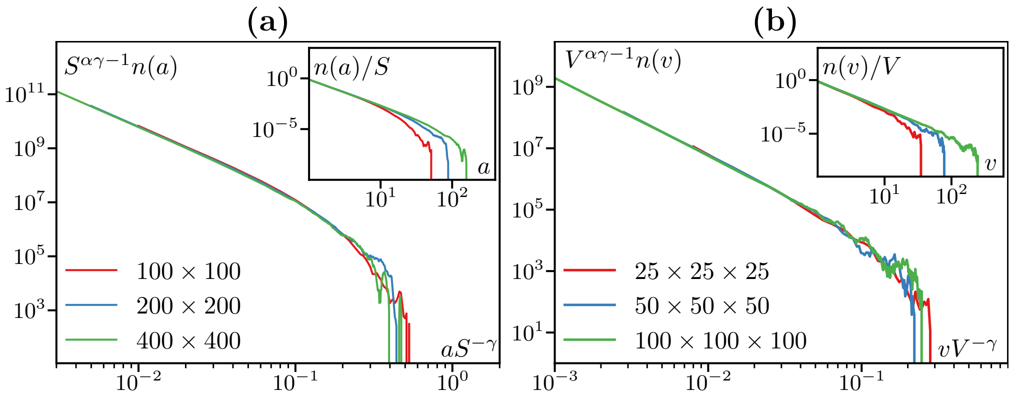

Figure 4.9: Bubble size distributions at various system sizes in the Reduced Bubble Model. **(a):** $2d$ simulations, showing the curves collapsing on a master curve for the exponents $\alpha = 5/2$ and $\gamma = 1/2$. Insets: without rescaling. **(b):** Same as (a) in the 3d case. Parameters: $\rho_0 = 1$ (a), $\rho_0 = 0.9$ (b); $\nu = 10^{-3}$ (a), $\nu = 10^{-2}$ (b).

so that the fraction x_g of gas is fixed. Initially, we seed the system with bubbles of unit radius randomly distributed in space.

Consistently with the previously presented models, the phase diagram, computed in $2d$, displays two regions (See Fig. 4.8a). At high gas fraction, the gas is contained in a macroscopic bubble surrounded by a sea of small bubbles (See Fig. 4.8c). Decreasing the gas fraction, the reservoir disappears and the gas is only contained in bubbles (See Fig. 4.8d). Computing the probability distributions of the bubbles' volume v for $d \in \{1, 2, 3\}$, we again find scale-free distributions terminated by a system-size dependent cutoff (Fig. 4.8b), with an algebraic exponent α compatible with the value $\alpha = 5/2$ predicted by the mean-field theory, in both phases.

As before in the ANM, computing the bubble size distributions at various system sizes, we observe a shift of the exponential cutoff. Bubbles have a physical size so we expect the previous hyperscaling relation Eq. (4.13) to fail predicting the correct value of the exponent γ in this case. Instead, rescaling bubble sizes by a power of the system size V^γ in dimensions 2 and 3, we find the distributions to collapse for $\gamma \approx 1/2$ both in $2d$ and in $3d$ (Fig. 4.9, main figures).

4.2.4 Fluctuations of the reservoir

As reported above, both the ANM and the RBM have a phase in which a reservoir of extensive size V_{res} coexists with bubbles of sizes distributed like a power-law of exponent α terminated by an exponential cutoff diverging with system size. We now consider the finite-size scaling of the reservoir's fluctuations in d dimensions. The nucleation process decreases at constant rate the size of the reservoir by an amount of order 1 so that in a time of order V_{res}, with $V_{\text{res}} \propto V$, all the gas of the reservoir is renewed. In contrast, in the same duration $\sim V$, the reservoir undergoes M_c collisions at constant rate, so that $M_c \sim V$. Each collision with a bubble increases the size of the reservoir by a quantity which typically scales with system size. We thus disregard the contribution of nucleations in our analysis of the reservoir's fluctuations. After a large number M_c of collisions with the surrounding bubbles, the size v_{res} fluctuates as the sum of M_c random variables drawn from a power-law distribution of exponent α with a cutoff, given in [Bouchaud & Georges 1990] by

$$\langle {V_{\text{res}}}^2 \rangle - \langle V_{\text{res}} \rangle^2 \sim M_c^{\frac{2}{\alpha-1}} \tag{4.30}$$

Since $M_c \sim V$, we obtain a prediction for the scaling of the reservoir fluctuations with system size:

$$\sqrt{\langle {V_{\text{res}}}^2 \rangle - \langle V_{\text{res}} \rangle^2} \sim V^{\frac{1}{\alpha-1}} \tag{4.31}$$

To test Eq. (4.31), we measure the reservoir size fluctuations in stationary state in the ANM (See Fig. 4.10a) and in the RBM (See Fig. 4.10b) as a function of system size. We observe good agreement with the predicted scaling. Note that in the ANM, the fluctuation amplitude of the reservoir is of the same order as the largest bubble size since $1/(\alpha - 1) = \gamma$, while in the RBM it is larger.

To conclude, we investigated two models of bubbles containing aggregation and nucleation in varying spatial dimension. We found the distributions of bubble sizes to be algebraic with a cutoff in all considered dimensions, with a decay exponent α compatible with the value predicted by mean-field theory. We explored the finite-size scaling of the reservoir and showed that it persists in the thermodynamic limit, as expected because $\alpha > 2$.

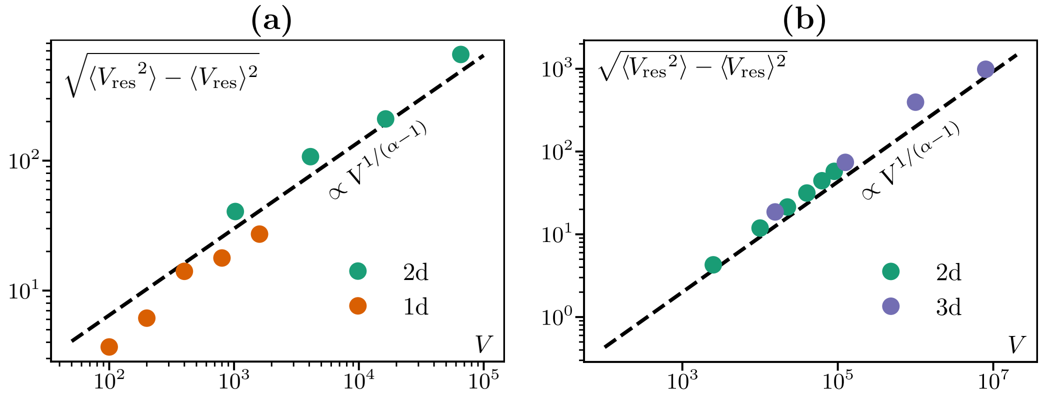

Figure 4.10: Fluctuations of the reservoir as a function of system size for the ANM (a) and the RBM (b), compared with the predicted scaling Eq. (4.31) (black dashed lines), with $\alpha = 5/2$. **(a):** Parameters: $\rho_0 = 1$ (1d), $\rho_0 = 0.9$ (2d); $\nu = 10^{-2}$ (1d), $\nu = 0.5$ (2d). **(b):** Parameters: $x_g = 0.7$, $\nu = 10^{-3}$.

4.3 Volume-dependent diffusion

Up to now, we have used the approximation that bubbles diffuse at constant unit rate. By contrast, in the well-studied case of equilibrium diffusion, the diffusion constant of a spherical drop of one fluid in another of similar viscosity is proportional to the inverse radius of the drop [Siggia 1979] *i.e.* to its volume to the power $-1/3$. Other diffusion processes can lead to a different scaling of the diffusion coefficient with the cluster size. For instance, in the mechanism of island diffusion, atoms diffuse freely in d-dimensions and aggregate to form islands which in turn diffuse. As computed in [Krapivsky *et al.* 1999], the diffusion of such an island is proportional to its volume to the power $-(d+1)/d$. More recently, measures of the displacement of active clusters of particles in MIPS [Caporusso *et al.* 2022] were shown to undergo enhanced diffusion proportional to their volume to the power $-1/2$. Finally, following bubbles in the lattice model of [Shi *et al.* 2020] and measuring their diffusion rate as a function of their size, it was observed that the diffusion is not a constant with respect to bubble size. They found that it scales as their volume to an exponent between -0.8 and -1 [unpublished results of Shi *et al.*].

To take this into account in the bubble models, we make the generic assumption that bubbles diffuse proportionnaly to a power $-\sigma$ of their volume, where $\sigma > 0$

is called *diffusion exponent*. Qualitatively, this means that small bubbles diffuse more rapidly than large ones. Instead of diffusing at a constant unit rate, bubbles of size k diffuse with a coefficient $D(k) = D_0 k^{-\sigma}$ in the Aggregation-Nucleation Model. Similarly, for the Reduced Bubble Model, a bubble of area a diffuses with a coefficient $D(a) = D_0 a^{-\sigma}$. We choose $D_0 = 1$ without loss of generality in the following.

4.3.1 Mean-field model

We first examine the consequences of a volume-dependent diffusion in the context of the mean-field model presented in Sec. 4.2.2. In practice, endowing the bubbles with a volume-dependent diffusion translates into a modification of their aggregation rate, because the interaction between two bubbles now depends on their respective sizes. The expression of the diffusion suggests that the aggregation kernel can take a similar form, involving powers of the bubble sizes. We thus choose a reaction rate of two bubbles of size i and j to be of the form:

$$K_{ij} = i^{-\omega} + j^{-\omega} \tag{4.32}$$

where $\omega > 0$ is the aggregation exponent. With this new kernel, the set of master equations of the n_k reads:

$$\begin{aligned}\partial_t n_k =& \frac{1}{2}\sum_{i=1}^{k-1}((k-i)^{-\omega} + i^{-\omega}) n_{k-i} n_i - n_k \sum_{i=1}^{+\infty}(k^{-\omega} + i^{-\omega}) n_i \\ &+ \frac{\nu(1-\varphi)}{\varphi}(n_{k+1} - n_k) + \nu(1-\varphi)\delta_{1,k}\end{aligned} \tag{4.33}$$

$$\partial_t \varphi = -\frac{1}{2}\sum_{i=1}^{+\infty}\sum_{j=1}^{+\infty}(i^{-\omega} + j^{-\omega}) n_i n_j + \nu(1-\varphi) - \frac{\nu(1-\varphi)}{\varphi} n_1 \tag{4.34}$$

Eq. (4.33) is the same as Eq. (4.15), albeit with a different aggregation kernel. Because the system displays an algebraic decay of the n_k when $\omega = 0$ (cf. Sec. 4.2.2), it is reasonable to assume that this decay holds when $\omega \neq 0$. That is, we want to find the algebraic decay exponent α as a function of ω.

Contrary to Eq. (4.15), Eq. (4.33) now features terms of the form $i^{-\omega} n_i$ in addition to the former n_i. This makes the use of the previous generating function

Eq. (4.17) inconvenient. Instead, we follow [Rajesh *et al.* 2002] and introduce two generating functions[3]

$$\mathcal{C}(p)=\sum_{k=1}^{+\infty} n_k e^{-pk} \quad \text{and} \quad \mathcal{A}(p)=\sum_{k=1}^{+\infty} n_k k^{-\omega} e^{-pk} \tag{4.35}$$

In stationary state, we recast Eq. (4.33) into:

$$0=\mathcal{A}\mathcal{C}-\mathcal{A}\varphi-M\mathcal{C}+\mathcal{C}\frac{\nu(1-\varphi)}{\varphi}(e^p-1)-\nu(1-\varphi)+\varphi A+e^{-p}\nu(1-\varphi) \tag{4.36}$$

Where $\varphi=\mathcal{C}(0)$ and $A=\mathcal{A}(0)$, and we have used Eq. (4.34) to express n_1 as a function of φ. Eq. (4.36) is the analogous of Eq. (4.18) in the presence of volume-dependent diffusion in stationary-state. It reduces to the later taking the limit $\omega \to 0$ and performing the changes of variable $z=e^{-p}$ and $\nu \leftarrow 2\nu$. Contrary to Eq. (4.18), we cannot solve Eq. (4.36) explicitly. To extract asymptotic behaviours we look at the moments $\langle k^x \rangle$ of the distribution of the n_k, where

$$\langle k^x \rangle=\sum_{k=1}^{+\infty} k^x n_k \tag{4.37}$$

To do this, we first expand the exponential in the expression of $\mathcal{A}$ and $\mathcal{C}$ (Eq. (4.35)) and write them as series involving the moments $\langle k^x \rangle$:

$$\mathcal{C}(p)=\sum_{n=0}^{+\infty}\langle k^n \rangle \frac{(-p)^n}{n!} \text{ and } \mathcal{A}(p)=\sum_{n=0}^{+\infty}\langle k^{n-\omega} \rangle \frac{(-p)^n}{n!} \tag{4.38}$$

Plugging these expressions in Eq. (4.36) and taking the limit $p \to 0$, we identify the various powers of p. At order p^1, we find:

$$\langle k \rangle \langle k^{1-\omega} \rangle=\nu(1-\varphi)\left(\frac{\langle k \rangle}{\varphi}-1\right) \tag{4.39}$$

Note that taking the limit $\omega \to 0$ and identifying $\langle k \rangle$ with ρ_0, the previous equation reduces to Eq. (4.20). It can thus be interpreted as an equation stating the conservation of density. At order p^2, using the previous expression of $\langle k^{1-\omega} \rangle$, we obtain:

$$\langle k \rangle^2 \langle k^{2-\omega} \rangle=\langle k^2 \rangle \nu(1-\varphi)-\langle k \rangle^2 \frac{\nu(1-\varphi)}{\varphi} \tag{4.40}$$

---

[3] Note that $\mathcal{C}(p)$ is the same definition as Eq. (4.17) upto the change of variable $z=e^{-p}$.

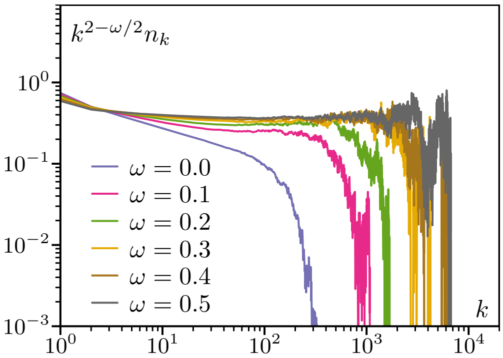

Figure 4.11: Distribution of sizes obtained by Monte-Carlo simulations of Eq. (4.33), multiplied by $k^{2-\omega/2}$ to highlight their algebraic exponent smaller than 2 for $\omega > 0$. Parameters : $L = 20000$, $\rho_0 = 1$, $\nu = 10^{-3}$.

We now wish to explicit the scaling of the moments $\langle k^x \rangle$ with density ρ_0. This requires writing a scaling form for the n_k in the large ρ_0 limit. In the $\omega = 0$ case, $\alpha = 5/2 > 2$ implies that the total volume contained in the bubbles, namely $M = \sum_{k=1}^{+\infty} k\, n_k$, converges. On the contrary, looking at the distributions obtained by simulation[4] of Eq. (4.33), we observe an exponent $\alpha < 2$ (See Fig. 4.11). As already mentioned, in this case, the total volume contained in the bubbles diverges in the thermodynamic limit, so that all the gas is contained in the distribution. Therefore, the macroscopic aggregate volume vanishes in the thermodynamic limit and we cannot reuse the scaling form Eq. (4.9): the system displays an algebraic decay terminated by an exponential cutoff k_c which depends on *density*: $k_c \sim \rho_0^{\phi}$. In line with this observation, we write the following scaling form, treating k as a continuous variable in the thermodynamic limit:

$$n_k = k^{-\alpha} g_\omega \left(\frac{k}{k_c} \right) \tag{4.41}$$

where g_ω is a scaling function with an exponential decay for large arguments. This allows to obtain an expression for the scaling of the moments with density:

$$\langle k^x \rangle = \int_0^{+\infty} k^x n_k dk = \int_0^{+\infty} k^{x-\alpha} g_\omega \left(\frac{k}{\rho_0^{\phi}} \right) dk \underset{\rho_0 \to \infty}{\sim} \rho_0^{\phi(x+1-\alpha)} \tag{4.42}$$

---

[4] These Monte-Carlo simulations, in which space is neglected, bubbles of size i and j aggregate at rate $K_{ij} = i^{-\omega} + j^{-\omega}$ and unit gas bubbles can detach from their bubble at rate $\nu(1-\varphi)/\varphi$, allow to sample the distribution of n_k whose dynamics is given by Eq. (4.33).

Note that the conservation of the volume of gas, $\langle k \rangle = \rho_0$, combined with Eq. (4.42), enforces a first relation between α and ϕ:

$$\phi(2 - \alpha) = 1 \tag{4.43}$$

Plugging the scaling behaviours Eq. (4.42) into Eq. (4.40), we obtain a second relation when $\rho_0 \to \infty$:

$$2 + \phi(3 - \omega - \alpha) = \phi(3 - \alpha) \tag{4.44}$$

Together with Eq. (4.43), it gives the expressions of both the algebraic exponent and the density-dependent cutoff exponent:

$$\alpha = 2 - \omega/2 \tag{4.45}$$

$$\phi = \frac{2}{\omega} \tag{4.46}$$

Interestingly, the $\omega = 0$ case seems to be singular. Indeed, taking $\omega \to 0$ reduces to the model presented in Sec. 4.2.2, for which we know the algebraic exponent to be $\alpha = 5/2$, in contrast with the value $\alpha = 2$ predicted by Eq. (4.45). Looking at Fig. 4.11, we observe that the value $k^*(\omega)$ above which the distribution reaches the algebraic decay $n_k \sim k^{2-\omega/2}$ is increasing as $\omega \to 0$. Extrapolating, we hypothesize that $k^*(\omega) \to \infty$ when $\omega \to 0$, so that we never observe the $\alpha = 2$ regime.

4.3.2 Aggregation-Nucleation Model

We now proceed to investigate the implications of a volume-dependent diffusion in the 1d ANM. To do so, let us first connect the diffusion exponent σ to the aggregation exponent ω of the mean-field model presented above (Sec. 4.3.1). For two point-like bubbles of size i and j diffusing respectively at rate $i^{-\sigma}$ and $j^{-\sigma}$, the Smoluchowski reaction rate theory [Smoluchowski 1917] predicts an aggregation rate $i^{-\sigma} + j^{-\sigma}$, based on a first-passage time computation. This justifies the identification of σ with ω in the following.

In Fig. 4.12a, we plot the stationary distributions of bubbles obtained varying the diffusion exponent σ. Multiplying the distibutions n_k by $k^{2-\sigma/2}$, we observe that they reach a plateau, indicating that the prediction of Eq. (4.45) for the algebraic exponent $\alpha = 2-\sigma/2$ compares favorably with numerical measurements.

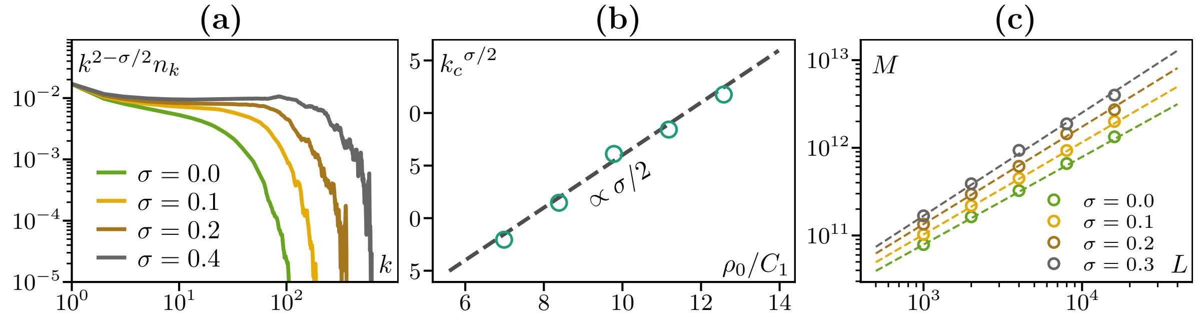

Figure 4.12: 1d local ANM. **(a):** Rescaled distributions, showing $\alpha = 2 - \sigma/2$ (aggregate not shown). **(b):** Scaling of the exponential cutoff with density for $\sigma = 0.5$. The dashed line corresponds to the prediction Eq. (4.50). **(c):** Mass contained in the aggregate compared with the predicted scaling Eq. (4.53) (dashed lines). Parameters: $L = 2000$ (a,b), $\rho_0 = 1$ (a,c), $\nu = 10^{-4}$.

We now investigate the scaling of the exponential cutoff with both density and system size. For $\sigma > 0$, the bubbles diffuse more slowly than for $\sigma = 0$. Numerically, this translates into large averaging times needed to obtain clean cutoff in the distributions so that a simple rescaling is inconclusive based on the data we could gather. To test the prediction of Eq. (4.46) in a different way, we first rewrite Eq. (4.41) in the scaling region $[k_0, k_c]$ as

$$n_k = C_1 k^{-\alpha} \quad \text{for} \quad k_0 \leq k \leq k_c \tag{4.47}$$

where C_1 is a constant which we measure numerically for same $k \in [k_0, k_c]$ using $C_1 = n_k k^{\alpha}$. The cutoff k_c scales as ρ_0^{ϕ}, as in with Eq. (4.41). We write the conservation of density

$$\rho_0 = cst + \int_{k=k_0}^{k_c(\rho_0)} k\, n_k\, dk \tag{4.48}$$

in which cst accounts for the volume of gas contained in the bubbles with $k < k_0$. Using the expression Eq. (4.47) of n_k:

$$\rho_0 = cst + C_1 \int_{k=k_0}^{k_c(\rho_0)} k^{1-\alpha}\, dk \tag{4.49}$$

In the limit $\rho_0 \to \infty$, this gives $k_c^{2-\alpha} \propto (2-\alpha)\dfrac{\rho_0}{C_1}$. Replacing α by its prediction Eq. (4.46), we find

$$k_c^{\sigma/2} \propto \frac{\sigma}{2}\frac{\rho_0}{C_1} \tag{4.50}$$

Looking at Fig. 4.12b, this is indeed what we observe, thus confirming the mean-field prediction $\phi = 2/\sigma$.

We now estimate the total volume of gas contained in the distribution $M(L)$, defined as

$$M(L) = \int_{k=1}^{k_c(L)} k\, n_k\, dk \tag{4.51}$$

Using Eq. (4.47) in which we discard the small-k corrections, we obtain in the limit $L \to \infty$:

$$M(L) \sim L^{\gamma(2-\alpha)} \tag{4.52}$$

which, using both Eq. (4.13) and Eq. (4.45) to replace γ and α, yields:

$$M(L) \sim L^{\frac{\sigma}{2-\sigma}} \tag{4.53}$$

We compare this prediction (dashed lines in Fig. 4.12c) with the finite-size scaling of the total volume of gas contained in the distribution for various values of σ (open circles). We find a good agreement, validating that the mean-field exponents of Sec. 4.3.1 describe correctly the ANM with volume-dependent diffusion.

4.3.3 Reduced Bubble Model

Supplementing the RBM with a volume-dependent diffusion $D = D_0 A^{-\sigma}$, we find the phenomenology to remain the same: at high enough gas fraction, a macroscopic gas reservoir coexists with a dilute gas of bubbles distributed algebraically. Since the gas reservoir is extensive with system size, we expect its diffusion coefficient to vanish in the thermodynamic limit. In contrast, looking at movies of the bubble dynamics, we always observe the reservoir to diffuse. We traced this back to the merging process with small bubbles, which displaces its center of mass at each collision. In line with this observation, its effective diffusion coefficient D_{eff} is the sum of the inner diffusion of the reservoir and the diffusion related to the collisions with small bubbles D_c:

$$D_{\text{eff}} = D_0 A^{-\sigma} + D_c \tag{4.54}$$

We now proceed to evaluate D_c. The number of collisions of the reservoir with small bubbles per unit time is proportional to its perimeter, and thus to its radius, that we note R. Each collision displaces the reservoir of a small distance δx. In the large size limit, we assume the small bubbles to be of radius $r \ll R$, so that the center of mass of the reservoir moves, at each collision, by an amount

$$\delta x = \frac{(R+r)\pi r^2}{\pi R^2 + \pi r^2} \sim R^{-1} \tag{4.55}$$

The expression of D_c is now readily obtained by multiplying the number of collision per unit time by the squared displacement of each collision:

$$D_c = R\delta x^2 \sim R^{-1} = A^{-1/2} \tag{4.56}$$

All in all, $D_{\text{eff}} = D_0 A^{-\sigma} + D_0^c A^{-1/2}$ where D_0^c is a prefactor accounting for the properties of the small bubbles merging with the reservoir. In the limit of large systems, we predict a crossover between a diffusion dominated by the inner diffusivity of the reservoir ($\sigma < 1/2$) to a diffusion driven by the collision with the surrounding gas ($\sigma > 1/2$). We test this prediction by measuring the mean-squared displacement $\langle \Delta r^2(t) \rangle$ in dimension $d = 2$ of the reservoir to extract the effective diffusion coefficient:

$$D_{\text{eff}} = \frac{d}{dt}\left(\frac{\langle \Delta r^2(t) \rangle}{2d}\right) \tag{4.57}$$

Looking at Fig. 4.13a, we indeed observe such crossover taking place for $\sigma \approx 1$. This difference with the predicted value $\sigma = 1/2$ is not surprising: we made the approximation that the reservoir collides with bubbles much smaller than its size and thus discarded the properties of the bubble size distribution, which we can expect to play a quantitative role in the precise position of the crossover.

We now investigate the scaling properties of the distribution of bubble areas. Since the mean-field prediction of the algebraic exponent $\alpha = 5/2$ was consistent with the measured value when $\sigma = 0$ (Sec. 4.2.3), one could expect the prediction to hold when $\sigma > 0$. In order to test this, we follow Smoluchowski's reaction rate theory [Smoluchowski 1917] and assume that two bubbles of sizes A_i and A_j react at rate

$$K_{A_i,A_j} = D_{\text{eff}}(A_i) + D_{\text{eff}}(A_j) \tag{4.58}$$

in spatial dimension $d = 2$. In Eq. (4.58), we neglected a slowly varying logarithmic factor $\ln(\sqrt{A_i}+\sqrt{A_j})$. As discussed above, the reservoir diffuses as $D_{\text{eff}} \sim A^{-\sigma}$ when $\sigma < 1$ so we extrapolate and make the approximation that this remains true for all bubbles, so that

$$K_{A_i,A_j} = A_i^{-\sigma} + A_j^{-\sigma} \tag{4.59}$$

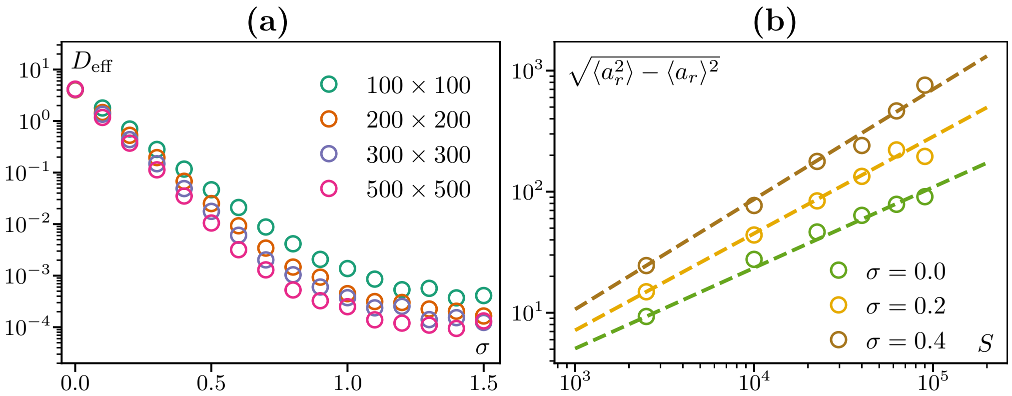

Figure 4.13: Reservoir dynamics in the RBM. **(a):** Effective diffusion coefficient of the macroscopic reservoir. **(b):** Fluctuations of the macroscopic reservoir area as a function of system size, compared with the prediction of Eq. (4.60). Parameters: $x_g = 0.7$, $\nu = 10^{-3}$.

We thus identify the aggregation exponent ω of the mean-field model with σ and predict the exponent $\alpha = 2-\sigma/2$. In contrast, looking at Fig. 4.14, we numerically estimate the exponent α to be larger than 2. This discrepancy might be explained by our approximation Eq. (4.58) in which we neglected the logarithmic prefactor. So far, we have no quantitative explanation for the value of these exponents. Going further, as the measured value of α is greater than 2, the reservoir survives in the thermodynamic limit, which markedly contrasts with the ANM and more generically with the MIPS phenomenology.

As before, the exponential cutoff is observed to shift with system size, as shown in the insets of Fig. 4.14. We find the cutoff to collapse when rescaling the bubble sizes by $S^{-\gamma}$ with γ depending on the value of the diffusion exponent σ. Interestingly, our numerical analysis seems to point towards the existence of a hyperscaling relation $\alpha + \gamma = 3$. So far we have no analytical explanation to support this observation.

The reasoning on the fluctuations of the macroscopic reservoir (Eq. (4.31)) described in Sec. 4.2.4 also applies in the case of the RBM with volume-dependent diffusion. It leads to the following scaling for the fluctuations of the reservoir area a_r:

$$\sqrt{\langle a_r^2\rangle - \langle a_r\rangle^2} \sim S^{\frac{1}{\alpha-1}} \tag{4.60}$$

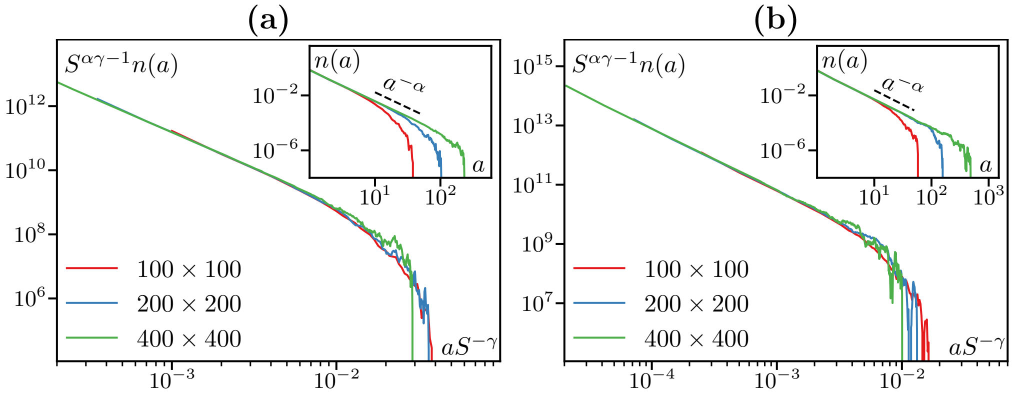

Figure 4.14: Rescaled distributions of bubble sizes in the $2d$ RBM for $\sigma = 0.2$ (a) and $\sigma = 0.4$ (b). Insets are the same distributions without rescaling. **(a):** $\alpha = 2.25$, $\gamma = 0.75$. **(b):** $\alpha = 2.1$, $\gamma = 0.9$. Parameters: $\nu = 10^{-4}$, $x_g = 0.3$.

To test this prediction, we extract the value of α varying σ from numerical simulations of the local RBM in $2d$ (See Fig. 4.14). We verified that the value of this exponent does not depend on space dimension, but only on σ. This gives us an estimate of $S^{\frac{2}{\alpha-1}}$ that we plot in dashed lines in Fig. 4.13a. We then measure the fluctuations of the reservoir area for the same values of σ, plotted as open circles on the same figure. We find that the predicted scaling Eq. (4.60) is in agreement with the observed values.

4.4 Homogeneous nucleation

In the RBM, we have shown in Sec. 4.2.3 that the measured exponent α lies between 2 and 2.5 depending on the scaling of D. Although it is the model that we have studied that could be expected to be the closest to microscopic models showing MIPS, the measured α exponent are quite different. In particular, the distributions we obtain in the RBM are too narrow to contain all the volume of gas of the system in the thermodynamic limit because the total volume of gas they can accommodate converges to a finite value. The macroscopic reservoir persists in the thermodynamic limit, in contrast with the observations of [Tjhung *et al.* 2018, Shi *et al.* 2020, Fausti 2021], who witness instead a homogeneous dense liquid containing bubbles but no macroscopic gas reservoir. Such a scenario occurs when the algebraic decay $\alpha < 2$, making the distribution broad enough to contain all the gas in the thermodynamic limit so that the gas reservoir vanishes. As a result,

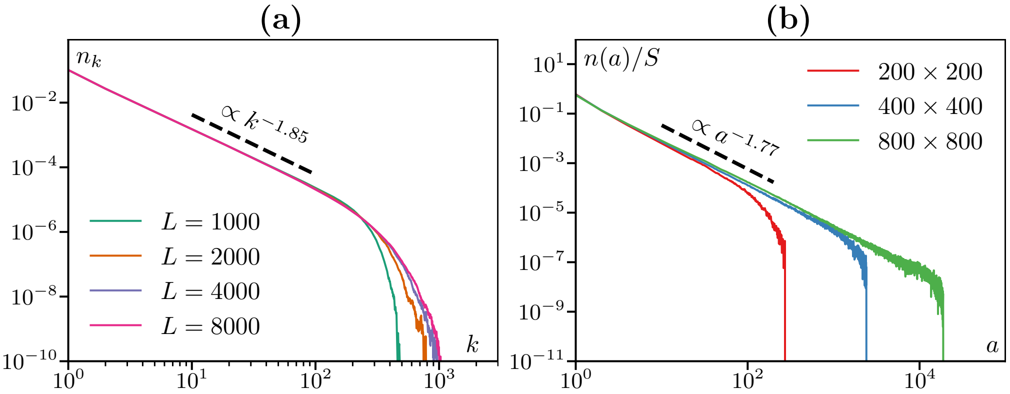

Figure 4.15: PDF for ANM (a) and RBM (b) with non-local nucleation. Parameters: **(a):** $\rho_0 = 1$, $\nu = 10^{-1}$. **(b):** $x_g = 0.7$, $\nu = 10^{-4}$.

the phase diagram we obtain with the RBM is different from the one observed in MIPS. We now present another nucleation mechanism which leads to exponents $\alpha < 2$ in our models, so that the MIPS phase diagram is qualitatively recovered in the thermodynamic limit.

Based on the study of microscopic simulation movies and on the analysis of AMB+ carried in [Tjhung *et al.* 2018], the nucleation process can be explained through the following picture: since the nucleation rate is small, the system has enough time to mix between two nucleation events. As a result, all the bubbles in the system effectively contribute to the nucleation of one bubble. We proceed to give evidences that a homogeneous nucleation process involving all the bubbles is a sufficient ingredient to qualitatively recover the MIPS phase diagram in the thermodynamic limit. To do so in the ANM, instead of nucleating a unit bubble on a vacant site by taking it from the nearest bubble, we extract it from a randomly chosen bubble in the system. In the RBM, following [Shi *et al.* 2020], we nucleate a bubble at the cost of all other bubbles: they shrink by a quantity $\kappa r(1 - r_0/r)$ (where r is their current radius), with κ chosen such that the total area of gas is conserved. This simple difference in the nucleation process gives rise to algebraic distributions compatible with microscopic models presenting MIPS, in the sense that the measured exponent $\alpha < 2$, as shown in Fig. 4.15). This provides indications that in-depth investigations of the role of a homogeneous nucleation process could help understand the bubble dynamics observed in MIPS.

4.5 Conclusion

We have provided a detailed study of several models of aggregation and nucleation to explain the bubble dynamics in MIPS and showed that they typically display scale-free distributions. We first introduced a model in which we neglect the spatial extension of bubbles, the Aggregation-Nucleation Model (ANM). Consistently with both particle-level simulations and continuum descriptions of MIPS [Tjhung *et al.* 2018, Caporusso *et al.* 2020, Shi *et al.* 2020, Fausti 2021], our model features algebraic distributions and a gas reservoir at high bubble density. To account for these observations, we constructed a mean-field description of its dynamics and derived an analytical solution through a mapping with a model of chipping presented in [Krapivsky *et al.* 2010]. We then considered bubbles with a spatial extension (Reduced Bubble Model, RBM) and reported the same phenomenology as in the ANM. Our models present algebraic distributions but the macroscopic aggregate that they exhibit survives in the thermodynamic limit, so that their phase diagrams differ qualitatively from microscopic simulations of MIPS.

Next, we studied the consequences of endowing bubbles with a volume-dependent diffusion coefficient and found that the scaling of the diffusion influences the scaling of bubble sizes. Following pre-established procedures [Rajesh & Majumdar 2001, Rajesh *et al.* 2002], we obtained the bubble distributions dependence on the scaling of the diffusion and compared them to numerical simulations. Finally, we analyzed the effect of a homogeneous nucleation process in our models and found it to be a sufficient condition to obtain algebraic distributions with exponents in qualitative agreement with those measured in MIPS.

Several questions brought up in this chapter are yet to be addressed. First, because at coexistence the dense phase of MIPS consistently displays bubbles in contact with a gas reservoir, we investigated in appendix B a ‘grand-canonical’ version of the mean-field model. We determined a new set of exponents quantitatively different from the ‘canonical’ ones. This seems to point toward a fundamental difference between a canonical and a grand-canonical description of the bubbles statistics in MIPS, in clear contrast with the equilibrium case, where one expects both descriptions to agree in the thermodynamic limit.

Second, analytical expressions for the exponents in the RBM with volume-dependent diffusion remain to be found and should help understand why the observed algebraic exponent is larger than 2 in this model. In contrast, we observe a homogeneous nucleation process to lead to exponents smaller than 2, but a clear explanation for this is yet to be determined. To further test the robustness of our results, it would be interesting to compare the exponents of our bubble models with a thorough analysis of those obtained from a continuum description. Finally, while the question of the coarsening process has not been tackled in this work, we expect our analysis to lay the groundwork for future investigations.

Conclusion

In this thesis, we studied the ordered phases of two paradigmatic phase transitions occurring in active matter: flocking and motility-induced phase separation. Through the analysis of the active Ising model (AIM) in Chapter 2, we showed that order in $1d$ flocking takes the peculiar form of a moving ordered aggregate of particles. Contrary to the passive Ising model, the system thus orders, but symmetry is not broken because the 'flock' stochastically reverses its direction of motion due to the effect of fluctuations.

At low temperature, we found static asters that relies on an original mechanism by which two clusters can block each other just because of alignment interactions. Their slow coarsening relies on rare fluctuations, giving rise to extremal dynamics, and eventually saturates leading to an extensive number of asters. For now, the observation of asters is limited to the $1d$ AIM on lattice. It will be interesting to study what happens in higher dimension and in continuous space when an effective lattice structure exists, such as a crystal. Since these objects could appear in numerical or experimental situations with effective discrete space, it would be interesting to study their dynamics in details.

In Chapter 3, we found that counter-propagating droplets nucleate both in the coexistence and in the ordered phase of the AIM and destroy the ordered state in arbitrary spatial dimension. We predicted these droplets to exist in all flocking models with discrete-symmetry order parameter. This could be systematically checked by introducing a counter-propagating droplet in the ordered phase in other models such as the clock model presented in [Solon *et al.* 2022], or by looking for growing droplet solutions in the associated continuum theory. Such a study would also contribute to a better understanding of the limitations of the hydrodynamic equations used to describe flocking models at the continuous level. Indeed, as demonstrated in the case of the Vicsek model, these equations do not always account for counter-propagating objects leading to reversals of the flow. Overall, the recent results on the fragility of the ordered state in flocking models suggest to probe the stability of the polar order in the Vicsek model to spontaneous nucleations, both in the coexistence phase and in the homogeneous ordered state.

In Chapter 4, we investigated the bubbly phase separation in MIPS. We introduced several bubble models to account for the bubble dynamics and found the bubble sizes to be generically scale-free distributed. We examined how the decay exponent α and the finite-size effects depend on the basic ingredients that we used. Even though we are able to predict accurately the value of α in some cases where we neglect the bubble spatial extension, we still lack analytical explanations for the role of the bubble spatial occupation. We found the value of the exponents to be sensitive to the specific ingredients of our models, which questions their universal nature. Finally, in a recent study, [Digregorio *et al.* 2021] suggest that MIPS bubbles appear concomitantly with a network of 'defects' in the dense region, so that bubble nucleation results from defect-induced dislocations of dense domains. This provides interesting microscopic fundations to study the nucleation process of bubbles as sudden, rare events.

More generally, we considered the exotic properties of ordered phases in flocking models and in MIPS separately, but in both cases nucleation events play an essential role. A promising framework to understand the occurrence of these rare events is transition path sampling. How to apply these techniques in the context of non-equilibrium physics is however still a topic under development [Berryman & Schilling 2010, Zakine & Vanden-Eijnden 2022].

CHAPTER 5

Synthèse en français

La matière active englobe tous les systèmes dont les composants dissipent de l'énergie afin d'exercer des forces sur leur environnement. Les systèmes actifs peuvent être trouvés à toutes les échelles, des moteurs moléculaires aux groupes d'animaux, en passant par les colonies de bactéries. Étant intrinsèquement hors d'équilibre, ces systèmes présentent de manière générique des comportements collectifs sans contrepartie à l'équilibre.

Nous nous sommes concentrés sur deux comportements collectifs paradigmatiques en matière active : le *flocking*, dans lequel des particules auto-propulsées et soumisent à des interactions d'alignement s'organisent à grand échelle pour se déplacer collectivement, et la séparation de phase induite par la motilité, dans laquelle des particules auto-propulsées et soumises à des forces répulsives forment un agrégat. Ces comportements collectifs présentent des propriétés exotiques que nous avons étudié dans cette thèse.

* * *

En une dimension, le mouvement collectif se traduit par la présence d'un agrégat de particules au mouvement ballistique qui subit des retournements stochastiques de sa direction [Czirók *et al.* 1999, O'Loan & Evans 1999, Dossetti 2011, Laighléis *et al.* 2018, Sakaguchi & Ishibashi 2019]. Nous nous sommes intéressés dans le Chapitre 2 au modèle d'Ising actif, un modèle de flocking avec une symétrie discrète. Dans ce modèle, l'agrégat possède une forme particulière représentée sur la Fig. 5.1 (gauche). Il est constituée d'un pic de largeur σ qui s'étale diffusivement et d'une protrusion et se propage à une vitesse v_p comme indiqué sur la Fig. 5.2a. Les valeurs de σ et de v_p peuvent être prédites *via* une analyse de champ moyen. La caractéristique la plus frappante des flocks est qu'ils subissent des retournements stochastiques de leur direction de propagation. Cela arrive lorsqu'une fluctuation

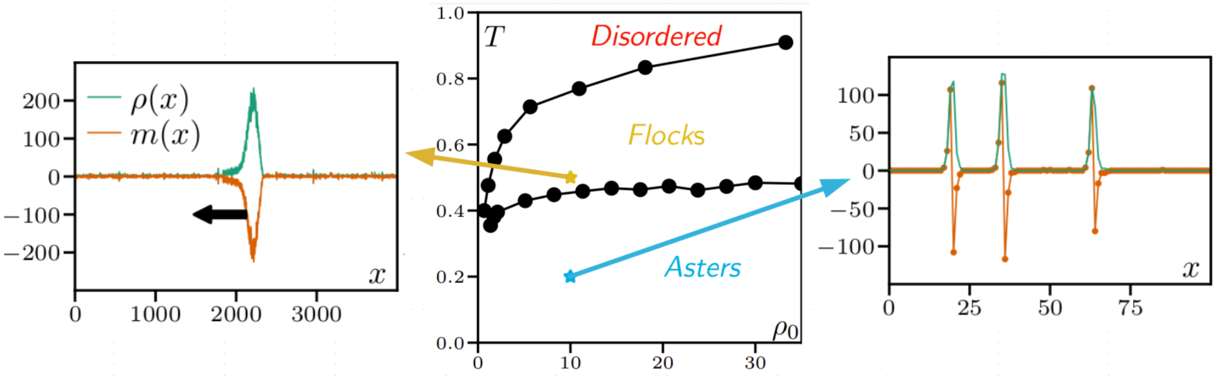

Figure 5.1: Diagramme des phases du modèle d'Ising actif en une dimension dans le plan densité-température (milieu) et profils de densité ρ et d'aimantation m associés aux phases Flocks (gauche) et Asters (droite).

à l'avant de l'agrégat, si elle est d'amplitude suffisante et d'aimantation opposée à celle de l'agrégat, se propage dans celui-ci en retournant le spin de toutes les particules qu'elle rencontre. Nous avons mesuré le temps séparant deux retournements et avons trouvé qu'il diverge comme le logarithme de la taille du système (voir Fig. 5.2b). En calculant la distribution des temps entre retournements, nous avons pu expliquer cette dépendance. Contrairement au modèle d'Ising passif, le système présente donc une phase ordonnée, bien que la symétrie ne soit pas brisée puisque l'agrégat retourne stochastiquement sa direction de déplacement sous l'effet des fluctuations.

À basse température, nous observons l'existence d'une nouvelle phase peuplée d'objets statiques que nous appelons “asters” (voir Fig. 5.1 (droite)), qui apparaissent uniquement en raison de l'interaction entre l'auto-propulsion et l'alignement. Ces structures prennent la forme de deux pics d'aimantation opposés qui se font face et empêchent ainsi la progression de l'autre. Nous avons calculé leur forme à l'aide d'une description de champ moyen, comme représenté en pointillés sur la Fig. 5.3a. À température nulle, les asters ont une durée de vie T avant dissolution qui dépend du nombre M de particules qui les composent. En utilisant un calcul de temps de premier passage, nous avons obtenu une solution exacte pour caractériser cette durée de vie (voir Fig. 5.3b). Pour l'instant, l'observation des asters est limitée au modèle d'Ising actif $1d$ sur réseau. Comme ces objets pourraient

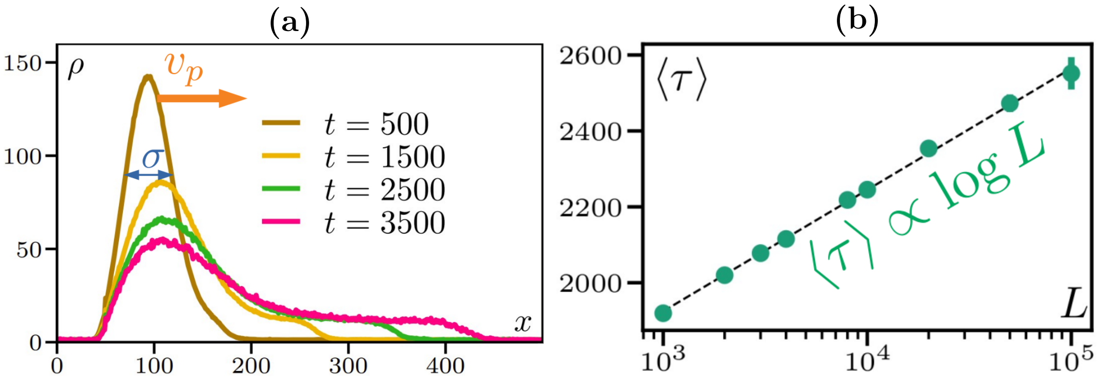

Figure 5.2: **(a) :** Évolution de la forme d'un flock se propageant à vitesse constante v_p au cours du temps et dont le pic possède une largeur σ. **(b) :** Temps moyen $\langle\tau\rangle$ séparant deux retournements en fonction de la taille du système L.

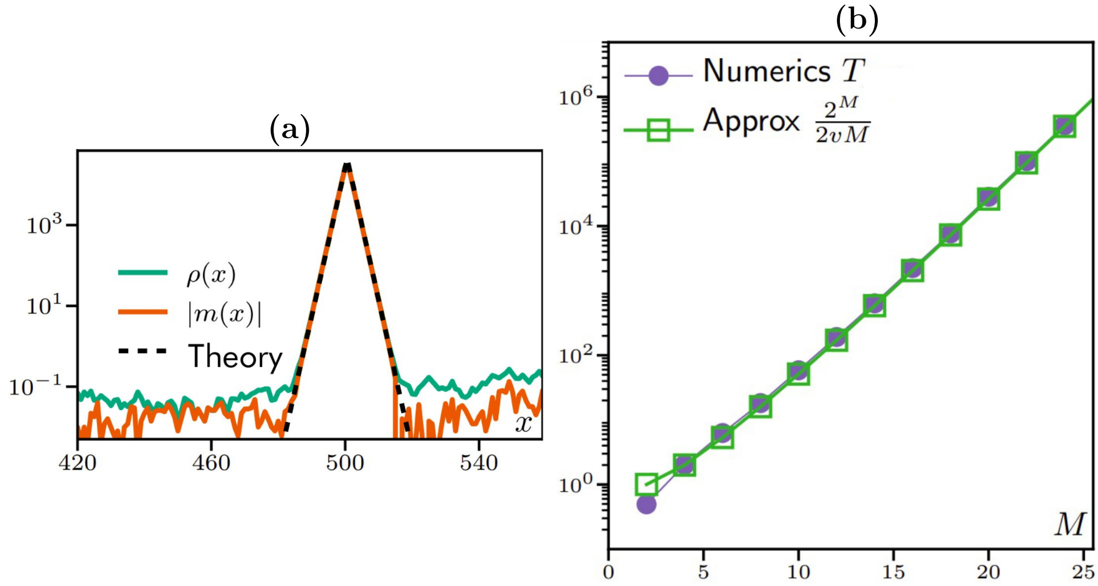

Figure 5.3: **(a) :** Profils de densité ρ et d'aimantation m dans un aster, comparés à la prédiction théorique (pointillés). **(b) :** Temps de dissolution T d'un aster contenant M particules.

néanmoins apparaître dans des situations numériques ou expérimentales avec un espace discret effectif, comme dans un crystal, il serait intéressant d'étudier leur dynamique en détail.

Dans le Chapitre 3, nous avons étudié les états ordonnés du modèle d'Ising actif en dimension $d > 1$. Jusqu'à présent, de tels états étaient considérés comme stables, mais nous avons montré qu'ils sont en réalité métastables dû à la nucléation spontanée de gouttelettes se propageant dans le sens contraire à l'ordre établi. Nous nous sommes tout d'abord intéressés à la phase de coexistence du modèle d'Ising actif en dimension $d = 2$, dans laquelle une bande ordonnée de haute densité se déplace dans un gas résiduel désordonné. Nous avons montré que des gouttellettes d'aimantation opposée apparaissent à l'avant de la bande et détruisent sa structure en se propageant à l'intérieur, comme illustré sur la Fig. 5.4a. Ce scénario persiste dans la phase homogène ordonnée (voir Fig. 5.4b), dans laquelle une assez grande fluctuation d'aimantation entraîne la nucléation d'une gouttelette se déplaçant en sens inverse. En étudiant numériquement la taille minimale d'une telle fluctuation ainsi que son taux de nucléation, nous avons montré qu'elle se produit spontanément dans la limite thermodynamique, de telle sorte que la phase homogène ordonnée est métastable. Afin de renforcer ce résultat, nous avons ensuite montré que les équations continues décrivant notre système admettent des solutions prenant la forme de gouttelettes en toute dimension $d > 1$.

Nos résultats concernant la métastabilité des états ordonnés du modèle d'Ising actif s'inscrivent dans la lignée d'une série de récentes publications faisant état de la fragilité des phases de mouvement collectifs dans les modèles de flocking, en particulier dans le modèle de Vicsek [Ventejou *et al.* 2021, Codina *et al.* 2022, Besse *et al.* 2022]. Nous avons montré qu'en se restreignant à un paramètre d'ordre à symétrie discrète, les modèles de flocking ont des états ordonnés métastables dans l'ensemble du diagramme des phases. Dans le cas d'un paramètre d'ordre à symétrie continue, comme pour le modèle de Vicsek, les résultats présentés dans [Codina *et al.* 2022] montrent que cette métastabilité n'existe que dans une fraction du diagramme des phases, ce qui indique une différence fondamentale entre les modèles à paramètre d'ordre scalaire et à paramètre d'ordre vectoriel.

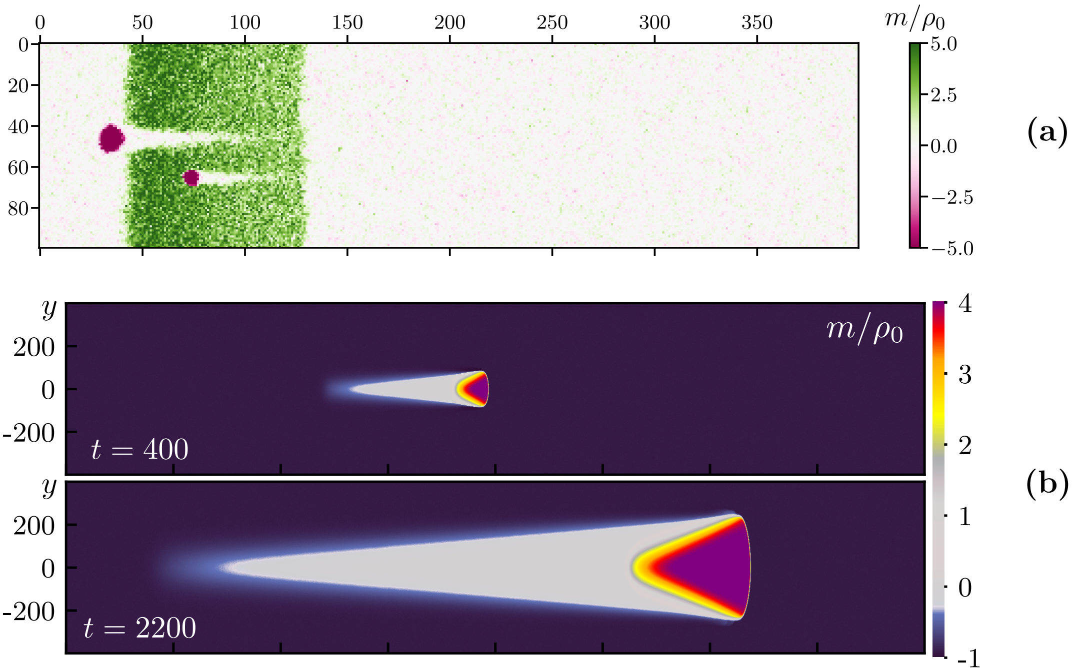

Figure 5.4: Nucléation de gouttelettes se propageant dans le sens opposé à l'ordre établi dans la phase de coexistence **(a)** et dans la phase homogène ordonnée **(b)** du modèle d'Ising actif en dimension $d = 2$.

Dans la séparation de phase induite par la motilité, le couplage entre le mouvement persistant des particules actives et leurs interactions répulsives conduit à la formation d'un agrégat dense entouré d'un gaz dilué. Parce que la pression de Laplace est négative [Bialké *et al.* 2015, Solon *et al.* 2018a, Patch *et al.* 2018], des bulles de gaz se forment et se développent dans cet agrégat, de sorte que le cadre général est celui d'une séparation de phase à bulles, dans laquelle les tailles de bulles sont distribuées algébriquement. Dans les systèmes de taille finie à faible densité, les bulles coexistent avec un grand réservoir de gaz. En augmentant la densité de particules à taille de système fixée, de plus en plus de gaz est contenu dans les bulles. Au-delà d'une densité critique, le réservoir de gaz disparaît et seule la distribution algébrique subsiste, terminée par une coupure exponentielle dépendant de la densité.

Nous avons présenté dans le Chapitre 4 des modèles minimaux pour rendre compte de la dynamique de ces bulles. Dans ces modèles, les degrés de liberté sont

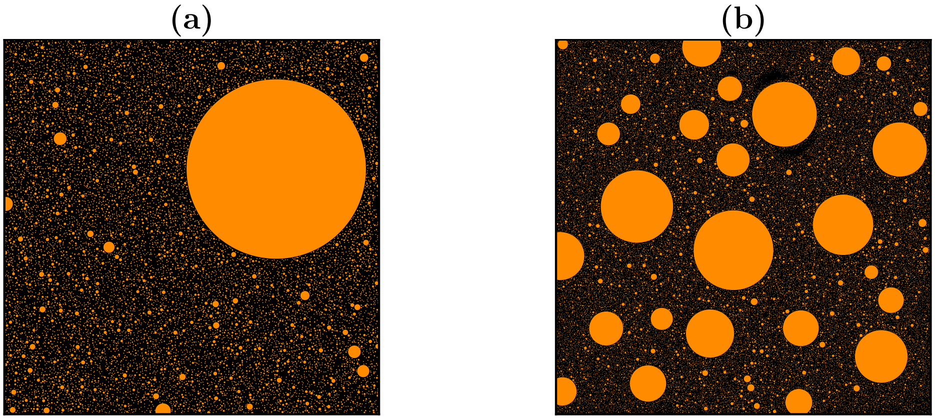

Figure 5.5: Clichés instantanés d'un modèle de bulle montrant la présence d'un réservoir de gaz à basse densité **(a)** et sa disparition en augmentant la densité **(b)**.

des bulles qui diffusent et fusionnent en cas de contact. La formation des bulles est modélisée par un processus de nucléation à taux constant par unité d'espace ν. Malgré leur simplicité, ces modèles reproduisent la présence d'un réservoir de gaz à basse densité (voir Fig. 5.5a) et sa disparition à mesure que la densité augmente (voir Fig. 5.5b), tout en présentant des distributions de taille de bulles en loi de puissance. Nous avons développé des arguments analytiques permettant de calculer l'exposant de ces lois de puissance dans certains cas ainsi que de prédire la disparition du réservoir. Enfin, nous avons présenté des éléments numériques indiquant que pour capturer correctement la phénoménologie microscopique de MIPS, le processus de nucléation doit être non-local.

Nous avons constaté que la valeur des exposants était sensible aux ingrédients spécifiques de nos modèles, ce qui remet en question leur nature universelle. Par ailleurs, dans une récente étude, [Digregorio *et al.* 2021] suggère que la région dense est composée d'un réseau de "défauts", de sorte que la nucléation des bulles résulte de dislocations de domaines denses induites par des défauts. Cela fournit des bases microscopiques intéressantes pour étudier le processus de nucléation des bulles en tant qu'événements soudains et rares.

Dans cette thèse, nous avons étudié les phases ordonnées dans deux transitions de phases paradigmatiques en matière active : le flocking et la séparation de phase induite par la motilité. Nous avons examiné leurs propriétés exotiques séparément, mais dans les deux cas, les événements de nucléation jouent un rôle essentiel. Un cadre prometteur pour comprendre l'occurrence de ces événements rares est le "transition path sampling". Comment appliquer ces techniques dans le contexte de la physique hors d'équilibre reste cependant un sujet en cours de développement [Berryman & Schilling 2010, Zakine & Vanden-Eijnden 2022].

Appendices

APPENDIX A

Measure of the probability of reversal

In this appendix, we give precisions about the numerical procedure followed in simulations of Chapter 3 in which a droplet of oppositely moving particles is inserted in an ordered phase. At time $t = 0$, we initialize the system by randomly distributing particles with spins $s = -1$ until a density ρ_o is reached. After an equilibration time $t_r = 100$, a circular droplet of radius r—modulo lattice discretization effects—centered at $\mathbf{i} = (0, 0)$ is modified as follows. First, the spins located at sites within a distance r from the center are set to $s = +1$. Second, an additional $\Delta N = (\rho_d^0 - \rho_\mathrm{o})\pi r^2$ particles with spins $s = +1$ are randomly distributed inside the droplet, leading to a droplet density $\rho_d^0 > \rho_\mathrm{o}$ and a magnetization ρ_d^0.

We note that, when a droplet has grown significantly after having traveled a large enough distance, it takes over the entire ordered phase. To estimate P_r, we thus proceeded as follows:

- We place a droplet with a positive magnetization in a negative-magnetization flock at $\mathbf{i} = (0, 0)$ as described before.
- We record the magnetization of a 5×5 square region centered at $(\Delta x, 0)$ during a time interval $\Delta t = 4(\Delta x/v)$, with $\Delta x = 50$. This time is short enough to allow for good statistics, yet sufficiently long to assess whether the droplet has grown or receded after having traveled the distance Δx from its seeding.
- If the average magnetization in the region increases by more than ρ_o at any time during the measurement, we conclude that the droplet will keep growing and will eventually reverse the entire flock. Δx is chosen to ensure the robust prediction of the droplet's fate.

- If the magnetization does not rise above the threshold by the end of the measurement at $t = t_r + 4(\Delta x/v)$, we conclude that the perturbation induced by the droplet will recede into the ordered phase.
- We repeat this protocol 100 times to estimate P_{r}.

The various parameters of this procedure have been chosen to ensure a robust prediction of the droplet's fate.

Appendix B

Grand-canonical description

In this appendix, we analyze the consequences of a grand-canonical description of the bubble models presented in Chapter 4. Since in the coexistence phase of MIPS, the picture is that of a gas in contact with a macroscopic reservoir, one could expect a grand-canonical description to be well-suited to the study of the system. We now present such a grand-canonical description of our model, in terms of a generalization of the mean-field equations Eq. (4.33).

B.1 Generalization of the mean-field model

It contains the same ingredients as the previous models, but the system is now in contact with a gas reservoir. Nucleation of a unit gas mass can happen at the expense of an existing bubble at rate λ or at the expense of the reservoir with rate $\nu(1-\varphi)$. As before, bubbles aggregate following the generalized aggregation kernel introduced in Sec. 4.3 so that the aggregation of bubbles of sizes i and j occurs at rate $K_{ij} = i^{-\omega} + j^{-\omega}$. Finally, bubbles are absorbed by the reservoir upon collision with it. In practice, a bubble of size i is removed at rate $i^{-\omega}$, because its rate of collision with the reservoir depends on its ability to diffuse. Let us write the dynamics of the fraction of bubbles of size k:

$$\begin{aligned}\partial_t n_k = {} & \frac{1}{2}\sum_{i=1}^{k-1}((k-i)^{-\omega} + i^{-\omega})n_{k-i}n_i - n_k \sum_{i=1}^{+\infty}(k^{-\omega} + i^{-\omega})n_i \\ & + \lambda(n_{k+1} - n_k) + \lambda\varphi\delta_{1,k} \\ & + \nu(1-\varphi)\delta_{1,k} \\ & - K k^{-\omega} n_k \end{aligned} \tag{B.1}$$

Using the generating functions Eqs. (4.35) we recast the previous equation into

$$\begin{aligned}\partial_t \mathcal{C}(p) - \partial_t \varphi = {} & \mathcal{A}(p)\mathcal{C}(p) - \mathcal{A}(p)\varphi - \mathcal{C}(p)A + A\varphi \\ & + \lambda \mathcal{C}(p)\left(e^p - 1\right) \\ & - [\nu(1-\varphi) + \lambda\varphi](1 - e^{-p}) \\ & + K(A - \mathcal{A}(p))\end{aligned} \tag{B.2}$$

B.2 Naive grand-canonical model

As in section Sec. 4.3.1, we use the series expansions of the generating functions Eq. (4.38) to identify the powers of p and obtain the time evolution of the first moments of n_k:

$$\partial_t \langle k \rangle = \nu(1-\varphi) - K\langle k^{1-\omega}\rangle \tag{B.3}$$

$$\partial_t \langle k^2 \rangle = 2\langle k \rangle \langle k^{1-\omega}\rangle - 2\lambda\langle k \rangle + 2\lambda\varphi + \nu(1-\varphi) - K\langle k^{2-\omega}\rangle \tag{B.4}$$

where we dropped the explicit time-dependence for legibility. This system is not closed since the dynamics of each moment is coupled to higher-order moments. To make progress, we want to relate the moments of n_k to the density of particles $\langle k \rangle$. To do so, we make the generic ansatz that at large k, the distribution n_k behaves as a power-law terminated by a cutoff which depends on the (time-dependent) density:

$$n_k = k^{-\alpha} f\left(\frac{k}{\langle k \rangle^{\phi}}\right) \tag{B.5}$$

The moment of order x, namely $\langle k^x \rangle$, can be computed using this ansatz, since

$$\langle k^x \rangle = \int_0^{+\infty} k^x n_k dk \tag{B.6}$$

We thus obtain the following relation:

$$\langle k^x \rangle = F(x)\langle k \rangle^{\phi(x+1-\alpha)} \tag{B.7}$$

with $F(x) = \int_0^{+\infty} u^{x-\alpha} f(u) du$. In particular, plugging in $x = 1$ implies

$$\phi(2-\alpha) = 1 \tag{B.8}$$

In stationary state, Eq. (B.3) gives

$$K = \frac{\nu(1-N)}{\langle k^{1-\omega}\rangle} \tag{B.9}$$

Using Eq. (B.7), we obtain $\langle k^{1-\omega}\rangle = F(1-\omega)\langle k\rangle^{2-\alpha-\omega}$ and we deduce a relation between the density $\langle k\rangle$ and K:

$$K = \frac{\nu(1-\varphi)}{F(1-\omega)}\langle k\rangle^{\phi(\alpha+\omega-2)} \tag{B.10}$$

We now insert Eq. (B.9) into the stationary state of Eq. (B.4) and obtain, at the highest order in $\langle k\rangle$:

$$2\langle k\rangle\langle k^{1-\omega}\rangle = \frac{\nu(1-\varphi)}{F(1-\omega)}\langle k\rangle^{\phi(\alpha+\omega-2)} \tag{B.11}$$

Using the scaling of $\langle k^{1-\omega}\rangle$, we finally obtain $1 = \phi(3-\omega-\alpha)$ which, together with $\phi(2-\alpha) = 1$, gives:

$$\begin{cases} \phi = \dfrac{2}{1+\omega} \\ \\ \alpha = \dfrac{3-\omega}{2} \end{cases} \tag{B.12}$$

The expression of the exponent α obtained is different from the one obtained in the canonical case ($\alpha = 2-\omega/2$). We verify this by simulating Eq. (B.1) for various values of ω. As seen in Fig. B.1a, plotting $k^{2-\omega/2}n_k$, the rescaled distributions do not converge to a plateau, confirming that the exponent α indeed differs from the canonical case. Looking at Fig. B.1b where we plot the measurement of α compared with the predicted scaling $(3-\omega)/2$, we observe a shift of less than 3%.

Let us come back to Eq. (B.9), where we implicitely assumed $\langle k^{1-\omega}\rangle$ to converge. Using the expression of α, we can check the consistency of our computation. Since $f(\cdot)$ is terminated by an exponential cutoff, by analogy with the Gamma function, we find that $\langle k^{1-\omega}\rangle$ converges if $1-\omega-\alpha > -1$, imposing $\omega < 1$. Under this condition, we can assume a stationary state of Eq. (B.3) to exist, so that density reaches a constant value at large times.

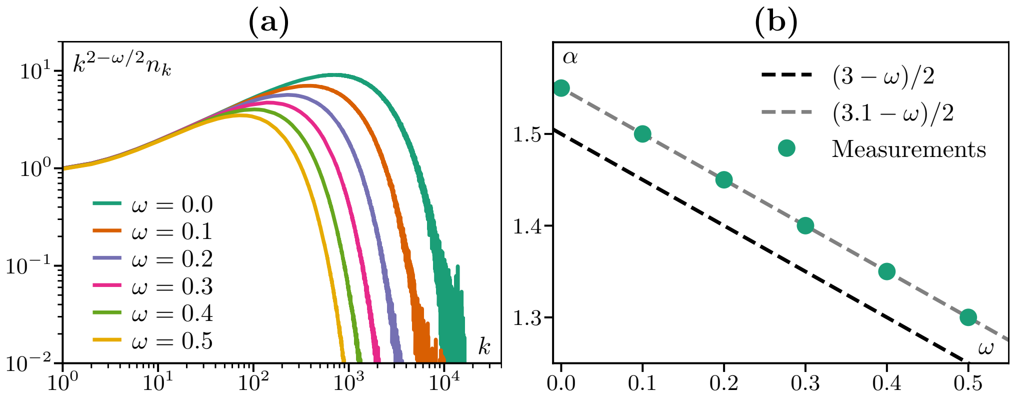

Figure B.1: Rescaled distributions of cluster sizes in Monte-Carlo simulations of the grand-canonical description Eq. (B.1). **(a):** Distributions rescaled with the exponent $\alpha = 2 - \omega/2$ of the canonical model. **(b):** Rescaling with the grand-canonical exponent. Parameters: $L = 10000$, $\nu = 10$, $\lambda = 0$, $K = 0.02$.

The exponents (B.12) coincide with those found in [Krapivsky *et al.* 2010] for a model of aggregation with constant input – akin to the nucleation term of our grand-canonical model – in which density is not conserved. This suggests that both models belong to the same class, so that nucleation from existing bubbles (*i.e.* the λ term) and absorption are actually not contributing to the scaling properties of the system.

B.3 Refined description

The naive grand-canonical description predicts exponent expressions which differs from those obtained in Sec. 4.3 and measured in numerical simulations of the ANM. This is because we implicitely considered that the rates of interaction of the bubbles with the reservoir – nucleation and absorption – take a finite non-vanishing value even in the thermodynamic limit that we consider here. On the other hand, in the 1d ANM of finite size L, the aggregate is contained on one site. In a mean-field description, bubbles thus interact with the reservoir with a rate decreasing as L^{-1}:

$$\nu = \frac{\nu'}{L} \tag{B.13}$$

$$K = \frac{K'}{L} \tag{B.14}$$

which vanish in the thermodynamic limit so that the dynamics of n_k reads:

$$\begin{aligned}\partial_t n_k = \frac{1}{2}\sum_{i=1}^{k-1}((k-i)^{-\omega} + i^{-\omega})n_{k-i}n_i - n_k \sum_{i=1}^{+\infty}(k^{-\omega} + i^{-\omega})n_i \\ + \lambda(n_{k+1} - n_k) + \lambda\varphi\delta_{1,k}\end{aligned} \tag{B.15}$$

These are precisely the mean-field equations of aggregation with chipping and mass-dependent diffusion solved by [Rajesh *et al.* 2002] which admit the exponent $\alpha = 2 - \omega/2$, consistently with our results of Sec. 4.3.1.

Bibliography

[Aditi Simha & Ramaswamy 2002] R. Aditi Simha and Sriram Ramaswamy. *Hydrodynamic Fluctuations and Instabilities in Ordered Suspensions of Self-Propelled Particles.* Phys. Rev. Lett., vol. 89, page 058101, Jul 2002. (Cited on page 9.)

[Anderson & Fernandez-Nieves 2022] Caleb Anderson and Alberto Fernandez-Nieves. *Social interactions lead to motility-induced phase separation in fire ants.* Nature Communications, vol. 13, no. 1, page 6710, Nov 2022. (Cited on page 18.)

[Antal & Scheuring 2006] Tibor Antal and Istvan Scheuring. *Fixation of strategies for an evolutionary game in finite populations.* Bulletin of mathematical biology, vol. 68, no. 8, pages 1923–1944, 2006. (Cited on page 52.)

[Aranson 2013] Igor S Aranson. *Active colloids.* Physics-Uspekhi, vol. 56, no. 1, page 79, 2013. Publisher: IOP Publishing. (Cited on page 6.)

[Attanasi *et al.* 2014a] Alessandro Attanasi, Andrea Cavagna, Lorenzo Del Castello, Irene Giardina, Stefania Melillo, Leonardo Parisi, Oliver Pohl, Bruno Rossaro, Edward Shen, Edmondo Silvestri*et al.* *Collective behaviour without collective order in wild swarms of midges.* PLoS computational biology, vol. 10, no. 7, page e1003697, 2014. (Cited on page 6.)

[Attanasi *et al.* 2014b] Alessandro Attanasi, Andrea Cavagna, Lorenzo Del Castello, Irene Giardina, Stefania Melillo, Leonardo Parisi, Oliver Pohl, Bruno Rossaro, Edward Shen, Edmondo Silvestri and Massimiliano Viale. *Finite-Size Scaling as a Way to Probe Near-Criticality in Natural Swarms.* Phys. Rev. Lett., vol. 113, page 238102, Dec 2014. (Cited on page 10.)

[Baglietto & Albano 2009] Gabriel Baglietto and Ezequiel V. Albano. *Nature of the order-disorder transition in the Vicsek model for the collective motion of self-propelled particles.* Phys. Rev. E, vol. 80, page 050103, Nov 2009. (Cited on page 12.)

[Ballerini *et al.* 2008] M. Ballerini, N. Cabibbo, R. Candelier, A. Cavagna, E. Cisbani, I. Giardina, V. Lecomte, A. Orlandi, G. Parisi, A. Procaccini, M. Viale and V. Zdravkovic. *Interaction ruling animal collective behavior depends on topological rather than metric distance: Evidence from a field study.* Proceedings of the National Academy of Sciences, vol. 105, no. 4, pages 1232–1237, 2008. (Cited on page 11.)

[Banerjee 1992] Abhijit V. Banerjee. *A Simple Model of Herd Behavior.* The Quarterly Journal of Economics, vol. 107, no. 3, pages 797–817, 1992. (Cited on page 10.)

[Ben-Jacob 2003] Eshel Ben-Jacob. *Bacterial Self-Organization: Co-Enhancement of Complexification and Adaptability in a Dynamic Environment.* Philosophical Transactions: Mathematical, Physical and Engineering Sciences, vol. 361, no. 1807, pages 1283–1312, 2003. (Cited on page 6.)

[Berg 2004] H.C. Berg. E. coli in motion. Biological and Medical Physics, Biomedical Engineering. Springer, 2004. (Cited on page 4.)

[Berryman & Schilling 2010] Joshua T. Berryman and Tanja Schilling. *Sampling rare events in nonequilibrium and nonstationary systems.* The Journal of Chemical Physics, vol. 133, no. 24, page 244101, dec 2010. (Cited on pages 126 and 133.)

[Berthier & Biroli 2011] Ludovic Berthier and Giulio Biroli. *Theoretical perspective on the glass transition and amorphous materials.* Rev. Mod. Phys., vol. 83, pages 587–645, Jun 2011. (Cited on page 3.)

[Bertrand *et al.* 2021] Thibault Bertrand, Joseph D'Alessandro, Ananyo Maitra, René-Marc Mège, Benoît Ladoux and Raphaël Voituriez. *Clustering and ordering in cell assemblies with generic asymmetric aligning interactions.* In APS March Meeting Abstracts, volume 2021 of *APS Meeting Abstracts*, page C13.003, January 2021. (Cited on page 24.)

[Besse *et al.* 2022] Marc Besse, Hugues Chaté and Alexandre Solon. *Metastability of Constant-Density Flocks.* Phys. Rev. Lett., vol. 129, page 268003, Dec 2022. (Cited on pages 66, 67 and 130.)

[Bialké et al. 2013] Julian Bialké , Hartmut Löwen and Thomas Speck. *Microscopic theory for the phase separation of self-propelled repulsive disks*. EPL (Europhysics Letters), vol. 103, no. 3, page 30008, aug 2013. (Cited on page 16.)

[Bialké *et al.* 2015] Julian Bialké, Jonathan T. Siebert, Hartmut Löwen and Thomas Speck. *Negative Interfacial Tension in Phase-Separated Active Brownian Particles*. Phys. Rev. Lett., vol. 115, page 098301, Aug 2015. (Cited on pages 20, 93, 95, 96 and 131.)

[Binder & Landau 1984] K Binder and DP Landau. *Finite-size scaling at first-order phase transitions*. Physical Review B, vol. 30, no. 3, page 1477, 1984. (Cited on page 32.)

[Bouchaud & Georges 1990] Jean-Philippe Bouchaud and Antoine Georges. *Anomalous diffusion in disordered media: Statistical mechanisms, models and physical applications*. physrep, vol. 195, no. 4-5, pages 127–293, November 1990. (Cited on page 110.)

[Bray 2002] Alan J Bray. *Theory of phase-ordering kinetics*. Advances in Physics, vol. 51, no. 2, pages 481–587, 2002. (Cited on page 82.)

[Bricard *et al.* 2013] Antoine Bricard, Jean-Baptiste Caussin, Nicolas Desreumaux, Olivier Dauchot and Denis Bartolo. *Emergence of macroscopic directed motion in populations of motile colloids*. Nature, vol. 503, no. 7474, pages 95–98, 2013. (Cited on pages 6, 10 and 11.)

[Buhl *et al.* 2006] J. Buhl, D. J. T. Sumpter, I. D. Couzin, J. J. Hale, E. Despland, E. R. Miller and S. J. Simpson. *From Disorder to Order in Marching Locusts*. Science, vol. 312, no. 5778, pages 1402–1406, 2006. (Cited on pages 24 and 25.)

[Buttinoni *et al.* 2013] Ivo Buttinoni, Julian Bialké, Felix Kümmel, Hartmut Löwen, Clemens Bechinger and Thomas Speck. *Dynamical Clustering and Phase Separation in Suspensions of Self-Propelled Colloidal Particles*. Phys. Rev. Lett., vol. 110, page 238301, Jun 2013. (Cited on pages 17 and 18.)

[Bäuerle *et al.* 2018] Tobias Bäuerle, Andreas Fischer, Thomas Speck and Clemens Bechinger. *Self-organization of active particles by quorum sensing rules.* Nature Communications, vol. 9, no. 1, page 3232, August 2018. (Cited on page 17.)

[Callen & Welton 1951] Herbert B. Callen and Theodore A. Welton. *Irreversibility and Generalized Noise.* Physical Review, vol. 83, no. 1, pages 34–40, July 1951. (Cited on page 3.)

[Caporusso *et al.* 2020] Claudio B. Caporusso, Pasquale Digregorio, Demian Levis, Leticia F. Cugliandolo and Giuseppe Gonnella. *Motility-Induced Microphase and Macrophase Separation in a Two-Dimensional Active Brownian Particle System.* Phys. Rev. Lett., vol. 125, page 178004, Oct 2020. (Cited on pages 20, 96, 97 and 122.)

[Caporusso *et al.* 2022] Claudio B. Caporusso, Leticia F. Cugliandolo, Pasquale Digregorio, Giuseppe Gonnella, Demian Levis and Antonio Suma. *Dynamics of Motility-Induced clusters: coarsening beyond Ostwald ripening*, 2022. (Cited on page 111.)

[Cates & Tailleur 2013] M. E. Cates and J. Tailleur. *When are active Brownian particles and run-and-tumble particles equivalent? Consequences for motility-induced phase separation.* EPL (Europhysics Letters), vol. 101, no. 2, page 20010, jan 2013. (Cited on page 16.)

[Cates & Tailleur 2015] Michael E. Cates and Julien Tailleur. *Motility-Induced Phase Separation.* Annual Review of Condensed Matter Physics, vol. 6, no. 1, pages 219–244, 2015. (Cited on page 7.)

[Cates *et al.* 2010] M. E. Cates, D. Marenduzzo, I. Pagonabarraga and J. Tailleur. *Arrested phase separation in reproducing bacteria creates a generic route to pattern formation.* Proceedings of the National Academy of Sciences, vol. 107, no. 26, pages 11715–11720, 2010. (Cited on page 18.)

[Caussin *et al.* 2014] Jean-Baptiste Caussin, Alexandre Solon, Anton Peshkov, Hugues Chaté, Thierry Dauxois, Julien Tailleur, Vincenzo Vitelli and Denis Bartolo. *Emergent spatial structures in flocking models: a dynamical system insight.* Physical Review Letters, vol. 112, no. 14, page 148102, 2014. (Cited on page 83.)

[Cavagna & Giardina 2014] Andrea Cavagna and Irene Giardina. *Bird Flocks as Condensed Matter*. Annual Review of Condensed Matter Physics, vol. 5, no. 1, pages 183–207, 2014. (Cited on page 11.)

[Cavagna *et al.* 2008] Andrea Cavagna, Irene Giardina, Alberto Orlandi, Giorgio Parisi, Andrea Procaccini, Massimiliano Viale and Vladimir Zdravkovic. *The STARFLAG handbook on collective animal behaviour: Part I, empirical methods*, 2008. (Cited on page 10.)

[Cavagna *et al.* 2010] Andrea Cavagna, Alessio Cimarelli, Irene Giardina, Giorgio Parisi, Raffaele Santagati, Fabio Stefanini and Massimiliano Viale. *Scale-free correlations in starling flocks*. Proceedings of the National Academy of Sciences, vol. 107, no. 26, pages 11865–11870, 2010. (Cited on page 6.)

[Chaté *et al.* 2008] Hugues Chaté, Francesco Ginelli, Guillaume Grégoire and Franck Raynaud. *Collective motion of self-propelled particles interacting without cohesion*. Physical Review E, vol. 77, no. 4, page 046113, 2008. (Cited on page 12.)

[Chepizhko *et al.* 2013] Oleksandr Chepizhko, Eduardo G. Altmann and Fernando Peruani. *Optimal Noise Maximizes Collective Motion in Heterogeneous Media*. Phys. Rev. Lett., vol. 110, page 238101, Jun 2013. (Cited on pages 67 and 68.)

[Codina *et al.* 2022] Joan Codina, Benoît Mahault, Hugues Chaté, Jure Dobnikar, Ignacio Pagonabarraga and Xia-qing Shi. *Small Obstacle in a Large Polar Flock*. Phys. Rev. Lett., vol. 128, page 218001, May 2022. (Cited on pages 66, 67, 78, 81, 87, 90 and 130.)

[Curatolo *et al.* 2020] AI Curatolo, N Zhou, Y Zhao, C Liu, A Daerr, J Tailleur and J Huang. *Cooperative pattern formation in multi-component bacterial systems through reciprocal motility regulation*. Nature Physics, vol. 16, no. 11, pages 1152–1157, 2020. (Cited on page 6.)

[Czirók *et al.* 1999] András Czirók, Albert-László Barabási and Tamás Vicsek. *Collective motion of self-propelled particles: Kinetic phase transition in one dimension*. Physical Review Letters, vol. 82, no. 1, page 209, 1999. (Cited on pages 22, 23, 24, 25, 32, 63 and 127.)

[Deseigne *et al.* 2010] Julien Deseigne, Olivier Dauchot and Hugues Chaté. *Collective motion of vibrated polar disks.* Physical Review Letters, vol. 105, no. 9, page 098001, 2010. (Cited on pages 6, 10 and 11.)

[Digregorio *et al.* 2018] Pasquale Digregorio, Demian Levis, Antonio Suma, Leticia F. Cugliandolo, Giuseppe Gonnella and Ignacio Pagonabarraga. *Full Phase Diagram of Active Brownian Disks: From Melting to Motility-Induced Phase Separation.* Phys. Rev. Lett., vol. 121, page 098003, Aug 2018. (Cited on page 96.)

[Digregorio *et al.* 2021] Pasquale Digregorio, Demian Levis, Leticia F. Cugliandolo, Giuseppe Gonnella and Ignacio Pagonabarraga. *Unified analysis of Topological Defects in 2D systems of Active and Passive disks*, 2021. (Cited on pages 126 and 132.)

[Digregorio *et al.* 2022] Pasquale Digregorio, Demian Levis, Leticia F. Cugliandolo, Giuseppe Gonnella and Ignacio Pagonabarraga. *Unified analysis of topological defects in 2D systems of active and passive disks.* Soft Matter, vol. 18, pages 566–591, 2022. (Cited on page 97.)

[Domb & Green 1972] C. Domb and M. S. Green, editors. 'rigorous results and theorems', by r.b. griffiths in phase transitions and critical phenomena, volume 1. Academic Press, London, 1972. (Cited on page 66.)

[Dossetti 2011] V Dossetti. *Cohesive motion in one-dimensional flocking.* Journal of Physics A: Mathematical and Theoretical, vol. 45, no. 3, page 035003, 2011. Publisher: IOP Publishing. (Cited on pages 25, 63 and 127.)

[Duan *et al.* 2021] Yu Duan, Benoît Mahault, Yu-qiang Ma, Xia-qing Shi and Hugues Chaté. *Breakdown of Ergodicity and Self-Averaging in Polar Flocks with Quenched Disorder.* Phys. Rev. Lett., vol. 126, page 178001, Apr 2021. (Cited on page 68.)

[Ebeling *et al.* 1999] Werner Ebeling, Frank Schweitzer and Benno Tilch. *Active Brownian particles with energy depots modeling animal mobility.* Biosystems, vol. 49, no. 1, pages 17–29, 1999. (Cited on page 4.)

[Ehrenfest 1933] P. Ehrenfest. *Phasenumwandlungen im ueblichen und erweiterten Sinn, classifiziert nach den entsprechenden Singularitaeten des ther-*

modynamischen Potentiales. Proc. Royal Acad. Amsterdam, vol. 36, 1933. (Cited on page 2.)

[Einstein 1905] A. Einstein. *Über die von der molekularkinetischen Theorie der Wärme geforderte Bewegung von in ruhenden Flüssigkeiten suspendierten Teilchen.* Annalen der Physik, vol. 322, no. 8, pages 549–560, 1905. (Cited on page 3.)

[Evans & Hanney 2005] M R Evans and T Hanney. *Nonequilibrium statistical mechanics of the zero-range process and related models.* Journal of Physics A: Mathematical and General, vol. 38, no. 19, pages R195–R240, apr 2005. (Cited on page 106.)

[Farrell *et al.* 2012] FDC Farrell, MC Marchetti, D Marenduzzo and J Tailleur. *Pattern formation in self-propelled particles with density-dependent motility.* Physical review letters, vol. 108, no. 24, page 248101, 2012. (Cited on page 49.)

[Fausti *et al.* 2021] G. Fausti, E. Tjhung, M. E. Cates and C. Nardini. *Capillary Interfacial Tension in Active Phase Separation.* Phys. Rev. Lett., vol. 127, page 068001, Aug 2021. (Cited on page 93.)

[Fausti 2021] Giordano Fausti. *Phase separation in active systems : non-equilibrium fingerprints.* Theses, Université Paris-Saclay, December 2021. (Cited on pages 96, 97, 98, 120 and 122.)

[Fily & Marchetti 2012] Yaouen Fily and M. Cristina Marchetti. *Athermal Phase Separation of Self-Propelled Particles with No Alignment.* Phys. Rev. Lett., vol. 108, page 235702, Jun 2012. (Cited on page 16.)

[Fodor *et al.* 2016] Étienne Fodor, Cesare Nardini, Michael E. Cates, Julien Tailleur, Paolo Visco and Frédéric van Wijland. *How Far from Equilibrium Is Active Matter?* Phys. Rev. Lett., vol. 117, page 038103, Jul 2016. (Cited on page 16.)

[Galajda *et al.* 2007] Peter Galajda, Juan Keymer, Paul Chaikin and Robert Austin. *A Wall of Funnels Concentrates Swimming Bacteria.* Journal of Bacteriology, vol. 189, no. 23, pages 8704–8707, 2007. (Cited on page 4.)

[Gautrais *et al.* 2012] Jacques Gautrais, Francesco Ginelli, Richard Fournier, Stéphane Blanco, Marc Soria, Hugues Chaté and Guy Theraulaz. *Deciphering interactions in moving animal groups.* Plos computational biology, vol. 8, no. 9, page e1002678, 2012. (Cited on page 6.)

[Geyer *et al.* 2019] Delphine Geyer, David Martin, Julien Tailleur and Denis Bartolo. *Freezing a flock: Motility-induced phase separation in polar active liquids.* Physical Review X, vol. 9, no. 3, page 031043, 2019. Publisher: APS. (Cited on page 6.)

[Giavazzi *et al.* 2017] Fabio Giavazzi, Matteo Paoluzzi, Marta Macchi, Dapeng Bi, Giorgio Scita, M. Lisa Manning, Roberto Cerbino and M. Cristina Marchetti. *Flocking Transition in Confluent Tissues*, 2017. (Cited on page 10.)

[Gillespie 1976] Daniel T. Gillespie. *A General Method for Numerically Simulating the Stochastic Time Evolution of Coupled Chemical Reactions.* Journal of Computational Physics, vol. 22, no. 4, pages 403–434, December 1976. (Cited on page 28.)

[Ginot *et al.* 2018] Felix Ginot, Alexandre Solon, Yariv Kafri, Christophe Ybert, Julien Tailleur and Cecile Cottin-Bizonne. *Sedimentation of self-propelled Janus colloids: polarization and pressure.* New Journal of Physics, vol. 20, no. 11, page 115001, 2018. (Cited on page 6.)

[Grégoire & Chaté 2004] Guillaume Grégoire and Hugues Chaté. *Onset of Collective and Cohesive Motion.* Phys. Rev. Lett., vol. 92, page 025702, Jan 2004. (Cited on page 12.)

[Gueron & Levin 1993] Shay Gueron and Simon Asher Levin. *Self-organization of front patterns in large wildebeest herds.* Journal of Theoretical Biology, vol. 165, no. 4, pages 541–552, December 1993. (Cited on page 10.)

[Hatwalne *et al.* 2004] Yashodhan Hatwalne, Sriram Ramaswamy, Madan Rao and R. Aditi Simha. *Rheology of Active-Particle Suspensions.* Phys. Rev. Lett., vol. 92, page 118101, Mar 2004. (Cited on page 9.)

[Hermann *et al.* 2019] Sophie Hermann, Daniel de las Heras and Matthias Schmidt. *Non-negative Interfacial Tension in Phase-Separated Active*

Brownian Particles. Phys. Rev. Lett., vol. 123, page 268002, Dec 2019. (Cited on page 93.)

[Hohenberg & Halperin 1977] P. C. Hohenberg and B. I. Halperin. *Theory of dynamic critical phenomena.* Rev. Mod. Phys., vol. 49, pages 435–479, Jul 1977. (Cited on page 9.)

[Howse *et al.* 2007] Jonathan R Howse, Richard AL Jones, Anthony J Ryan, Tim Gough, Reza Vafabakhsh and Ramin Golestanian. *Self-motile colloidal particles: from directed propulsion to random walk.* Physical review letters, vol. 99, no. 4, page 048102, 2007. (Cited on pages 5 and 6.)

[Illien *et al.* 2020] Pierre Illien, Charlotte de Blois, Yang Liu, Marjolein N. van der Linden and Olivier Dauchot. *Speed-dispersion-induced alignment: A one-dimensional model inspired by swimming droplets experiments.* Phys. Rev. E, vol. 101, page 040602, Apr 2020. (Cited on page 24.)

[Ising 1925] Ernst Ising. *Beitrag zur Theorie des Ferromagnetismus.* Zeitschrift fur Physik, vol. 31, no. 1, pages 253–258, February 1925. (Cited on page 22.)

[Karani *et al.* 2019] Hamid Karani, Gerardo E Pradillo and Petia M Vlahovska. *Tuning the random walk of active colloids: From individual run-and-tumble to dynamic clustering.* Physical review letters, vol. 123, no. 20, page 208002, 2019. Publisher: APS. (Cited on pages 5 and 6.)

[Kardar *et al.* 1986] Mehran Kardar, Giorgio Parisi and Yi-Cheng Zhang. *Dynamic Scaling of Growing Interfaces.* Phys. Rev. Lett., vol. 56, pages 889–892, Mar 1986. (Cited on page 4.)

[Kardar 2007] Mehran Kardar. Statistical physics of fields. Cambridge University Press, 2007. (Cited on page 66.)

[Kolmogorov 1936] A. Kolmogorov. *Zur Theorie der Markoffschen Ketten.* Mathematische Annalen, vol. 112, no. 1, pages 155–160, Dec 1936. (Cited on page 3.)

[Kourbane-Houssene *et al.* 2018] Mourtaza Kourbane-Houssene, Clément Erignoux, Thierry Bodineau and Julien Tailleur. *Exact hydrodynamic description of active lattice gases.* Physical review letters, vol. 120, no. 26, page 268003, 2018. (Cited on page 57.)

[Krapivsky *et al.* 1999] P. L. Krapivsky, J. F. F. Mendes and S. Redner. *Influence of island diffusion on submonolayer epitaxial growth.* Physical Review B, vol. 59, no. 24, pages 15950–15958, jun 1999. (Cited on page 111.)

[Krapivsky *et al.* 2010] Pavel L. Krapivsky, Sidney Redner and Eli Ben-Naim. A kinetic view of statistical physics. Cambridge University Press, 2010. (Cited on pages 82, 98, 104, 106, 122 and 142.)

[Kruse *et al.* 2004] Karsten Kruse, Jean-François Joanny, Frank Jülicher, Jacques Prost and Ken Sekimoto. *Asters, vortices, and rotating spirals in active gels of polar filaments.* Physical review letters, vol. 92, no. 7, page 078101, 2004. (Cited on page 49.)

[Kubo 1966] R. Kubo. *The fluctuation-dissipation theorem.* Reports on Progress in Physics, vol. 29, no. 1, pages 255–284, January 1966. (Cited on page 3.)

[Kumar *et al.* 2014] Nitin Kumar, Harsh Soni, Sriram Ramaswamy and AK Sood. *Flocking at a distance in active granular matter.* Nature communications, vol. 5, no. 1, pages 1–9, 2014. Publisher: Nature Publishing Group. (Cited on page 6.)

[Laighléis *et al.* 2018] E Ó Laighléis, Martin R Evans and Richard A Blythe. *Minimal stochastic field equations for one-dimensional flocking.* Physical Review E, vol. 98, no. 6, page 062127, 2018. Publisher: APS. (Cited on pages 23, 25, 63 and 127.)

[Landau & Lifshitz 1980] L. D. Landau and E. M. Lifshitz. Statistical Physics Part I. Elsevier, Amsterdam, 3rd édition, 1980. bibtex: landa;b;sp80. (Cited on page 22.)

[Liu *et al.* 2011] Chenli Liu, Xiongfei Fu, Lizhong Liu, Xiaojing Ren, Carlos KL Chau, Sihong Li, Lu Xiang, Hualing Zeng, Guanhua Chen, Lei-Han Tang*et al.* *Sequential establishment of stripe patterns in an expanding cell population.* Science, vol. 334, no. 6053, pages 238–241, 2011. (Cited on page 18.)

[Liu *et al.* 2019] Guannan Liu, Adam Patch, Fatmagül Bahar, David Yllanes, Roy D Welch, M Cristina Marchetti, Shashi Thutupalli and Joshua W

Shaevitz. *Self-Driven Phase Transitions Drive Myxococcus xanthus Fruiting Body Formation.* Physical review letters, vol. 122, no. 24, page 248102, 2019. Publisher: APS. (Cited on pages 5, 6 and 18.)

[Liu *et al.* 2021] Zeng Tao Liu, Yan Shi, Yongfeng Zhao, Hugues Chaté, Xia-qing Shi and Tian Hui Zhang. *Activity waves and freestanding vortices in populations of subcritical Quincke rollers.* Proceedings of the National Academy of Sciences, vol. 118, no. 40, page e2104724118, 2021. Publisher: National Acad Sciences. (Cited on pages 5 and 6.)

[López *et al.* 2015] Héctor Matías López, Jérémie Gachelin, Carine Douarche, Harold Auradou and Eric Clément. *Turning bacteria suspensions into superfluids.* Physical review letters, vol. 115, no. 2, page 028301, 2015. (Cited on page 6.)

[Mahault *et al.* 2019] Benoît Mahault, Francesco Ginelli and Hugues Chaté. *Quantitative Assessment of the Toner and Tu Theory of Polar Flocks.* Phys. Rev. Lett., vol. 123, page 218001, Nov 2019. (Cited on page 12.)

[Martin *et al.* 2021a] David Martin, Hugues Chaté, Cesare Nardini, Alexandre Solon, Julien Tailleur and Frédéric Van Wijland. *Fluctuation-Induced Phase Separation in Metric and Topological Models of Collective Motion.* Phys. Rev. Lett., vol. 126, page 148001, Apr 2021. (Cited on pages 13 and 15.)

[Martin *et al.* 2021b] David Martin, Jérémy O'Byrne, Michael E. Cates, Étienne Fodor, Cesare Nardini, Julien Tailleur and Frédéric van Wijland. *Statistical mechanics of active Ornstein-Uhlenbeck particles.* Phys. Rev. E, vol. 103, page 032607, Mar 2021. (Cited on pages 16 and 17.)

[Maxwell 1860] J.C. Maxwell. *On the Motions and Collisions of Perfectly Elastic Spheres.* Philosophical Magazine, 1860. (Cited on page 2.)

[Mermin & Wagner 1966] N. David Mermin and Ho Wagner. *Absence of ferromagnetism or antiferromagnetism in one-or two-dimensional isotropic Heisenberg models.* Physical Review Letters, vol. 17, no. 22, page 1133, 1966. (Cited on pages 4 and 66.)

[Morin *et al.* 2016] Alexandre Morin, Nicolas Desreumaux, Jean-Baptiste Caussin and Denis Bartolo. *Distortion and destruction of colloidal flocks in disordered environments.* Nature Physics, vol. 13, no. 1, pages 63–67, oct 2016. (Cited on pages 67 and 68.)

[Nardini *et al.* 2017] Cesare Nardini, Étienne Fodor, Elsen Tjhung, Frédéric van Wijland, Julien Tailleur and Michael E. Cates. *Entropy Production in Field Theories without Time-Reversal Symmetry: Quantifying the Non-Equilibrium Character of Active Matter.* Phys. Rev. X, vol. 7, page 021007, Apr 2017. (Cited on page 94.)

[O'Byrne *et al.* 2022] Jérémy O'Byrne, Alexandre Solon, Julien Tailleur and Yongfeng Zhao. *An Introduction to Motility-Induced Phase Separation*, 2022. (Cited on page 93.)

[O'Loan & Evans 1999] O. J. O'Loan and M. R. Evans. *Alternating steady state in one-dimensional flocking.* Journal of Physics A: Mathematical and General, vol. 32, no. 8, page L99, 1999. (Cited on pages 22, 23, 24, 25, 32, 38, 59, 63, 64 and 127.)

[Omar *et al.* 2020] Ahmad K. Omar, Zhen-Gang Wang and John F. Brady. *Microscopic origins of the swim pressure and the anomalous surface tension of active matter.* Phys. Rev. E, vol. 101, page 012604, Jan 2020. (Cited on page 93.)

[Parisi 2023] G. Parisi. In a Flight of Starlings: The Wonders of Complex Systems. Penguin Publishing Group, 2023. (Cited on page 6.)

[Patch *et al.* 2018] Adam Patch, Daniel M. Sussman, David Yllanes and M. Cristina Marchetti. *Curvature-dependent tension and tangential flows at the interface of motility-induced phases.* Soft Matter, vol. 14, pages 7435–7445, 2018. (Cited on pages 20, 93 and 131.)

[Peierls 1991] Rudolf Peierls. More surprises in theoretical physics. Princeton University Press, 1991. (Cited on page 66.)

[Poel *et al.* 2022] Winnie Poel, Bryan C Daniels, Matthew MG Sosna, Colin R Twomey, Simon P Leblanc, Iain D Couzin and Pawel Romanczuk. *Subcritical escape waves in schooling fish.* Science Advances, vol. 8, no. 25, page eabm6385, 2022. Publisher: American Association for the Advancement of Science. (Cited on page 6.)

[Rajesh & Majumdar 2001] R. Rajesh and Satya N. Majumdar. *Exact phase diagram of a model with aggregation and chipping.* Phys. Rev. E, vol. 63, page 036114, Feb 2001. (Cited on pages 100, 101 and 122.)

[Rajesh *et al.* 2002] R. Rajesh, Dibyendu Das, Bulbul Chakraborty and Mustansir Barma. *Aggregate formation in a system of coagulating and fragmenting particles with mass-dependent diffusion rates.* Phys. Rev. E, vol. 66, page 056104, Nov 2002. (Cited on pages 102, 113, 122 and 143.)

[Raymond & Evans 2006] JR Raymond and MR Evans. *Flocking regimes in a simple lattice model.* Physical Review E, vol. 73, no. 3, page 036112, 2006. Publisher: APS. (Cited on pages 24, 32, 38, 57, 63 and 64.)

[Redner *et al.* 2013] Gabriel S. Redner, Michael F. Hagan and Aparna Baskaran. *Structure and Dynamics of a Phase-Separating Active Colloidal Fluid.* Phys. Rev. Lett., vol. 110, page 055701, Jan 2013. (Cited on pages 16 and 17.)

[Rørth 2009] Pernille Rørth. *Collective Cell Migration.* Annual Review of Cell and Developmental Biology, vol. 25, no. 1, pages 407–429, 2009. PMID: 19575657. (Cited on page 10.)

[Sakaguchi & Ishibashi 2019] Hidetsugu Sakaguchi and Kazuya Ishibashi. *Flip motion of solitary wave in an Ising-type Vicsek model.* Physical Review E, vol. 100, no. 5, page 052113, 2019. Publisher: APS. (Cited on pages 25, 63, 67, 68 and 127.)

[Schaller *et al.* 2011] Volker Schaller, Christoph A Weber, Benjamin Hammerich, Erwin Frey and Andreas R Bausch. *Frozen steady states in active systems.* Proceedings of the National Academy of Sciences, vol. 108, no. 48, pages 19183–19188, 2011. (Cited on page 6.)

[Schimansky-Geier *et al.* 1995] Lutz Schimansky-Geier, Michaela Mieth, Helge Rosé and Horst Malchow. *Structure formation by active Brownian particles.* Physics Letters A, vol. 207, no. 3, pages 140–146, 1995. (Cited on page 4.)

[Schnitzer 1993] Mark J. Schnitzer. *Theory of continuum random walks and application to chemotaxis*. Phys. Rev. E, vol. 48, pages 2553–2568, Oct 1993. (Cited on page 4.)

[Shaw 1978] Evelyn Shaw. *Schooling Fishes*. American Scientist, vol. 66, no. 2, pages 166–175, March 1978. (Cited on page 10.)

[Shi *et al.* 2020] Xia-qing Shi, Giordano Fausti, Hugues Chaté, Cesare Nardini and Alexandre Solon. *Self-Organized Critical Coexistence Phase in Repulsive Active Particles*. Phys. Rev. Lett., vol. 125, page 168001, Oct 2020. (Cited on pages 20, 96, 97, 98, 111, 120, 121 and 122.)

[Siggia 1979] Eric D. Siggia. *Late stages of spinodal decomposition in binary mixtures*. Phys. Rev. A, vol. 20, pages 595–605, Aug 1979. (Cited on page 111.)

[Smoluchowski 1917] M. V. Smoluchowski. *Mathematical Theory of the Kinetics of the Coagulation of Colloidal Solutions*. Zeitschrift für Physikalische Chemie, Jan 1917. (Cited on pages 115 and 118.)

[Sokolov & Aranson 2012] Andrey Sokolov and Igor S Aranson. *Physical properties of collective motion in suspensions of bacteria*. Physical review letters, vol. 109, no. 24, page 248109, 2012. Publisher: APS. (Cited on page 6.)

[Solon & Tailleur 2013] AP Solon and Julien Tailleur. *Revisiting the flocking transition using active spins*. Physical review letters, vol. 111, no. 7, page 078101, 2013. (Cited on pages 14, 22, 23, 24, 25, 26, 30, 31, 32, 33, 43, 63 and 70.)

[Solon & Tailleur 2015] Alexandre P Solon and Julien Tailleur. *Flocking with discrete symmetry: The two-dimensional active Ising model*. Physical Review E, vol. 92, no. 4, page 042119, 2015. Publisher: APS. (Cited on pages 14, 25, 27, 30, 32, 36, 38, 70, 71 and 82.)

[Solon *et al.* 2015a] A. P. Solon, M. E. Cates and J. Tailleur. *Active brownian particles and run-and-tumble particles: A comparative study*. The European Physical Journal Special Topics, vol. 224, no. 7, pages 1231–1262, jul 2015. (Cited on pages 16 and 17.)

[Solon *et al.* 2015b] Alexandre P Solon, Jean-Baptiste Caussin, Denis Bartolo, Hugues Chaté and Julien Tailleur. *Pattern formation in flocking models: A* *hydrodynamic description.* Physical Review E, vol. 92, no. 6, page 062111, 2015. (Cited on pages 15, 42 and 83.)

[Solon *et al.* 2015c] Alexandre P. Solon, Hugues Chaté and Julien Tailleur. *From Phase to Microphase Separation in Flocking Models: The Essential Role of Nonequilibrium Fluctuations.* Phys. Rev. Lett., vol. 114, page 068101, Feb 2015. (Cited on pages 13 and 15.)

[Solon *et al.* 2015d] Alexandre P Solon, Hugues Chaté and Julien Tailleur. *From Phase to Microphase Separation in Flocking Models: The Essential Role of Nonequilibrium Fluctuations.* Physical review letters, vol. 114, no. 6, page 068101, 2015. (Cited on page 32.)

[Solon *et al.* 2015e] Alexandre P. Solon, Joakim Stenhammar, Raphael Wittkowski, Mehran Kardar, Yariv Kafri, Michael E. Cates and Julien Tailleur. *Pressure and Phase Equilibria in Interacting Active Brownian Spheres.* Phys. Rev. Lett., vol. 114, page 198301, May 2015. (Cited on page 16.)

[Solon *et al.* 2018a] Alexandre P Solon, Joakim Stenhammar, Michael E Cates, Yariv Kafri and Julien Tailleur. *Generalized thermodynamics of motility-induced phase separation: phase equilibria, Laplace pressure, and change of ensembles.* New Journal of Physics, vol. 20, no. 7, page 075001, jul 2018. (Cited on pages 20, 92, 93 and 131.)

[Solon *et al.* 2018b] Alexandre P. Solon, Joakim Stenhammar, Michael E. Cates, Yariv Kafri and Julien Tailleur. *Generalized thermodynamics of phase equilibria in scalar active matter.* Phys. Rev. E, vol. 97, page 020602, Feb 2018. (Cited on pages 18 and 19.)

[Solon *et al.* 2022] Alexandre Solon, Hugues Chaté, John Toner and Julien Tailleur. *Susceptibility of polar flocks to spatial anisotropy.* Physical Review Letters, vol. 128, no. 20, page 208004, 2022. (Cited on pages 68, 89 and 125.)

[Soni *et al.* 2020] Harsh Soni, Nitin Kumar, Jyothishraj Nambisan, Rahul Kumar Gupta, AK Sood and Sriram Ramaswamy. *Phases and excitations of active rod–bead mixtures: simulations and experiments.* Soft Matter, vol. 16, no. 31, pages 7210–7221, 2020. Publisher: Royal Society of Chemistry. (Cited on page 6.)

[Stenhammar *et al.* 2013] Joakim Stenhammar, Adriano Tiribocchi, Rosalind J. Allen, Davide Marenduzzo and Michael E. Cates. *Continuum Theory of Phase Separation Kinetics for Active Brownian Particles*. Physical Review Letters, vol. 111, no. 14, oct 2013. (Cited on page 16.)

[Stenhammar *et al.* 2014] Joakim Stenhammar, Davide Marenduzzo, Rosalind J. Allen and Michael E. Cates. *Phase behaviour of active Brownian particles: the role of dimensionality*. Soft Matter, vol. 10, pages 1489–1499, 2014. (Cited on pages 95 and 96.)

[Stenhammar 2021] Joakim Stenhammar. *An Introduction to Motility-Induced Phase Separation*, 2021. (Cited on page 18.)

[Sumino *et al.* 2012] Yutaka Sumino, Ken H. Nagai, Yuji Shitaka, Dan Tanaka, Kenichi Yoshikawa, Hugues Chaté and Kazuhiro Oiwa. *Large-scale vortex lattice emerging from collectively moving microtubules*. Nature, vol. 483, no. 7390, pages 448–452, 2012. (Cited on pages 5 and 6.)

[Tailleur & Cates 2008] J. Tailleur and M. E. Cates. *Statistical Mechanics of Interacting Run-and-Tumble Bacteria*. Phys. Rev. Lett., vol. 100, page 218103, May 2008. (Cited on pages 4 and 16.)

[Takatori & Brady 2015] S. C. Takatori and J. F. Brady. *Towards a thermodynamics of active matter*. Phys. Rev. E, vol. 91, page 032117, Mar 2015. (Cited on page 16.)

[Thompson *et al.* 2010] Alasdair G Thompson, Julien Tailleur, Michael E Cates and Richard A Blythe. *Zero-range processes with saturated condensation: the steady state and dynamics*. Journal of Statistical Mechanics: Theory and Experiment, vol. 2010, no. 02, page P02013, 2010. (Cited on page 56.)

[Thompson *et al.* 2011] A G Thompson, J Tailleur, M E Cates and R A Blythe. *Lattice models of nonequilibrium bacterial dynamics*. Journal of Statistical Mechanics: Theory and Experiment, vol. 2011, no. 02, page P02029, feb 2011. (Cited on page 16.)

[Tjhung *et al.* 2018] Elsen Tjhung, Cesare Nardini and Michael E. Cates. *Cluster Phases and Bubbly Phase Separation in Active Fluids: Reversal of the Ostwald Process*. Phys. Rev. X, vol. 8, page 031080, Sep 2018. (Cited on pages 20, 93, 94, 95, 97, 98, 120, 121 and 122.)

[Toner & Tu 1995] John Toner and Yuhai Tu. *Long-range order in a two-dimensional dynamical XY model: how birds fly together*. Physical Review Letters, vol. 75, no. 23, page 4326, 1995. (Cited on pages 4, 9, 12 and 66.)

[Toner & Tu 1998] John Toner and Yuhai Tu. *Flocks, herds, and schools: A quantitative theory of flocking*. Phys. Rev. E, vol. 58, pages 4828–4858, Oct 1998. (Cited on page 12.)

[Toner *et al.* 2005] John Toner, Yuhai Tu and Sriram Ramaswamy. *Hydrodynamics and phases of flocks*. Annals of Physics, vol. 318, no. 1, pages 170–244, 2005. (Cited on page 12.)

[Toner *et al.* 2018] John Toner, Nicholas Guttenberg and Yuhai Tu. *Swarming in the Dirt: Ordered Flocks with Quenched Disorder*. Physical Review Letters, vol. 121, no. 24, dec 2018. (Cited on page 68.)

[Toner 2012a] John Toner. *Birth, Death, and Flight: A Theory of Malthusian Flocks*. Phys. Rev. Lett., vol. 108, page 088102, Feb 2012. (Cited on page 66.)

[Toner 2012b] John Toner. *Reanalysis of the hydrodynamic theory of fluid, polar-ordered flocks*. Physical Review E, vol. 86, no. 3, page 031918, 2012. (Cited on page 12.)

[Tsebers 1980] A. O. Tsebers. *Internal rotation in the hydrodynamics of weakly conducting dielectric suspensions*. Fluid Dynamics, vol. 15, no. 2, pages 245–251, Mar 1980. (Cited on page 6.)

[Tu *et al.* 1998] Yuhai Tu, John Toner and Markus Ulm. *Sound Waves and the Absence of Galilean Invariance in Flocks*. Physical Review Letters, vol. 80, no. 21, pages 4819–4822, may 1998. (Cited on page 12.)

[van der Linden *et al.* 2019] Marjolein N. van der Linden, Lachlan C. Alexander, Dirk G. A. L. Aarts and Olivier Dauchot. *Interrupted Motility Induced Phase Separation in Aligning Active Colloids*. Phys. Rev. Lett., vol. 123, page 098001, Aug 2019. (Cited on pages 17 and 18.)

[Van Kampen 1992] Nicolaas Godfried Van Kampen. Stochastic processes in physics and chemistry, volume 1. Elsevier, 1992. (Cited on page 52.)

[Ventejou *et al.* 2021] Bruno Ventejou, Hugues Chaté, Raul Montagne and Xiaqing Shi. *Susceptibility of Orientationally Ordered Active Matter to Chirality Disorder*. Phys. Rev. Lett., vol. 127, page 238001, Nov 2021. (Cited on pages 67, 68 and 130.)

[Vicsek *et al.* 1995] Tamás Vicsek, András Czirók, Eshel Ben-Jacob, Inon Cohen and Ofer Shochet. *Novel type of phase transition in a system of self-driven particles*. Physical review letters, vol. 75, no. 6, page 1226, 1995. (Cited on pages 4, 11 and 66.)

[Weihs 1973] D. Weihs. *Hydromechanics of Fish Schooling*. nat, vol. 241, no. 5387, pages 290–291, 1973. (Cited on page 10.)

[Wensink *et al.* 2012] Henricus H Wensink, Jörn Dunkel, Sebastian Heidenreich, Knut Drescher, Raymond E Goldstein, Hartmut Löwen and Julia M Yeomans. *Meso-scale turbulence in living fluids*. Proceedings of the National Academy of Sciences, vol. 109, no. 36, pages 14308–14313, 2012. (Cited on page 6.)

[Wysocki *et al.* 2014] Adam Wysocki, Roland G. Winkler and Gerhard Gompper. *Cooperative motion of active Brownian spheres in three-dimensional dense suspensions*. EPL (Europhysics Letters), vol. 105, no. 4, page 48004, feb 2014. (Cited on page 16.)

[Yates *et al.* 2009] Christian A. Yates, Radek Erban, Carlos Escudero, Iain D. Couzin, Jerome Buhl, Ioannis G. Kevrekidis, Philip K. Maini and David J. T. Sumpter. *Inherent noise can facilitate coherence in collective swarm motion*. Proceedings of the National Academy of Sciences, vol. 106, no. 14, pages 5464–5469, 2009. (Cited on page 24.)

[Zakine & Vanden-Eijnden 2022] Ruben Zakine and Eric Vanden-Eijnden. *Minimum Action Method for Nonequilibrium Phase Transitions*, 2022. (Cited on pages 126 and 133.)

[Zhang *et al.* 2017] Jie Zhang, Bartosz A Grzybowski and Steve Granick. *Janus particle synthesis, assembly, and application*. Langmuir, vol. 33, no. 28, pages 6964–6977, 2017. Publisher: ACS Publications. (Cited on page 6.)

[Zhang *et al.* 2020] Bo Zhang, Andrey Sokolov and Alexey Snezhko. *Reconfigurable emergent patterns in active chiral fluids*. Nature Communications, vol. 11, page 4401, 09 2020. (Cited on pages 10 and 11.)

Propriétés exotiques des phases ordonnées en matière active

Résumé :

La matière active englobe tous les systèmes dont les composants dissipent de l'énergie afin d'exercer des forces sur leur environnement. Les systèmes actifs peuvent être trouvés à toutes les échelles, des moteurs moléculaires aux groupes d'animaux, en passant par les colonies de bactéries. Étant intrinsèquement hors d'équilibre, ces systèmes présentent de manière générique des comportements collectifs sans contrepartie à l'équilibre.

Nous nous concentrons sur deux comportements collectifs paradigmatiques en matière active : le *flocking*, dans lequel des particules auto-propulsées et soumisent à des interactions d'alignement s'organisent à grande échelle pour se déplacer collectivement, et la séparation de phase induite par la motilité, dans laquelle des particules auto-propulsées et soumises à des forces répulsives forment un agrégat. Ces comportements collectifs présentent des propriétés exotiques que nous étudions dans cette thèse.

Nous étudions d'abord le modèle d'Ising actif, un modèle de flocking avec une symétrie discrète. En une dimension, le mouvement collectif se traduit par la présence d'un agrégat de particules qui subit des retournements stochastiques de sa direction. Nous caractérisons en détail la forme de ces agrégats et la statistique de leurs retournements. Le scénario général est celui d'une séparation de phase liquide-gaz. À basse température, nous observons l'existence d'une nouvelle phase peuplée d'objets statiques que nous appelons "asters", qui apparaissent uniquement en raison de l'interaction entre l'auto-propulsion et l'alignement. Nous obtenons une solution exacte pour caractériser leur dynamique à température nulle et calculons leur forme à l'aide d'une description de champ moyen.

En plus grandes dimensions, nous étudions les états ordonnés du modèle d'Ising actif. Jusqu'à présent, de tels états étaient considérés comme stables, mais nous montrons qu'ils sont en réalité métastables dû à la nucléation spontanée de gouttelettes se propageant dans le sens contraire à l'ordre établi. En utilisant à la fois des simulations microscopiques et une théorie continue, nous montrons que des gouttelettes suffisamment grandes peuvent grossir et détruire l'ordre existant. En considérant la même théorie continue en $2d$ mais avec un paramètre d'ordre vectoriel, nous montrons numériquement que l'advection verticale entrave la propagation des gouttelettes, pour les paramètres testés.

Dans la séparation de phase induite par la motilité, le couplage entre le mouvement persistant des particules actives et leurs interactions répulsives conduit à la formation d'un agrégat dense entouré d'un gaz dilué. Parce que la pression de Laplace est négative, des bulles de gaz se forment et se développent dans cet agrégat, de sorte que le cadre général est celui d'une séparation de phase à bulles. Nous présentons des modèles minimaux pour rendre compte de la dynamique de ces bulles. Ils reproduisent les distributions sans échelles des tailles de bulles et les effets de taille finie observés dans les modèles microscopiques. Nous concluons en fournissant des preuves numériques que la nucléation des bulles est non-locale.

Exotic properties of ordered phases in active matter

Abstract:

Active matter encompasses all systems whose components dissipate energy in order to exert forces on their environment. Example of active matter systems can be found at all scales, from molecular motors to bacterial swarms and animal groups. Being intrinsically out of equilibrium, these systems generically display collective behaviours with no equilibrium counterpart.

We focus on two paradigmatic collective behaviours in active matter: flocking, the ability of collections of aligning self-propelled particles to move collectively on large scales, and the motility-induced phase separation, in which repulsive self-propelled particles aggregate in the absence of attractive forces. These collective behaviours display exotic properties that we study in this thesis.

We first study the active Ising model, a flocking model with discrete symmetry. In one space dimension, collective motion takes the specific form of an ordered aggregate of particles undergoing stochastic reversals. We characterize in details the shape of these aggregates and the statistics of their reversals. The scenario is that of a liquid-gas phase separation which is prevented to relax to the phase-separated profile due to reversals. At low temperature, we report a new phase populated by static objects that we term "asters" which appear solely due to the interplay of self-propulsion and alignment. We provide an exact solution of their dynamics at zero temperature and compute their shape using a mean-field description.

In higher spatial dimensions, we investigate the ordered states of the active Ising model. So far, such states were believed to be stable but we show that they are actually metastable to the spontaneous nucleation of counter-propagating droplets. Using both particle-level simulations and a continuum theory, we show that large enough droplets can grow and destroy the existing order. Considering the same continuum theory in $2d$, albeit with a vectorial order parameter, we numerically show that any amount of vertical advection hinders the propagation of droplets, at least for the parameter values that we tested.

In the motility-induced phase separation, the coupling between persistent motion of active particles and pair-wise repulsive interactions leads to the formation of a dense cluster surrounded by a remaining dilute gas. In addition, because the Laplace pressure is negative, gas bubbles nucleate and grow in this dense aggregate, so that the global picture is that of a bubbly phase separation. We present minimal models to account for the dynamics of bubbles. They reproduce the scale-free bubble size distributions and the finite-size scalings observed in microscopic models. We conclude by providing numerical evidences that bubble nucleation is non-local.